

Sheffield Hallam University

Factors affecting the constitution and stability of iron-base austenitic alloys.

CAWLEY, Jess.

Available from the Sheffield Hallam University Research Archive (SHURA) at:

<http://shura.shu.ac.uk/19434/>

A Sheffield Hallam University thesis

This thesis is protected by copyright which belongs to the author.

The content must not be changed in any way or sold commercially in any format or medium without the formal permission of the author.

When referring to this work, full bibliographic details including the author, title, awarding institution and date of the thesis must be given.

Please visit <http://shura.shu.ac.uk/19434/> and <http://shura.shu.ac.uk/information.html> for further details about copyright and re-use permissions.

BAR CODE

791 393 1019.

ProQuest Number: 10694315

All rights reserved

INFORMATION TO ALL USERS

The quality of this reproduction is dependent upon the quality of the copy submitted.

In the unlikely event that the author did not send a complete manuscript and there are missing pages, these will be noted. Also, if material had to be removed, a note will indicate the deletion.



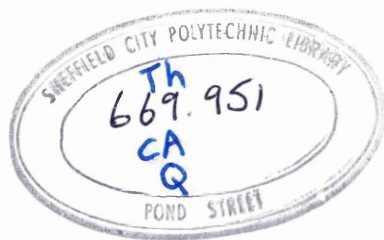
ProQuest 10694315

Published by ProQuest LLC (2017). Copyright of the Dissertation is held by the Author.

All rights reserved.

This work is protected against unauthorized copying under Title 17, United States Code
Microform Edition © ProQuest LLC.

ProQuest LLC.
789 East Eisenhower Parkway
P.O. Box 1346
Ann Arbor, MI 48106 – 1346



791393101

FACTORS AFFECTING THE CONSTITUTION AND
STABILITY OF IRON-BASE AUSTENITIC ALLOYS

Jess Cawley B.Sc.

This Thesis is submitted in partial fulfilment
of the requirements for the Degree of PhD of
the Council for National Academic Awards.

The collaborating establishment was:-

United Kingdom Atomic Energy Authority
Atomic Energy Research Establishment
Harwell, Oxon, OX11 0RA

December 1982

Department of Metallurgy
Sheffield City Polytechnic
Pond Street
Sheffield S1 1WB

FACTORS AFFECTING THE CONSTITUTION AND
STABILITY OF IRON-BASE AUSTENITIC ALLOYS

Jess Cawley B.Sc.

This thesis is based upon an investigation carried out mainly at Sheffield City Polytechnic, but also in part at the United Kingdom Atomic Energy Research Establishment, Harwell, during the period October 1978 to September 1981, under the supervision of Dr. F.B. Pickering of Sheffield City Polytechnic and Dr. D.R. Harries of U.K.A.E.R.E. (Harwell).

The thesis is submitted to the Council for National Academic Awards in partial requirement for the degree of Doctor of Philosophy, in December 1982. The Collaborating establishment in the work reported was the United Kingdom Atomic Energy Research Establishment, Harwell.

The candidate has not, during the period of registration for the CNAA degree of PhD, been a registered candidate for any other CNAA award or for any University degree.

The results presented in the thesis are, to the best of my knowledge, original except where reference and acknowledgement has been made to other authors. No part of this thesis has been submitted for a degree at any other University or College.

The following Conferences were attended during the work:-

- (1) Symposium "Design as related to the Properties of Materials" organised by the Sheffield Metallurgical and Engineering Association and the University of Sheffield, March 1979.
- (2) "Quantitative Microanalysis with high Spatial Resolution". UMIST Manchester, 25-27 March 1981, organised by the Metals Society/Royal Microscopical Society.
- (3) "Mechanical behaviour and Nuclear Application of Stainless Steels at Elevated Temperatures", 20-22 May 1981, Varese, Italy, organised by CEC-JRC Ispra Establishment and the Metals Society.
- (4) "Radiation Damage" Harwell February 18th 1982.

In addition the following courses were also attended:-

- (i) "Numerical Methods and Programming" Part of Module 1 of MSc in Metallurgical Process Management, October 1978-February 1979, Sheffield City Polytechnic.
- (ii) "High Strength Steels". Advanced Topic in Module 3 of the MSc in Metallurgical Process Management, May-June 1979, Sheffield City Polytechnic.

cont.

- (iii) "Multicomponent diffusion and gas/solid reaction"
Short Course run by the Department of Metallurgy,
Sheffield City Polytechnic, December 1978.

- (iv) "Heat Treatment and Transformations" Advanced Topic
in Module 3 of the MSc in Metallurgical Process
Management, Feb-June 1981, Sheffield City Polytechnic.

J. Cawley

December 1982

FACTORS AFFECTING THE CONSTITUTION AND
STABILITY OF IRON-BASE AUSTENITIC ALLOYS

Jess Cawley B.Sc.

ABSTRACT

A study of the constitution of Fe-Cr-Ni based alloys has been carried out. The isothermal sections of the ternary Fe-Cr-Ni system have been determined for temperatures between 1150°C and 650°C by analysing the composition of the individual phases by a micro-probe technique. The transformation of the delta ferrite, during the isothermal heat treatments, to either austenite or (austenite + sigma phase) has been investigated. In the sigma phase regions the delta ferrite transforms first to sigma phase which forms an envelope around the remaining delta ferrite which then transforms to a cellular structure of austenite + sigma phase.

The effect of fourth element additions namely:- (Mn,Cu,C,N, Si,Mo,Nb and Ti) which are known austenite or delta ferrite/sigma phase formers have been investigated. The constitutional effects of the fourth element additions have been quantified by the determination of nickel and chromium equivalents by a method which compares directly the effect of the fourth element additions against that of the nickel and chromium of the base alloy system.

The partitioning of selected alloying additions between the phases present has been investigated in an attempt to explain the microstructural effects of the alloy additions. The results suggest that the amount of partitioning is dependent upon the amount of alloy addition and is somewhat less than would be expected.

The concept of electron vacancy numbers has been used to predict the stability of the austenite phase and whether a particular composition is prone to sigma formation.

The effects of alloying additions on the void swelling characteristics of selected alloys has been studied using both the High Voltage Electron Microscope and Variable Energy Cyclotron with 46MeVNi⁶⁺ ions.

It has been shown that whilst most elements depress void swelling, manganese significantly increases void swelling at moderate levels of addition.

ACKNOWLEDGEMENTS

I would like to express my gratitude to those who have assisted me with my post graduate research, culminating in this thesis.

Firstly I wish to thank my internal supervisor Dr. F.B. Pickering, who's constant help and encouragement has been of inestimable value. My thanks are also due to Dr. D. R. Harries and Dr. T.M. Williams of the U.K.A.E.A. as Industrial supervisors.

I would generally like to thank the technical staff and research group at Sheffield City Polytechnic particularly Mr. G. Gregory who offered generous assistance.

I would specially like to thank my wife Linda who patiently typed and corrected the script and put up with a most unreasonable researcher many times. My thanks also go to Mr. B. Munks for the preparation of the graphs and diagrams.

Lastly I would like to thank the U.K.A.E.A. for provision of the award that made this thesis possible.

CONTENTSPage

1	<u>Introduction</u>	1
2	<u>Literature Review</u>	2
2.1.1.	The Iron-Chromium-Nickel System	2
2.1.2	Experimental Techniques for Equilibrium Diagram Determination	6
2.1.3	Effect of Alloying Elements	9
2.1.4	Prediction of Constitution	12
2.1.5	Prediction of Sigma Phase Formation by Electron Vacancy Number Calculations	14
2.1.5.1	Electron Vacancy Theory	15
2.1.5.2	Electron Vacancy Theory Applied to Alloys	16
2.1.5.3	Application to Commercial Alloys	17
2.1.5.4	Practical Electron Vacancy Calculations	18
2.1.6	Transformations in Stainless Steels	19
2.1.6.1	Transformations Occurring in Duplex Alloys	20
2.1.6.2	Carbides	22
2.1.6.3	Intermetallic Phases	23
2.1.6.4	Coherent Intermetallic Phases	25
2.1.7	The Effect of Irradiation on the Constitution	25
2.1.8.1	Void Swelling	27
2.1.8.2	Void Formation	29
2.1.8.3	Simulation Techniques of Neutron Irradiation	30
2.1.8.4	The Effect of Constitution and Microstructures on Void Swelling	33
2.1.8.5	Effect of Minor Elements	36
3	<u>Experimental Methods</u>	39
3.1.	The Experimental Alloys	39
3.2.	Manufacture of the Base Experimental Alloys	39
3.3.	Manufacture of Quaternary Alloys	40
3.4.	Heattreatment	41
3.5.	Metallography	41
3.6.	Quantitative Analysis of the Constitution	43
3.7.	Magnetic Measurements	45
3.8.	Kinetics and Phase Transformations	45
3.9.	Transmission Electron Microscopy	46
3.10	Quantitative Microanalysis	47
3.11	Simulation of Neutron Irradiation using a High Voltage Electron Microscope (H.V.E.M.)	53
3.12	Simulation of Neutron Irradiation using a Variable Energy Cyclotron (V.E.C)	57
4	<u>Results</u>	60
4.1.1.	Metallography of the Fe-Cr-Ni Experimental Alloys	60
4.1.2.	Microprobe Analysis	62
4.1.3.	The Isothermal Sections of the Ternary Constitutional Diagrams	64
4.2.	Transformation in Fe-Cr-Ni Stainless Steels	66
4.2.1.	Introduction	66
4.2.2.	Transformations in Alloy 3A(18Cr-2Ni)	66
4.2.3.	Transformations in Alloy 1A(30Cr-13Ni)	67

contents cont.	<u>Page</u>
4.2.4. Quantitative Metallography and Microanalysis	69
4.3. Effects of Fourth Element Additions on the Constitution of the Fe-Cr-Ni Alloys	69
4.3.1. Quantitative Metallography and Structural Changes	70
4.3.1.1. Additions of Austenite Forming Elements (Mn,Cu, C and N ₂)	70
4.3.1.2. Addition of Ferrite Forming Elements (Si,Mo,Nb and Ti)	71
4.3.2. Nickel and Chromium Equivalents	73
4.3.2.1. Nickel and Chromium Effects on the Constitution	73
4.3.2.2. Nickel and Chromium Equivalents of the Fourth Element Additions	75
4.3.3. Partitioning of Fourth Element Additions	80
4.3.4. Irradiation Damage	81
4.3.4.1. H.V.E.M. Irradiation	81
4.3.4.2. V.E.C. Irradiation	83
5. <u>Discussion</u>	85
5.1. Constitution	85
5.1.1. Microstructure of the Fe-Cr-Ni Base Alloys	85
5.1.2. The Attainment of Equilibrium	88
5.1.3. The Isothermal Sections of the Fe-Cr-Ni Ternary System	89
5.1.4. The Effect of Fourth Element Additions	90
5.1.4.1. Austenite Forming Elements (Mn,Cu,C and N ₂)	91
5.1.4.2. Ferrite/Sigma Phase Forming Elements (Si,Mo,Nb and Ti)	93
5.1.5. Nickel and Chromium Equivalents	94
5.1.5.1. Austenite Forming Elements (Mn,Cu,C and N ₂)	95
5.1.5.2. Ferrite Forming Elements (Si,Mo,Nb and Ti)	97
5.1.5.3. Comparison with Existing Equivalent Data	99
5.1.6. Partitioning of the Fourth Element Additions	102
5.1.7. Prediction of Phase Stability	104
5.1.8. Irradiation Damage	107
5.1.8.1. H.V.E.M. Irradiation	107
5.1.8.2. V.E.C. Irradiation	110
5.1.8.3. General Discussion of Results	111
5.1.9. Partitioning	114
6. <u>Conclusions</u>	116
6.1. Base Fe-Cr-Ni Ternary Constitution	116
6.2. Nickel and Chromium Equivalents of the Fourth Element Additions	117
6.3. Partitioning of the Fourth Element Additions	118
6.4. Electron Vacancy Phase Stability Predictions	119
6.5. Irradiation Damage	119
7. <u>Future Work</u>	120
7.1. Base Fe-Cr-Ni Ternary System	120
7.2. The Effect of Fourth Element Additions	121
7.3. Partitioning of Alloy Additions	123
7.4. Irradiation Damage	121
<u>References</u>	123

1 Introduction

The commercial application of materials based on the iron-chromium-nickel ternary system is widespread. The combination of high corrosion resistance, coupled with good high temperature strength and structural stability has produced materials suitable for a wide range of applications including the chemical industry, jet engines, steam turbines and power generation plant. Of particular interest is the use of stainless steels and iron-nickel based superalloys in nuclear fast reactors. It is important therefore that the constitution of the iron-chromium-nickel ternary system is clearly understood if alloys are to be designed that will maintain their mechanical properties throughout their working lives, particularly at elevated temperatures and under irradiation conditions.

The work which will be described was initiated to investigate the constitution of iron-chromium-nickel based alloys and also to study the possibility of replacing nickel by manganese and/or copper because of the disadvantages of the high nickel contents which are presently used in many stainless steels, which are:-

- (1) A pronounced tendency for low high temperature ductility,
- (2) A high capture cross-section for neutrons.
- (3) Production of long life radio-active species which tend to deposit in the heat-exchangers.
- (4) The high cost of nickel.

It must be noted that nickel however, has a pronounced effect in reducing the void swelling properties which is a major materials selection problem for fast reactor design.

The Fe-Cr-Ni system has been studied over a temperature range of 1150°C to 650°C because a good understanding of the base system was important if the effects of alloying additions and irradiation was to be understood and quantified. Base alloys have been equilibrated for long heat treatment times and a quantitative micro-probe analysis technique has been used to determine the constitution of the alloys. Work has been carried out on the transformations occurring during isothermal treatments, in an attempt to understand the equilibrium microstructures obtained and to investigate if any transitory phases are present at stages throughout the equilibrating heat treatment.

Other aims of the project have been:-

- (1) The investigation of minor alloying elements on the various possible structural features influencing the constitution and void swelling. Such features would be defect trapping by solutes, delta ferrite formation and the formation of topologically close packed phases.
- (2) To investigate the partitioning of alloying elements in duplex structures, which may influence the solute concentration in the austenite and hence the defect trapping capability.
- (3) To study the role of alloying additions such as silicon, titanium niobium and molybdenum, all of which stabilize ferrite and/or sigma, increase the N_v (electron vacancy) number, and yet have a pronounced effect in decreasing void swelling.
- (4) To examine the effectiveness of alloying additions in

promoting austenitic, ferritic or sigma phases, and if possible to quantify their effects by the use of nickel and chromium equivalence concepts. A procedure has been developed that compares directly the effect of an alloy addition with that of the nickel or chromium equivalent necessary to produce a similar change in microstructure. This was only possible because of the good understanding of the Fe-Cr-Ni system that was a primary aim of the project.

- (5) To investigate the effect of irradiation, using both electrons and heavy ions to simulate neutron irradiation, in order to study the effects of irradiation on selected alloys. The void swelling characteristics of the base ternary alloys and the series of alloys containing varying amounts of fourth element additions have been determined. The relative effects of various alloying additions under given irradiation conditions has allowed the effect of individual alloying elements on the void swelling characteristics of the base alloys to be determined. This is not possible for commercial alloys which may contain up to 8 deliberately added elements and many more trace elements.
- Also the effect of irradiation on the kinetics of the transformations occurring in these multi-phase systems has been investigated and shows a significant increase in transformation rate under irradiation conditions.

2 Literature Review

2.1.1. The Iron-Chromium-Nickel System

Several workers have studied the constitution of the iron-chromium-nickel ternary alloys. The establishment of four solid state equilibrium phases at temperatures above 650°C was published by Jenkins et al⁽¹⁾ and confirmed through Xray diffractometry by Bradley and Goldschmidt⁽²⁾:-

<u>Phase</u>	<u>Crystal Structure</u>	<u>Remarks</u>
Austenite (γ)	Face Centred Cubic	Generally based on the high nickel phase, although a high temperature allotrope of iron is faced centred cubic and denoted austenite
Alpha Ferrite (α)	Body Centred Cubic	The low temperature form of iron
Delta Ferrite (δ)	Body Centred Cubic	Generally refers to the high chromium phase but is also a high temperature allotrope of iron. There is no crystallographic difference between alpha and delta ferrite.
Sigma (σ)	Body Centred Tetragonal	A hard, brittle non-magnetic phase usually defined as FeCr but can dissolve significant amounts of nickel.

There are two general forms of the iron-chromium-nickel ternary diagrams between 650°C and the solidus. Above $\sim 950^\circ\text{C}$ there are two single phase regions based on chromium (δ) and nickel (γ) with a two-phase region ($\gamma + \delta$) between the (γ) and (δ) regions. Both phases are stable at high temperature and the duplex region persists to the solidus Fig. 1(a). Below $\sim 950^\circ\text{C}$

the isothermal sections became more complex. The two single phase regions are stable down to 650°C, particularly the austenitic phase, whilst a new constituent occupies a small single phase region at approximately Fe-Cr which is denoted sigma and is surrounded by two three-phase regions ($\gamma + \sigma + \delta$) and ($\gamma + \sigma + \alpha$) and three two phase regions ($\gamma + \sigma$), ($\sigma + \alpha$) and ($\sigma + \delta$), Fig 1(b). In commercial terms the important aspect of the ternary diagram is the extent to which the austenite is stable, particularly at lower temperatures. It is a general feature of the diagram that as the temperature decreases the alpha ferrite, delta ferrite and most importantly the sigma phase becomes stable at lower chromium contents. This effectively reduces the compositional range over which the single austenitic phase is stable.

Several workers have produced isothermal equilibrium diagrams in the temperature range from 650°C upwards. Andrews⁽³⁾ produced the most comprehensive set of data based on the known work up to 1950. A disadvantage of this early work is the impurities present in the experimental alloys. Work by Schafmeister and Ergang⁽⁴⁾ used alloys containing silicon which is a known sigma and ferrite former and raises the temperature at which sigma remains stable. Bradley and Goldschmidt⁽²⁾, whilst using a very comprehensive series of alloys, employed chromium of low purity ie chromium = 99.38% with the main impurities being nitrogen 0.20% and oxygen 0.488% max. Both nitrogen and oxygen are austenite formers and have a significant effect on the constitution of the alloys. It is probable that this level of impurity compared favourably with other workers at the time. Interestingly, work by Rees et al⁽⁵⁾ who used much purer ternary alloys produced by a melting technique in which hydrogen was a deoxidizer, presented constitutional data which

was in very good agreement with present day results. The isothermal constitutional diagram at 800°C published in the same work indicated that the γ -($\gamma + \sigma + \delta$) triple point was at a higher chromium level than had been previously suggested, Fig 1(c) and was consistent with this work. Cook and Brown⁽⁶⁾ using similar techniques to those used by Rees et al⁽⁵⁾, produced a constitutional diagram at 550°C which indicated, that sigma was an equilibrium phase at $\sim 16\%wtCr$, the γ -($\gamma + \sigma$) phase boundary rising slowly in chromium content as nickel is added. This work is in very good agreement with the constitutional diagrams that have been calculated thermodynamically for temperatures below 650°C by Kaufman et al⁽⁷⁾, Hillert⁽⁸⁾ and others. A critical review by Raynor and Rivlin⁽⁹⁾ has compiled the most recent constitutional work and highlights the differences in the phase boundary positions previously reported. Jones and Hume-Rothery⁽¹⁰⁾ and Hattersley and Hume-Rothery⁽¹¹⁾ made important contributions to determining the γ ($\gamma + \sigma$) phase boundary and the austenite triple point, and their results are reflected in the Raynor and Rivlin review⁽⁹⁾.

2.1.2 Experimental Techniques for Equilibrium Diagram Determination

A pre-requisite of all constitutional work is the manufacture of high purity alloys. The most reliable work has used argon arc vacuum button melting techniques to produce high purity ternary alloys, usually from high quality individual elements. Degassing techniques, using hydrogen⁽⁵⁾, have been employed since the purest chromium often contains high levels of nitrogen and oxygen.

The resulting alloys are then heat-treated, usually in silica tubes, under a partial pressure of argon. All workers have found that the approach to solid state equilibrium, particularly at lower

temperatures, is extremely slow. The use of prior cold work speeds up the approach to equilibrium but has the disadvantage of producing very fine microstructures, often with grains less than $1\mu\text{m}$ in size, that in themselves are very difficult to interpret with any certainty, and also difficult to analyse by any but the most sophisticated techniques.

The two most common techniques used for constitutional work are optical microscopy and X-ray diffraction work. Various etching techniques are employed in optical microscopy, designed to distinguish unambiguously the various phases present in the individual alloys. Many workers have experienced difficulty in distinguishing ferrite from sigma and have employed stain etches⁽¹¹⁾ such as 10N.K OH used electrolytically at 4 volts which stains ferrite orange, sigma bronze and does not stain austenite. There are though several disadvantages in that different thicknesses of stain produce different colours and identification of sigma or ferrite particularly when both phases occur as small precipitates is very doubtful by this technique. Jones and Hume-Rothery⁽¹⁰⁾ described an electrolytic potentiostatic method which distinguished the various phases by selective etching at particular potentials. It must be noted that the potential given for sigma (σ) and ferrite (α) is the same and cannot therefore distinguish between these phases if they occur in the same alloy. Furthermore whilst the work of Hattersley and Hume-Rothery⁽¹¹⁾ is in excellent agreement with that of other workers, Schultz and Merrick⁽¹²⁾ could not reproduce their etching technique.

The main X-ray technique used is the Debye-Scherrer powder camera, using filings of the experimental alloys⁽¹¹⁾. The filings

are taken before heattreatment and are usually sealed in silica tubes under argon. This method also gives an indication of the attainment of equilibrium since diffuse diffraction patterns indicate that equilibrium has not been reached. Also the cold work accelerates the approach to equilibrium. Several workers have confirmed their results by a qualitative magnetic technique which indicates whether there is a body centred cubic ferromagnetic phase present.

Recently Hasele et al⁽¹³⁾ have described a technique using diffusion couples to study the phase equilibria in ternary systems. The various elements are set up first as binary and then as a ternary diffusion couple by joining the metals, after electro-polishing, under dry hydrogen, followed by sealing in silica tubes under a third of an atmosphere of argon and heattreating at the appropriate temperature for a given time. The method allows the study of real ternary systems over a wide range of alloy compositions with a single sample. Phase compositions are claimed to be within 1% of the equilibrium composition obtained by prolonged heattreatment, although no mention of such times are given, nor is there any mention of phase identification. It would seem likely that quantitative microprobe analysis may be a phase identification technique in its own right given the large partitioning of chromium and nickel in the ternary system. The results agree well with those given by Schultz et al⁽¹²⁾.

The temperature working range for the core components of the fast reactors is 300-700°C, 700°C being the hot spots. This range unfortunately encompasses the void swelling range and as such, a knowledge of the constitution below 650°C is of paramount

importance. Experimentally this has proved very difficult for reasons already outlined, namely very slow diffusion rates of the elements leading to non-attainment of equilibrium. This problem has led to the development of calculation methods for predicting phase diagrams for temperatures where it is difficult to obtain experimental data. Classical work by Kaufman and Bernstein⁽⁷⁾ and Hillert⁽⁸⁾ have led to calculated equilibrium diagrams being published for the Iron-Chromium-Nickel system down to 500°C. The technique is complex but basically uses thermodynamic functions that have been determined experimentally, such as the Free Energy minimum whereby a phase change will occur. Very few experimental results are necessary to be able to calculate complete isothermal sections.

2.1.3 Effect of Alloying Elements

Stainless Steels are rarely simple ternary alloys, often containing more than 8 elements that have been deliberately added plus other minor elements that are either residuals or difficult to eliminate. It is well known that the composition of an alloy has a profound effect on many properties, eg. Ms, strength, ductility and creep properties. Many of the changes in properties are a direct result of a change in the constitution and or micro-structure of the alloy and it is this parameter, the effect of alloy additions on the constitution of iron-chromium-nickel ternaries, that the present work is largely concerned with.

Stainless steels cover a wide range of compositions leading to a variety of structures: austenitic, ferritic, martensitic and duplex, all of which can contain carbides and/or intermetallic compounds. Work by Irvine et al⁽¹⁴⁾ showed the effect of various

austenite formers and ferrite formers, Fig 2(a), after solution treatment at 1050°C on a 17wt%Cr 0.1wt%C alloy with 4wt%Ni added for the ferrite forming elements. It can be seen that nickel is the most potent of the substitutional austenite formers whilst small amounts of the interstitial elements carbon or nitrogen have large effects (nitrogen is not shown). Cobalt is useful generally, since whilst stabilizing the austenite it does not decrease the Ms, which is important for the martensitic stainless steels⁽¹⁵⁾. Cobalt though has serious disadvantages for uses in fast reactors in terms of the generation of radioactive isotopes and is not used in alloys destined for reactor core components. Copper and manganese, whilst producing some reduction in delta ferrite at lower concentrations, have little effect above about 4wt%. Also severe hot shortness problems may be encountered with copper. Lismar et al⁽¹⁶⁾ have described the effect of carbon on the microstructure in terms of a shift in the $\gamma-(\gamma + \sigma)$ phase boundary favouring the austenite. It must be noted that their experimental alloys contained silicon and manganese which may well affect their results. Also an isothermal treatment time of four hours was used for temperatures down to 950°C, probably resulting in the non-attainment of equilibrium.

Fig 2(b)⁽¹⁴⁾, shows the various potencies of the ferrite formers which are common additions to stainless steels. Many of these elements are also carbide/nitride formers, and only that proportion which is in solid solution will act as a ferrite former. The relatively small negative effects of copper, cobalt and manganese may well have been due to the presence of nickel which may have

affected their potency as austenite formers. Pryce et al⁽¹⁷⁾ studied the effect of silicon as a sigma former. They suggested that silicon is three times as potent as chromium as a sigma former. Again their alloys contain manganese whose role as an austenite former is dubious at lower temperatures. Nicholson et al⁽¹⁸⁾ worked with various alloys in an attempt to quantify the constitutional effect of silicon, manganese and molybdenum. They concluded that the effect of silicon was not linear in its equivalence to chromium, but varied in effect with nickel concentration, becoming less effective as nickel increased.

No firm conclusions were given although examination of their evidence would suggest that manganese is a sigma former at 650°C. They also suggested that the addition of 2wt%Mo displaced the $\gamma-(\gamma + \sigma)$ boundary by about 3wt%Cr towards lower chromium contents. Hattersley et al⁽¹¹⁾ studied the effect of titanium on the constitution of stainless steels and in common with other workers suggested that titanium stabilized ferrite and sigma, and indicated the results by the displacement of the $\gamma-(\gamma + \sigma)$ and $\gamma-(\gamma + \delta)$ phase boundaries. When the solubility of titanium was exceeded the intermetallic phase Ni_3Ti was precipitated. This will have the effect of reducing the amount of nickel in solid solution which will further increase the volume fraction of delta ferrite/sigma. Chromium equivalents for titanium, as measured by its effects on the $\gamma-(\gamma + \delta)$ and $\gamma-(\gamma + \sigma)$ phase boundaries are given as 1.2 at 1050-1150°C, 1.9 at 950°C and 1.3 at 700°C, this last figure reflecting the complication caused by the precipitation of Ni_3Ti .

Shao et al⁽¹⁹⁾ used thermodynamic methods to compare the ternary diagrams predicted by Kaufman et al⁽⁷⁾ with multi-component systems, using the compositions of commercial stainless steels ie, AISI 304, 316, 321 and 347. The results were shown by a shift in the phase boundaries in pseudo-ternary diagrams at 600° and 650°C. For all the alloys the tendency was to displace the γ -($\gamma + \sigma$) phase boundary to lower chromium levels particularly in the case of AISI 316, which contains a molybdenum addition but a higher nickel content, and AISI 347 (Nb stabilized). In this latter case, it was probably the depletion of carbon from solid solution that produced the effect. A comparison of this work with that of Nicholson et al⁽¹⁸⁾, who determined the constitution of stainless steels containing molybdenum, showed very good agreement with the predicted pseudo-quaternary alloys with only three experimental points lying in the wrong phase field. Shao⁽¹⁹⁾ also mentioned that the equivalents of the elements studied appeared to be dependent on the amount of the bulk elements present, particularly nickel, giving credence to the results of Nicholson et al⁽¹⁸⁾ who also reported varying values for the chromium and nickel equivalents.

2.1.4 Prediction of Constitution

It has been previously mentioned that commercial stainless steels can contain a number of additional elements, all of which will have some effect on the constitution. Many elements are added to perform specific functions such as stabilization, precipitation hardening or added corrosion resistance. Some knowledge of the effects of these additives is essential when designing stainless steels and predicting their properties.

Schaeffler⁽²⁰⁾ made an early attempt to characterise the effect of alloy additions with the publishing of the well known Schaeffler diagram, Fig 3(a). Whilst initially devised to predict the percentage of ferrite in weld metal, and thus the resistance to weld cracking, the diagram can be used in more general terms if treated with care. The nickel or chromium equivalent of an element is a measure of the potency of that element compared to either nickel or chromium, ie those elements which are austenite formers will have nickel equivalents and ferrite formers chromium equivalents. Schaeffler gave the following equivalents, but no indication of how they were determined:-

$$\text{Ni equ} = \%Ni + 0.5 \times \%Mn + 30 \times \%C \text{ -----(1)}$$

and

$$\text{Cr equ} = \%Cr + \%Mo + 1.5 \times \%Si + 0.5 \times \%Nb \text{ -----(2)}$$

A difficulty with the diagram is in the prediction of a martensitic phase. To do this on the basis of a nickel and chromium equivalent is to suggest that the various elements act with the same potency in their effect on the constitution of stainless steel as they do on the depression of the Ms (excepting cobalt). This has been shown by Pickering⁽¹⁵⁾ not to be the case. Delong⁽²¹⁾ has modified the Schaeffler diagram as shown in Fig 3(b) using the same equivalence factors, but also accounting for the effect of nitrogen which is reported to have a value of 30, the same as carbon. Price and Andrews⁽²²⁾ have published a Schaeffler type diagram pertaining to the constitution of stainless steels at the rolling temperature of 1150°C. Their equivalent equations are:-

$$\text{Ni equ} = Ni + 0.5Mn + 21C + 11.5N \text{ -----(3)}$$

$$\text{Cr equ} = Cr + 3Si + Mo \text{ -----(4)}$$

Pryce and Andrews⁽²³⁾ also published the chromium equivalents for titanium and niobium as 10 and 4 respectively, after taking into account the effect of carbon and nitrogen in decreasing the amount of the element dissolved in the alloy, ie Ti' and Nb':-

$$Ti' = Ti - 4 [(C - 0.03) + N] \text{ ----- (5)}$$

$$Nb' = Nb - 8 [(C - 0.03) + N] \text{ ----- (6)}$$

The value of 0.03%C was taken to be the solubility of carbon in the presence of titanium and niobium. Hammond⁽²⁴⁾ produced a modified DeLong diagram in which the delta ferrite percentage lines were not parallel and represented the constitution of stainless steels at ambient temperatures. The equivalent coefficients were those according to Schaeffler and DeLong.

Work by Jones et al⁽¹⁰⁾ suggested that the $\gamma+(\gamma+\sigma)$ phase boundary can be described as a function of temperature by the empirical equation:-

$$T = 70 + 38(\%Cr) - 6(\%Ni) + 50(\%Al) + 70(\%Ti) \text{ -----(7)}$$

where T^oC is the temperature below which an alloy of a certain composition will have sigma present as an equilibrium phase.

Eichelman and Hull⁽²⁵⁾ have prepared a table of equivalent coefficients based on the work of Thielemann⁽²⁶⁾, Newell et al⁽²⁷⁾ and Binder⁽²⁸⁾, to which has been added the work already reviewed here, and the data is given in Table 1.

2.1.5 Prediction of Sigma Phase Formation by Electron Vacancy

- Number Calculations.

Electron vacancy number calculations have been used to predict the formation of sigma phase in stainless steels and superalloys. The average number of unpaired electrons in metallic systems can be related to the tendency to form electronic compounds,

one of which is sigma phase. The method employed calculates the atomic concentration of the elements in the matrix of the alloy for which individual electron vacancy numbers have been determined. The criterion used has been determined experimentally in that the electron vacancy numbers have been calculated for a large number of commercial alloy whose constitution is known. It has been found that alloys whose electron vacancy number is greater than ~ 2.5 are sigma prone, whilst those below ~ 2.5 are not. The method has proved useful in alloy design and in the prediction of the void swelling characteristics of alloys.

2.1.5.1 Electron Vacancy Theory

In 1938 Pauling⁽²⁹⁾ published a paper that combined theory with experimental observations to provide a coherent explanation of the magnetic properties of the first long period transition elements Cr, Mn, Fe, Co and Ni. The electronic structure of these atoms is given below.

Electron Orbitals									
Element	Atomic No	1s	2s	2p	3s	3p	3d	4s	Atomic Diameter
Cr	24	2	2	6	2	6	5	1	2.57
Mn	25	2	2	6	2	6	5	2	?
Fe	26	2	2	6	2	6	6	2	2.54
Co	27	2	2	6	2	6	7	2	2.50
Ni	28	2	2	6	2	6	8	2	2.49

It is characteristic of the transition elements that the 3d shell, which can accommodate 10 electrons, remains only partially filled while some of the electrons have already occupied the 4s orbitals. Further, the atomic diameter varies only about 3% on moving from Cr to Ni.

Pauling interpreted these facts as meaning that the five d orbitals of each spin could be divided into 2.44 non-bonding orbitals and 2.56 bonding orbitals. The latter orbitals could

hybridize with p and s orbitals to account for metallic bonding. The 2.44 d-orbitals not required for bonding were then available for other events, and were essentially a measurement of the ability of an element to take part in other interactions. It has been postulated that the greater the number of unpaired electrons (electron holes) the greater is the ability of an element to form electron compounds, ie sigma phase.

2.1.5.2 Electron Vacancy Theory Applied to Alloys

In 1951 Rideout et al⁽³⁰⁾, whilst investigating the constitution of certain ternary systems (Cr-Co-Ni, Cr-Co-Fe, Cr-Co-Mo and Cr-Ni-Mo) found that the sigma phase extended over large regions in these systems. It had been previously suggested by Sully and Heal⁽³¹⁾ that sigma was an electron compound. Rideout et al⁽³⁰⁾ postulated that it should be possible to characterize the range of composition in which sigma phase would form by an average electron vacancy number (Nv) of the solid solution matrix, which could be expressed by a linear combination of terms:-

$$Nv = 4.66 (Cr + Mo) + 3.66 (Mn) + 2.66 (Fe) + 1.71 (Co) + 0.61 (Ni) \text{ ----- (8)}$$

where the elemental symbols represent the atom fraction of the corresponding elements and the numerals the individual Electron Vacancy Number for the elements.

Rideout went on to consider the results of other workers e.g. Pearson, Christian and Hume-Rothery⁽³²⁾, who had investigated the chromium-manganese system. It was concluded that manganese must be assigned a Nv_{Mn} of 3.3 rather than Paulings Nv_{Mn} 3.66 in order to obtain good agreement with the constitutional results. It became clear that the values of the individual Nv numbers for

certain elements were affected by the constitution of the system. Greenfield and Beck⁽³³⁾ have justified two values of N_v for vanadium, ie 5.66 with Ni and Co or 4.88 with Mn or Fe. In addition Greenfield and Beck⁽³⁴⁾ have shown that Nb and Ta, which, according to the theory should have equal N_v numbers, actually have distinctly different values when used individually in the Pt-Nb and Pt-Ta systems. Thus there may be a general compositional dependence of N_v numbers.

2.1.5.3 Application to Commercial Alloys

All the previous work which has been described was carried out on simple systems, that generally were solid-solutions. Further, the initial work was mainly aimed at predicting the $\sigma/(\sigma + \text{austenite})$ phase boundary. This has little or no use for commercial alloy designers since it is the austenite $/(\text{austenite} + \sigma)$ boundary that is of importance, σ usually being an undesirable phase. In 1963-64 two groups of workers, Slaney and Boesch⁽³⁵⁾ and Woodyatt, Sims and Beattie⁽³⁶⁾, independently made efforts to use the electron vacancy concept to predict the possibility of σ phase occurring in a particular commercial alloy, ie, the austenite $/(\text{austenite} + \sigma)$ phase boundaries. Both groups of workers developed the N_v concepts using nickel based superalloys.

Boesch and Slaney⁽³⁵⁾ applied electron vacancy theory to a nickel based Udimet 700 alloy. They implicitly assumed that σ would form from the austenite matrix, and that carbon depletion of the matrix could be ignored at the low ($\sim 0.05\%$ C) levels in the alloy. They went on to determine the residual austenite matrix composition by consideration of the elements

forming γ' , essentially $Ni_3(Al,Ti,Nb,Ta)$. An initial value for N_v was calculated using the base composition of a Udimet-500 alloy which had not precipitated sigma phase in a 1600 h rupture test, $N_v = 2.32$. Using this as an upper value, the method developed by Boesch and Slaney⁽³⁵⁾ has been able to produce sigma free alloys namely Udimet - 500 and 700.

The approach of Woodyatt et al⁽³⁶⁾, whilst following a similar pattern to that of Boesch and Slaney was far more general in its choice of alloys, and hence its application. The most technically significant difference between the two groups of workers is that Woodyatt et al⁽³⁶⁾ considered both nickel based alloys and steels, and also took account of all possible phases likely to be present in a particular alloy, thus extending Boesch and Slaney's⁽³⁵⁾ consideration of γ' to include mono- and complex carbides, borides, nitrides and other intermetallic compounds. By applying their model to 12 compositionally similar Udimet - 700 heats, which both did and did not form sigma, a range of N_v from 2.32 to 2.67 with a clear critical value for sigma formation near $N_v = 2.52$, was obtained.

2.1.5.4 Practical Electron Vacancy Calculations

Because of the complexity of the nickel based superalloys, the commercially used systems are all computerized, eg Phacomp⁽³⁷⁾. To determine the N_v number of an alloy it is necessary to determine the residual austenite matrix concentration. This can be done essentially in two ways.

1. To measure directly the composition using a micro-analytical technique.
2. Calculate the probable composition of the austenite based

on a knowledge of what phases will precipitate and how the individual elements will partition between them and the matrix.

Invariably the second method is used, particularly in the case of nickel based superalloys where, even when the most sophisticated methods are used, the experimental determination of the matrix composition is very difficult. Because commercial alloys commonly contain more than 12 elements, the calculations become complex and often are based on ambiguous assumptions. Nevertheless the results have proved adequate, and of real industrial value.

Palentine⁽³⁸⁾ has developed a computer program that predicts the composition of the alloy matrix based on experimental data and assumptions as to the form of carbide, nitrides and intermetallics that are commonly found in austenitic stainless steels and superalloys. The program determines the relative amounts of elements that are tied up in other phases and hence the remainder will represent the composition of the matrix. The program and its assumptions are extremely complex. Nevertheless the technique has been continuously updated and has provided useful data for the prediction of sigma phase.

In this work the alloy matrix compositions have been determined experimentally such that these often ambiguous assumptions have not been necessary.

2.1.6 Transformations in Stainless Steels

The complex nature of the compositions of commercial stainless steels leads to an extensive range of transformations that can occur. It is not the intention to review all the aspects of transformation but a review of the factors affecting the

transformations in stainless steels that are being considered for use in nuclear reactors is presented.

2.1.6.1. Transformations Occurring in Duplex Alloys

Beckitt⁽³⁹⁾ has published detailed work on transformations occurring in a duplex stainless steel having chromium and nickel equivalent values of 26 and 11wt% respectively. Solution treating at 1250°C produced a mixed microstructure of austenite with approximately 40% by volume of delta ferrite, in which condition a small dark precipitate was observed on the austenite/delta ferrite grain boundaries and was presumed to be $M_{23}C_6$. Aging for one hour at 700°C produced a cellular precipitate of $M_{23}C_6$ and new austenite on the austenite-delta ferrite boundaries. Increasing the aging time to four hours at 700°C produced laths of austenite growing into the delta ferrite grains, and these laths were sometimes in contact with the austenite-delta ferrite grain boundaries or occurred as isolated precipitates within the delta ferrite. No evidence of the cellular structure was evident and only small $M_{23}C_6$ particles were observed on the austenite-delta ferrite grain boundaries. Dispersed between the austenite laths at the grain boundaries were large irregular particles identified as the iron-chromium sigma phase. The austenite laths in contact with the austenite-delta ferrite boundary invariably showed the same orientation as the austenite grain and grew along a $[211]$ preferred direction, conforming to the well known Kurdjumov and Sachs orientation relationship namely:-

$$\begin{array}{l} \{111\} \delta // \{110\} \gamma \\ [110] \delta // [111] \gamma \end{array}$$

The Sigma, whilst having no preferred orientation relationship with the adjoining delta-ferrite did adopt an orientation relationship

with one of the austenite colonies with which it was initially in contact, this being:-

$$\begin{aligned} (111)_\gamma & // (001)_\sigma \\ \langle 110 \rangle_\gamma & // \langle 110 \rangle_\sigma \end{aligned}$$

After 25 hours the majority of the remaining delta-ferrite had transformed to an aggregate of sigma and austenite.

Aging at 900°C produce no sigma, and Beckett concluded that 900°C was above the temperature at which sigma is stable. This is now known to be incorrect and the alloy which was used according to recent constitutional work⁽⁹⁾ will lie in the austenite + alpha ferrite phase field. After one hour the carbides present after solution treatment had grown and produced a cellular precipitation with new austenite growing into the ferrite and having an orientation relationship of:-

$$\begin{aligned} (100)_\gamma & // (100)_{M_{23}C_6} \\ \langle 100 \rangle_\gamma & // \langle 100 \rangle_{M_{23}C_6} \end{aligned}$$

Further aging had the effect of increasing the amount of new austenite and coarsening the microstructure. Beckett also produced a 'C' curve for the kinetics of the growth of sigma in these alloys which is shown in Fig 4. Pickering⁽⁴⁰⁾ has also studied the formation of sigma in two steels based on 25%Cr-15%Ni with the carbon, manganese and silicon adjusted so that one was austenitic and the other duplex. It was confirmed that sigma precipitated much faster in the duplex alloys and its nucleation was associated with $M_{23}C_6$, which presumably occurred by a cellular type reaction and formed a nodular structure, observed in the austenitic alloy. In the case of the duplex alloy the delta ferrite transformed to an aggregate of austenite and sigma which grew inwards to consume the whole

delta ferrite grain. It seems likely that the precipitation of phases containing high levels of chromium must play a part in the nucleation of sigma.

Southwick et al⁽⁴¹⁾ studied the decomposition of ferrite to austenite using a 26%Cr, 5%Ni, 1.3%Mo, 0.7%Mn, 0.6%Si, 0.03%C alloy. Solution treatment at 1300°C was sufficient to redissolve the austenite and carbides leaving a single phase ferrite structure. Aging at 1200-650°C resulted in the transformation of ferrite to austenite by a nucleation and growth process at both grain boundaries and within the matrix. At temperatures between 300-600°C austenite was formed by a martensitic or shear type transformation. A scanning transmission electron microscope attachment was used in conjunction with an energy dispersive analyser to confirm that there was no difference in the concentrations of the bulk elements for the body-centred cubic phase and the face centred cubic phase. A clear difference was shown however between the composition of the austenite that had transformed by nucleation and growth at higher temperature and that of the ferrite.

2.1.6.2 Carbides

Specifically $M_{23}C_6$ is the common carbide formed in stainless steels and is generally based on chromium although iron and molybdenum are known to substitute when these elements are present. The $M_{23}C_6$ is commonly described as $(Cr,Fe,Mo)_{23}C_6$. Work by Tuma et al⁽⁴²⁾, cited in ref. (43), has studied the solubility of carbon in austenite and concluded that whilst the solubility is quite high at homogenisation temperatures, e.g. 0.1 wt%C at 1100°C, it becomes vanishingly small below ~700°C.

Also the effect of nickel is to reduce the solubility of carbon particularly at higher temperatures. Rapid quenching will then produce a supersaturation of carbon in austenite at room temperature. Unfortunately stainless steels are often required to work at elevated temperatures with the inherent problems of carbide precipitation. Elements are often added to stainless steels to stabilize the carbon, niobium being commonly used and forming a eutectic with austenite, ie $\text{Liquid} \rightarrow \gamma + \text{NbC}$. This then effectively removes the carbon from solution and alleviates the problem of chromium carbide precipitation. Titanium is another commonly used stabilizer. The other aspect that must be considered is the ferrite/sigma forming tendencies of these elements and the indirect ferrite/sigma forming tendency of reducing the carbon in solid solution thus making it necessary to add further austenite formers to maintain a fully austenitic structure. Nitrogen behaves similarly to carbon in this respect.

The other use for the MC type carbides is as precipitation strengtheners, the difference being in the heattreatments. A high solution temperature is used to dissolve as much of the carbon, titanium, niobium or molybdenum as possible. There is a limit however, due to the increased temperature producing a coarse grain size and in practice a compromise is made such that some randomly distributed MC type carbides remain undissolved. An aging heattreatment is then used to provide a fine intragranular precipitate of MC that acts to strengthen the alloy.

2.1.6.3 Intermetallic Phases

Again the complexity of stainless steel compositions lead to a variety of intermetallic phases that can be present at

temperatures between 600-1150°C. The presence of these topologically close packed phases in quite small amounts is generally deleterious to the low and high temperature properties, including ductility, strength and creep strength. They can act to produce easy paths for fracture, and can deplete both the grain boundary and matrix of important solid solution elements and produce undesirable hard phases at the grain boundaries.

Whilst no quantitative assessment has been made of the type or morphology of intermetallic phases that can precipitate over the range of stainless steel compositions, Decker⁽⁴⁴⁾ has published a chart, given in Table 2, that indicates the major types of intermetallic compounds that occur between the various elements present.

Sigma Phase (Tetragonal, Fe-Cr; $a_0 = 8.7995\text{\AA}$ $c_0 = 4.5442$ ⁽⁴⁵⁾),
This is the most important phase since it is an equilibrium phase in the iron-chromium-nickel system, has a wide compositional range and is the primary reason why the amount of chromium in austenitic stainless steels is limited to ~ 20wt% if other austenite forming elements are not present. Sigma is generally quoted as FeCr but can be FeMo or a combination of these elements, it can also dissolve significant quantities of other elements.

Chi phase (Body Centred Cubic; $\text{Cr}_6\text{Fe}_{18}\text{Mo}_5$; $a_0 = 8.920\text{\AA}$ ⁽⁴³⁾)
This phase can be precipitated over a wide range of compositions and as can be seen from Table 2, it can contain a variety of elements and is generally stable to much higher temperatures than sigma.

Laves phase (Hexagonal; Fe_2Mo ; $a_0 = 4.744\text{\AA}$, $c = 7.257\text{\AA}$ ⁽⁴³⁾)
This is a common intermetallic phase in stainless steels, and whilst based on Fe_2Mo can dissolve various elements and has been

given a much more general formula by Sullivan et al⁽⁴⁶⁾ of $(\text{Fe, Mn, Cr, Si})_2 (\text{Mo, Ti, Nb})$. Silicon and niobium are suggested to promote directly the Laves phase formation. Attempts^(47,48) have been made to use Laves phase as a precipitation strengthener and although strengthening can be achieved, premature cracking is often associated with Laves phase at the grain boundaries.

Other intermetallic phases such as Mu and G phase have been reported but are more generally found in nickel based superalloys.

2.1.6.4 Coherent Intermetallic Phases

The coherent type of intermetallic compounds that are precipitated purposefully in stainless steels are $\text{Ni}_3(\text{Ti Al}), \gamma'$ and $\text{Ni}_3(\text{Nb Ta}), \gamma''$, both having a stable and metastable occurrence. Their primary use is in high temperature creep resisting steels with the fine coherent intermetallic particles providing matrix strength by their inhibition of dislocation movement. Interestingly, the stable form of the $\text{Ni}_3(\text{Nb Ta})$ precipitate, which is orthorhombic in structure as opposed to the face-centred cubic nature of the metastable phase, precipitates at the grain boundaries, pinning the grain boundaries and providing further resistance to creep in much the same way as M_{23}C_6 does in other creep resisting steels. This can be doubly useful in that chromium is not removed from solution and hence the corrosion and oxidation resistance of the alloy is not impaired.

2.1.7 The Effect of Irradiation on the Constitution

It has been pointed out by several workers that the constitution of irradiated stainless steels is not what would be expected from a knowledge of the phase diagrams. Kaufman et al⁽⁴⁹⁾ have been unable to detect the presence of sigma phase

in M 316 type fuel pin cladding irradiated in the Dounreay Fast Reactor (DFR) at temperatures up to 700°C, although this phase is frequently observed in this alloy in unirradiated conditions. Instead an ordered face-centred-cubic phase has been discovered in alloys irradiated at temperatures below 550°C. This phase is thought to be $Ni_3(Fe,Mn)$ or Ni_3Si . A similar phase is predicted to occur by the calculated phase diagrams below 550°C but not in the M 316 compositional range. The paper by Kaufman et al⁽⁴⁹⁾ also cites other workers (Bilsby) who has also noted the ordered face-centred-cubic phase and the absence of sigma in irradiated M 316 alloys. It is also significant that under normal circumstances M 316 type stainless steel does not exhibit ferro-magnetism although many reports exist to suggest that after irradiation alloys of this type are slightly ferro-magnetic. Brown et al⁽⁵⁰⁾ have, suggested that the ordered $Ni_3(Fe Mn)$ phase may in some part be responsible for the ferro-magnetism, although he points out that alloys not containing the phase are also magnetic. Baron et al⁽⁵¹⁾ found abnormal magnetism in a low carbon 316 alloy and tentatively suggested that the magnetic behaviour may be due to the formation of a body-centred-cubic phase caused by the presence of hydrogen formed by (n-p) transmutations with the major alloying components. They did not however produce direct evidence for this effect. Kaufman et al⁽⁴⁹⁾ have summarised the observed phenomena and proposed possible reasons for the following effects:-

1. The non-appearance of sigma phase at temperatures and times where this would normally be observed without irradiation.
2. The appearance of an ordered phase in a compositional range

and at a temperature where it would not normally be observed without irradiation.

3. The appearance of ferro-magnetism after irradiation both in the presence and absence of the ordered phase.

The possible explanations for the observations were:-

1. That irradiation brings about the true equilibrium structure in these alloys by enhancing diffusion, which under normal circumstances would be very slow at the temperatures in question.
2. That irradiation changes the relative free energies of the various phases by differentially increasing the concentration of defects.
3. That irradiation inhibits the formation of some phases by bombardment processes which physically knock precipitate atoms back into solution.

2.1.8.1 Void Swelling

The phenomenon of void formation in irradiated materials was predicted in 1959 by Greenwood et al⁽⁵²⁾ and was first observed experimentally in 1966 in austenitic stainless steel irradiated in the Dounreay Fast Reactor, as reported by Cawthorne and Fulton^(53,54) Void formation in austenitic material can cause swelling of > 20%, causing severe engineering problems when used as core-reactor components, and because of this has been the subject of extensive investigations.

There is now general agreement on why voids nucleate and grow in non-fissile metals and alloys⁽⁵⁵⁾. Essentially, void swelling occurs through a supersaturation of vacancies and interstitials resulting from energetic neutron-atom collisions.

Dislocations, energetically, have a slightly higher preference for interstitials than for vacancies, thought now to be of the order of 10%. The excess vacancies migrate and form clusters which are stabilized by the residual gases in the material or by gases produced by irradiation. The temperature dependence of void swelling, typically in the range 350°C-700°C, is due to the fact that below $\sim 0.3 T_m$ the mutual recombination of interstitials and the slowly diffusing vacancies is dominant. Conversely above $\sim 0.5 T_m$ the thermal vacancy concentration exceeds that induced by irradiation.

Several early fast reactors were designed before the void swelling phenomenon was observed but were operated effectively below the void swelling temperature range. This range however embraces the current temperature range for the large commercial fast reactors. Developments over recent years have shown that the most severe void swelling occurs in the sub-assembly wrappers which are generally constructed of austenitic stainless steel or iron-nickel based superalloys. The degree of swelling is dependent on temperature and neutron flux, and both parameters can be non-uniform. It is known that the neutron flux shows considerable variation across the hexagonal wrappers at the edge of a fast reactor. Respective doses across a wrapper, as reported by Harries⁽⁵⁵⁾, are 52 and 19 d.p.a. (displacements per atom), thus resulting in significant differences in void swelling rate and hence causing bowing of the sub-assemblies. It has been estimated by Anderson⁽⁵⁶⁾ that a cold worked austenitic steel wrapper will deflect by approximately 25 millimetres from the vertical at its shoulder.

2.1.8.2 Void Formation

There is no precise mechanism known for the nucleation and growth of voids in crystals. Mayer and Brown⁽⁵⁷⁾ have discussed in some detail in a series of papers the known damage processes during irradiation. Irradiation produces Frenkel defects, which are single interstitial atoms or vacancies, together with the possibility of a vacancy rich volume at the end of the paths of energetic ions or atoms. The majority of Frenkel defects recombine, that is interstitials migrate randomly and are annihilated at vacancies. However some point defects meet like defects and form clusters. Because interstitials are considerably more mobile than vacancies, the clusters that are formed are predominantly interstitial in nature; further migration increases the size of these interstitial clusters but it decreases the size of any vacancy clusters. The interstitial cluster is generally a two dimensional platelet, i.e. a dislocation loop. Thus in the absence of voids the outcome of irradiation damage is a population of large interstitial loops, together with a population of smaller vacancy clusters, the number and size of which depends on the temperature and type of irradiation.

At elevated temperatures the population of interstitial loops coarsens and both glide and climb take place with the result that a dislocation network is eventually formed. If there is no preferential absorption of point defects at sinks then the flow of interstitials will prevent the growth of vacancy clusters up to long irradiation times. However it is generally accepted that interstitials are preferentially absorbed at dislocations, due to the very large elastic strains associated

with self-interstitial atoms. This bias factor allows a net vacancy flow to relatively unstrained vacancy clusters, especially to voids. It is important to note that the growth of interstitial loops provide the dislocations which act as biased sinks.

The method of void nucleation from the vacancy clusters is not understood. Greenwood et al⁽⁵²⁾ in the earliest work on gas bubbles arising out of the formation of fission gases in nuclear reactors, suggest that the coalescence of two gas atoms could result in the nucleation of a bubble. A gas bubble implies that the interfacial energy created by the nucleation of a bubble is balanced by the pressure of the gas inside; this is not the case for a void since it is known that insufficient gas is created to equilibrate the observed voidage. Nevertheless it has been shown⁽⁵⁸⁾ that in very pure face-centred-cubic metals which are thoroughly outgassed, no voidage occurs, whereas an implantation of helium in the same alloy produced voids on irradiation. It seems quite clear that residual gases and gases created by irradiation interactions play an important role in the nucleation of voids.

2.1.8.3 Simulation Techniques of Neutron Irradiation

There are two main methods of simulating neutron irradiation:-

1. The high voltage (1MeV) electron microscope, which uses energetic electrons to displace atoms within a thin foil of material.
2. An ion accelerator used to produce energetic ions i.e. 22MeVC⁺⁺ ions or 46.5MeVNi⁶⁺ ions, which at the same time can inject helium to simulate the production of helium and other gases by neutron irradiation.

The wrapper and cladding material in a commercial fast reactor will have to withstand ~ 100 d.p.a. of neutron irradiation throughout its working life. Considering that the dose rate per year in the Dounreay Fast Reactor is 20-25 d.p.a. one can imagine the difficulties when studying high dose irradiations if they take four years to reach ~ 100 d.p.a. Coupled with this is the fact that accurate determination of dose and temperature is virtually impossible, as well as the fact that considerable cycling of the reactor occurs during its working life. Accelerators and High Voltage Electron Microscopes (H.V.E.M.) have dose rates which are of the order of 1000 times higher than those experienced in a fast reactor and thus can reach relatively high doses in a matter of hours. There is then a definite advantage to be gained using accelerators and H.V.E.M's for the study of irradiation damage. If the results of these simulation techniques are to be useful then they must be comparable to the case for neutron damage. Nelson et al⁽⁵⁹⁾ have reviewed the use of accelerators to simulate fast neutron induced voidage in metals and highlighted the physical differences encountered using these methods. Firstly the fundamental difference between fast neutrons and charged particle irradiation is the elastic scattering cross-section; neutrons have a cross section in the order of 10^{-24} cm² whereas the cross-section of charged particles is in excess of six orders of magnitude greater. The consequence of this is the difference in mean free path length between successive collisions; for fast neutrons this is of the order of centimetres whilst for charged particles it can be as small as 100\AA . Thus damage by fast neutrons will be uniform throughout the specimens

whilst charged particles will have a damaged surface layer roughly equal to the particle range in the solid. In the case of the H.V.E.M , the electrons produce uniform damage through the foil except for the surface layers which do not produce voidage due to the surfaces acting as sinks for the generated defects. Both neutron and heavy particle collisions result in the production of cascades of defects which are thought to be important in the formation of a dislocation structure and hence voidage, which has already been covered in section 2.1.8.2. However in the case of electrons only one atom can be displaced by any one electron and this should be born in mind when comparing H.V.E.M. irradiation with neutron irradiation. On the other hand it is thought that the most important parameter is the total number of displacements, and thus any difference in the primary recoil spectra may be of secondary importance.

The choice of charged particle is also important since the depth of penetration depends critically on particle mass and initial energy. Probably the best results would be obtained using 4MeV protons, the elastic scattering cross section of which is low and would therefore produce a uniform damage layer through a 25 μ m thick specimen. However we again approach the situation for neutron irradiation in that the dose rate will be excessively slow. 20 MeV C^{++} ions have been commonly used but care must be taken since the damaged layer of the specimen will have an increased carbon content and it is well known that void swelling is critically dependant on the constitution and therefore on the composition. In view of this a major constituent of the alloy to be irradiated would be favored, which, in the majority of cases.

would be 100MeVFe^+ ions, although there is no accelerator that can produce this ion at a sufficiently high flux to cause heavy damage. Generally 46MeVNi^{6+} ions are used giving a good compromise between damage layer thickness and depth of penetration.

2.1.8.4 The Effect of Constitution and Microstructure on Void Swelling

The dependence of the swelling behaviour on constitution and microstructure has been investigated by several workers, including Harries⁽⁶⁰⁾. The temperature dependence is indicated in Fig.5 which shows percentage swelling plotted against irradiation temperature for Type 316 stainless steel, and indicates the effect of cold work on the swelling behaviour. These results have been obtained using the Dounreay Fast Reactor (D.F.R) with an irradiation dose of 44 d.p.a. The cold worked materials swell considerably less than the solution-treated materials and show one definite peak at $475 \pm 25^\circ\text{C}$ as opposed to the twin peaks of the solution treated samples. Williams et al⁽⁶¹⁻⁶³⁾ have simulated neutron irradiation by both H.V.E.M. and V.E.C. techniques for FV 548 and 316 alloys, and have found very comparable results although the peak swelling occurred at higher temperatures using the simulation technique. This is expected and is thought to be due to the different dose rates employed, i.e. 10^{-6} displacements per atom per second for neutrons and 10^{-3} displacement per atom per second for charged particles. This behaviour is however not consistent for all types of material. For example Type 321 stainless steel will exhibit increased swelling in the cold worked condition as opposed to the solution treated material⁽⁶⁴⁾.

The void swelling-dose relationships are shown in Fig.6 and confirm the behaviour of the solution-treated versus the cold worked structures. The differences in Type 316 and 321 steels are thought to be due to the different types of precipitates associated with each material, i.e. $M_{23}C_6$ in 316 and TiC in 321. Also there is the probability of a martensitic transformation induced by cold working in the Type 321 stainless steels, which is less stable with respect to strain induced martensite than is Type 316.

It is now well established that the austenitic alloys exhibit a wide range of void swelling behaviour. The higher nickel alloys such as Nimonic PE16 show a relatively high resistance to void swelling^(65,66). There is also evidence^(64,67) to suggest that the ferritic/martensitic steels of the 12%Cr types have a high resistance to void swelling when studied by simulation techniques, i.e. H.V.E.M. and V.E.C. irradiation. Such studies have shown that negligible swelling occurs in these ferritic materials up to 500°C when irradiated up to ~ 90 d.p.a.

It is obvious that the matrix composition will have a dominating influence in determining the void swelling characteristics of austenitic alloys. The effects of composition for pure Fe-Ni-Cr alloys and commercial austenitic steels have been investigated^(68,69,70). Increasing the nickel content above ~ 20% dramatically reduces void swelling, Fig 7. This decrease is due primarily to a reduction in void concentration, the void size remaining essentially constant.

It is clear that the formation of a second or third phase, namely ferrite or sigma, has a large effect on void swelling.

Evidence to support this has been obtained from a series of pure Fe-Ni-Cr alloys and commercial stainless steels using 5MeV Ni²⁺ ion irradiation^(68,70). The compositions are shown on the 450°C isothermal section of the Fe-Ni-Cr system, Fig 8. Alloys within the two and three phase regions exhibit higher void swelling. Recent work on the Fe-Ni-Cr system indicates that the γ -($\gamma + \sigma$) phase boundary stretches to lower chromium contents than suggested by the published work of Hattersley and Hume-Rothery⁽¹¹⁾. Further evidence of the dependence of void swelling on the constitution has been given by Watkin et al⁽⁷¹⁾. Using isothermal sections calculated from thermodynamic principles⁽⁷²⁾ for low temperatures of 400-600°C it was shown that swelling at these temperatures is a maximum in a three phase field, a minimum in the single phase austenitic field, and had an intermediate value in a two phase region⁽⁷³⁾.

It has been postulated that the reason why interstitial and substitutional solutes reduce void swelling is that they provide sites for trapping defects which would otherwise accumulate to produce voids. When other phases are formed such as sigma or ferrite, which may well have the ability to preferentially partition the solute atoms, the defect trapping sites may well be lost. Hence the formation of sigma or ferrite that are suggested to partition these solute atoms has the effect of increasing void swelling.

The case of silicon, in solution as a substitutional solute within the austenitic matrix is known to reduce the void swelling. However at elevated temperatures the phase Ni₃Si will precipitate and remove the silicon from solution thereby reducing its effectiveness in reducing void swelling.

The void swelling of Fe-Ni-Cr alloys and commercial austenitic steels has been correlated with electron vacancy concentration of the matrix^(73,74), stacking fault energy⁽⁷⁴⁾, partial diffusion coefficient⁽⁷⁵⁾ and shear modulus⁽⁷⁶⁾. Fig 9 shows the relationship between electron vacancy number (N_v) and the % swelling for various commercial austenitic stainless steels and nickel based alloys. The graph indicates that below a critical N_v , negligible void swelling occurs whilst above this value swelling increases with increasing N_v ⁽⁷⁴⁾. An analogous situation is seen to exist between the stacking fault energy (SFE) and void swelling. The observed critical values of N_v and SFE for the transition from low to high swelling behaviour probably indicate the compositions at which structural changes take place from single phase γ to the two phase ($\gamma + \alpha$) or ($\gamma + \sigma$) regions, or the three phase field ($\gamma + \alpha + \sigma$) region. This hypothesis provides further evidence in favour of the view that constitution, particularly ferrite and sigma phase, play a major role in controlling void swelling.

2.1.8.5. Effect of Minor Elements

It is now well known that minor alloy additions suppress void swelling in pure metals and alloys. It has been demonstrated that commercial Type 316 will swell some 20-50 times less than a pure Fe-Ni-Cr-Mo Alloy that approximates to the base composition of Type 316⁽⁷⁷⁾. These results are consistent for relatively low irradiation doses, but when higher doses are applied the difference in swelling between the commercial and pure alloys is less marked⁽⁷⁰⁾. It has been suggested therefore that elements such as carbon, manganese, sulphur, molybdenum and silicon retard

both the nucleation and growth of voids⁽⁷⁷⁾. This does not however account for the behaviour at higher doses. It may well be that the influence of these minor elements is confined mainly to the suppression of the nucleation of voids rather than to the growth mechanism. Whilst there is no complete agreement on the relative effects of all the various minor elements, there is now general agreement that silicon has a major effect in reducing void swelling^(78,79). Also other elements (phosphorus, manganese, molybdenum, copper and cobalt) in low dose neutron irradiated Type 316, have been effective in suppressing void swelling. Carbon^(44,80,81) has also proved to be effective in reducing the void swelling along with Ti, Zr and Nb⁽⁷⁰⁾. Furthermore it appears that a combination of silicon and titanium is far more effective in reducing the swelling than a single addition of either element⁽⁷⁰⁾.

The effect of carbon in suppressing void swelling is most pronounced at the lower temperatures^(64,65,82) whilst silicon appears to be most effective at the higher temperatures⁽⁷⁰⁾. It must be noted though that all these minor alloying elements are only effective whilst in solid solution. Thus precipitation of carbides by aging increases the void swelling of cold worked Type 316 steel⁽⁸³⁾. Conversely in Type 316 steel, increasing the solid solution concentration of carbon in the austenitic matrix by raising the solution-treatment temperature decreases the void swelling⁽⁸⁴⁾.

The low void swelling exhibited by Nimonic PE16 was initially attributed to the precipitation of the coherent γ' phase, $Ni_3(Ti,Al)$, and enhanced point defect recombination at the coherent interface of the austenite and γ' ^(80,81). It is now known that the

resistance to void swelling is dependent on the matrix Fe-Ni-Cr composition, since equally low void swelling characteristics are shown by a Nimonic PE16 composition that contains no aluminium or titanium additions^(64,68).

The influence of carbides and other types of precipitate on void swelling is not clear, although transmission electron microscopy indicates that voids are often associated with such phases in irradiated austenitic alloys.

3 EXPERIMENTAL METHODS

3.1 The Experimental Alloys

The work itself is concerned with the constitution of stainless steels and the effect thereon of various addition elements. It was imperative therefore to manufacture ternary alloys of compositions relevant to the commercially important areas of the iron-chromium-nickel system. Three series of alloys were chosen, the compositions of which are given in Table 3. Series 1 comprises two constant iron contents, the nickel and chromium contents being adjusted so that the series crossed the $\gamma-(\gamma + \delta)$ phase boundary at high temperatures of 1150-950°C and the $\gamma-(\gamma + \sigma)$ phase boundary below 950°C. Series 2 and 3 were alloys of constant chromium content, namely 12wt% and 18wt% respectively. These chromium contents are those of commercial importance and the series of alloys chosen cross the $\alpha-(\alpha + \gamma)$ and $\gamma-(\alpha+\gamma)$ phase boundaries.

3.2 Manufacture of the Base Experimental Alloys

The University of Sheffield were approached to provide suitable high purity base ternary alloys. The alloys provided were 750g casts of high frequency vacuum melted material having the compositions listed in Table 3. The ingots made were 25mm diameter and \sim 15cm long, and were cleaned by turning off the surface. They were then milled into 19mm square sections, the millings being saved for analysis and for further sample preparation of button melts to which alloy additions were made. The milled bars were then hot rolled at an initial temperature of 1100°C from 19mm to 13mm thick in two passes, reheated and further reduced to 6mm thickness in a further two passes. The bars were then cold rolled to 3mm thick strip using two passes, the final material

being 3mm thick x 25mm wide and ~40cm long. The material in this cold rolled condition was then ready for heat treatment.

3.3 Manufacture of Quaternary Alloys

An existing argon arc button melter was used to produce high purity quaternary alloys using the base materials produced by the University of Sheffield and a number of single element additions as given in Table 4. Several problems arose from the use of the apparatus in its standard form, namely; the alloys were heterogeneous particularly if elements of a high melting temperature were used, the level of nitrogen (~ 0.10wt%) was unacceptably high, and only 25-30gms of material could be made in one melt. These problems were overcome by (1) a modification to the copper hearth as shown in Fig 10 in which the cruciform nature of the melting channel allowed for triple remelting from the upper channel to the lower which promotes mixing, and (2) the vacuum system and argon flushing apparatus was adjusted to permit a constant flow of argon at one third atmosphere to pass through the melting chamber. This effected a continual reduction of the partial pressures of nitrogen and carbon monoxide thus refining the melt, such that levels of carbon and nitrogen could be kept below 0.005wt%. This purity was achieved in the majority of melts. The modified copper hearth had an increased capacity of 50gms of material.

The slugs produced by the argon arc melting were then ground clean and machined to 6.25mm diameter by ~ 5cm long. Homogenisation at 1150°C was carried out under argon in silica tubes for 24 hrs prior to cold working, which was necessary to

accelerate the attainment of equilibrium, the bars being swaged to 3.12mm diameter before final machining to 3.0mm diameter x 20cm long.

3.4 Heattreatment

The basis of the work was to investigate the equilibrated constitution of the iron-chromium-nickel system at temperatures down to 650°C. All the heattreatments were carried out under argon in sealed silica tubes. In the main, tube furnaces were used giving an adequate hot zone with a temperature variation of $\pm 2^\circ\text{C}$ of the heattreatment temperature, the only disadvantage being that only one sample could be treated at any one time. The subsequent building of special muffle furnaces in which up to three silica tubes could be positioned in a hot zone constant in temperature to $\pm 3^\circ\text{C}$ greatly assisted with the long time heattreatments. After the required heattreatment duration, the sample was quenched into ice water and the silica tubes broken. Single heattreatment times of up to 800hrs were used.

3.5 Metallography

The determination of the microstructure is of paramount importance in constitutional work and several methods were used to investigate the phases present and their morphologies.

Optical Microscopy

Standard polishing techniques down to $\frac{1}{4}\mu\text{m}$ diamond were used to prepare the specimens for optical microscopy. The optical microscope used was a Ziess projection microscope with magnification up to 1000x. Etchants used were as follows:

1. Oxalic Acid

10% by weight used electrolytically at ~ 4 volts with a

Pt electrode in contact with the specimen whilst a stainless steel electrode was passed over the specimen; this method eradicated the rather selective etching achieved with a static stainless steel electrode. This etchant was very good for the general micro-structure and outlines the austenite-ferrite and austenite-sigma boundaries well. It was not good however for boundaries within the same phase, i.e. austenite-austenite or ferrite-ferrite boundaries were at best poorly outlined or even unaffected. Carbides of the $M_{23}C_6$ type were stained black.

2. Potassium Hydroxide (10N)

Used electrolytically at a potential of ~ 4 volts and a similar technique to that used for oxalic acid. This etchant was a stain etch and produced a variety of colours for the ferrite and sigma phases, whilst the austenite remained unstained. A light etch would result in the ferrite/sigma becoming initially blue or green and then becoming a yellow bronze colour at longer etching times when the surface films were thicker. At all conditions the stain produced on the sigma was slightly deeper and the etch could therefore distinguish to some degree the sigma from the ferrite. However when only one of these phases was present, usually with austenite, it was impossible to distinguish which phase it was since no comparison could be made. Also the stain films were fragile and care had to be taken in the preparation of these samples particularly if quantitative volume fraction analysis was to be carried out.

3. Chemical stain (30gKFe (30gKFeCN, + 30gKOH + 60ccH₂O)

This chemical stain etch was used boiling, and produced very similar results to the electrolyte KOH. However the solution

became quickly exhausted; in general the potassium hydroxide etch was preferred for convenience.

Both "Schafmeisters Reagent" and "Glyceregia" were used but proved ineffective in etching these alloys.

3.6 Quantitative Analysis of the Constitution

In order to study the effects of various additions to stainless steels, their effects in terms of transformations and constitutional changes must be quantified. The effect of austenite or ferrite/sigma formers on the bulk constitution was determined by the change in the relative amounts of the phases present. The change in the volume fraction of a particular phase, as a result of a fourth element addition, was a measure of the "potency" of the austenite or ferrite/sigma forming tendency of that element.

It has been shown that the volume fraction of a particular phase is equal to the point fraction of the phase, the point fraction being a relatively easy parameter to measure⁽⁸⁵⁾. A two dimensional systematic grid was laid down on the projection screen of a Ziess microscope. The intersection of the grid lines were deemed to be the points. A suitable magnification was chosen which was as high as possible subject to there being on average only one point in any one particle or grain of the phase to be counted. The points were scanned and any points falling in the counted phase, which was usually ferrite or sigma, were recorded. Several fields were taken until the total points observed was 1000. The volume fraction of, say the ferrite phase (α) within a sample was given by:-

$$Vf_{\alpha} = \frac{P_{\alpha}}{P_t} \text{-----} (9)$$

Where

P_{α} = Point count in the ferrite phase

P_t = Total number of points observed

The accuracy of such determinations was dependent on the total number of points counted and the actual volume fraction of the phase. Two approaches can be made:- (1) If a pre-determined accuracy is required at a particular standard deviation a calculation can be made of the number of points in the counted phase (P_{α}) required to achieve the accuracy. This method relies on a first approximation being made of the volume fraction of the counted phase so as to determine the value of P_{α} . The count must then continue until the total number of points required is reached. (2) The total number of counts may be decided before hand, and the relative accuracy determined after the volume fraction has been calculated. Gladman et al⁽⁸⁶⁾ give the equation for determining the relative error as:-

$$\frac{\sigma_{Vf}}{Vf_{\alpha}} = \sqrt{\frac{1}{P_{\alpha}} (1-Vf)} \quad \text{-----} \quad (10)$$

where σ_{Vf} is the standard deviation.

One standard deviation gives the result to a confidence limit of 67% and two standard deviations, i.e. $2\sigma_{Vf}$, to a confidence limit of 95%.

This analysis gives a measure of the statistical errors involved in point counting but other practical inaccuracies exist and are listed in the monograph by Pickering⁽⁸⁵⁾. Generally the error determined by statistical analysis can be regarded as a minimum but it may be larger depending on such things as the resolution of the microscope, the etching procedure and morphology and fineness of the microstructure. In all cases for this

particular work the total count was 1000 points; accordingly the accuracy will depend on the actual volume fraction of the second phase. Volume fractions were in the order of 0.02 to 0.4 giving a value for $2\sigma V_f$ as 0.010 and 0.031 respectively. The larger figure can be represented as $\pm 3.1\%$ error, this value being adopted as the statistical error for all volume fraction determinations.

3.7 Magnetic Measurements

The use of a ferritescope, which essentially measures the amount of ferro-magnetic phase present, has been useful in determining the alloy constitution. The presence of ferrite was detected since it is the only equilibrium phase that is ferro-magnetic. The technique is very simple provided that the specimen is thick enough, ~ 3 mm. A probe is brought into contact with the specimen which produces a magnetic field and detects any ferro-magnetic phase within the sample, the wt% magnetic phase being read directly from the instrument.

The instrument was particularly useful in investigating two and three phase structures where either ferrite or sigma could occur, and at equilibration temperatures around 900°C where the upper temperature for sigma-formation was reached.

3.8 Kinetics and Phase Transformations

A study of the kinetics of the transformations occurring at lower temperatures was carried out using the quantitative metallographic methods already described. A homogenisation temperature of 1150°C for 24 hours was used, the specimens being sealed in tubes under argon. No prior cold working was carried out so that recovery and/or recrystallization could not play a part in the transformation mechanisms. Samples were

treated in air at 800°C for times from 5 minutes up to 200 hours. Quantitative analysis of the on-going transformations was carried out where this was possible. Quantitative microprobe analysis was also used to study the partitioning effects of the elements as transformation proceeded, in order to assess the approach to equilibrium.

3.9 Transmission Electron Microscopy

Extensive use of transmission electron microscopy has been made to examine the morphology of fine structures and to identify phases using selected area diffraction techniques. The instrument used was a JEOL 100 CX with a side entry deucentric uniaxial tilt stage. The operation of a transmission electron microscope is regarded as a standard technique and will not be reported in detail here.

Since considerable cold work had been used to facilitate the approach to equilibrium, a fine structure, particularly at the lower temperatures, was often obtained. Electron microscopy proved particularly useful for these structures and in the case of duplex or three phase material, orientation relationships and % mismatch factors have been determined. The development of a computerized technique for the solution of selected area diffraction patterns has been utilised and refined to facilitate phase identification. The method involves the measurement of five diffraction spots and a knowledge of the camera constant. The observed d spacings are then compared with programmed crystallographic data for the phases present in stainless steels, thus enabling the diffraction pattern to be indexed and the phase identified.

The T.E.M. has been used to study and measure the extent of void swelling using the High Voltage Electron Microscope (H.V.E.M.) and the Variable Energy Cyclotron (V.E.C.) to simulate neutron irradiation, an account of which is given in sections 3.11, 3.12.

3.10 Quantitative Microanalysis

A major part of the work has been the determination of the composition of the phases present and the partitioning effects of the various elements between the phases. For the majority of this work a Philips PSEM 500 Scanning Electron Microscope (S.E.M.) with an Energy Dispersive X-ray Analysis (E.D.A.X.) attachment has been used. For part of the work, where the composition makes the use of energy dispersive analysis inaccurate, a fully automated electron probe microanalyser has been used.

A specimen holder, Fig 11, has been designed that allows the X-ray analysis of both sample and standards simultaneously, which is important in quantitative microanalysis. Samples are mounted in a conducting medium which does not require the use of conducting glues (such as silver dag) which are likely to contaminate the specimen and require drying and out-gassing. The general configuration for microanalysis is shown in Fig 12. The take-off angle is important since it governs the path length that the X-rays must traverse through the sample and hence the degree of absorption. A take off angle which was as high as possible whilst being consistent with an optimum count rate was used, in this case 60° . The counter windows must be set at particular energy levels so as to collect the characteristic X-radiation from each individual element. It was also important

to set a background window as near as possible and to the left (ie lower) of the characteristic energy for each element. There must be no change in the electron beam energy whilst analysis is being carried out as this will affect the count rate and hence the accuracy of the results. As a consequence the voltage, current, electron beam spot size, focus and gain control must be pre-set before analysis was commenced and these must remain constant until the analysis was complete.

The area, phase or precipitate within the sample which is to be analysed, is selected and a convenient count time is chosen. The count time should be as long as practically possible, and is usually in the region of 40-100 seconds. Windows are set for all elements present in the alloy and the standards usually comprise the pure elements.

The X-ray intensity data is correlated with the apparent mass fraction of any element (k), eg. chromium, is given as a ratio of the intensity of chromium Xrays from the sample to those from the standard minus the background count in each case, ie:-

$$k_{Cr} = \frac{I_{Cr} \text{ Sample} - I_{Cr} \text{ Sample Background}}{I_{Cr} \text{ Standard} - I_{Cr} \text{ Standard Background}} \quad \text{----(11)}$$

For any system, assuming no corrections are necessary, then:-

$$k_A + k_B + \dots + k_n = \sum_{i=A}^n k_i = 1 \quad \text{----(12)}$$

Inevitably however $\sum_{i=A}^n k_i$ is less than unity because of the prevailing absorption, fluorescence and atomic number effects.

Having obtained the apparent mass fractions these must be corrected by :-

$$C_{Cr} = F \cdot k_{Cr} \quad \text{----(13)}$$

where C_{Cr} is the mass % of chromium (corrected) and F is a function of atomic number, absorption and fluorescence effects, known as the Z.A.F. correction coefficient.

(a) The Atomic Number Effect

Electrons entering the surface of a specimen both penetrate the specimen and are scattered by it. The effect of these two processes on X-ray emission can be considered more simply in terms of two factors. The electrons which are back scattered from the surface do not contribute to X-ray production, the fraction of the incident electrons which enter the specimen being termed R . Specimens of low atomic number have high values of R with the effect becoming insignificant for higher atomic number elements.

The electrons which penetrate the specimen may cause ionisation, producing X-rays or they may be scattered within it. The production of X-rays by ionisation depends on the critical ionisation potential of the specimen and thus on its composition. Elements of low atomic number have low critical ionisation potentials, are more easily ionised, and have greater stopping power per unit mass. The stopping power of the specimen, S , is higher for elements of lower atomic number. The initial energy of the electrons affect the values of R and S in that higher energy electrons are more readily back scattered and escape from the sample producing a lower value for R .

Thus both R and S vary with both initial electron energy and the atomic number, with the atomic number correction being

given as:-

$$C_Z = \frac{R}{S} \text{-----(14)}$$

C_Z is the proportion of the correction factor F, due to atomic number effects. These two factors R and S tend to cancel each other out as the atomic number and accelerating voltage vary, although they can, in certain systems, represent an important part of the correction procedure and are always included in correction programmes for bulk specimen analysis.

(b) The Absorption Effect

X rays travelling through a material of density ρ suffer absorption:-

$$\frac{I_t}{I_o} = e^{-\frac{\mu}{\rho} \cdot \rho x} \text{-----(15)}$$

where:-

I_t = the transmitted X-ray intensity
 I_o = the original X-ray intensity
 μ/ρ = the mass absorption coefficient
 x = distance travelled by X-rays

For a specimen composed of a number of elements the value for μ/ρ is given by the individual absorption co-efficients multiplied by their mass fractions. μ/ρ will also vary with the initial X-ray energy. X-rays are generated at different depths within a specimen and hence must travel through different distances to escape from the sample. They are thus absorbed to different degrees. The correction for this absorption, C_A , takes into account the shape and volume of specimen producing the X-rays, the angle at which the X-rays are collected from the specimen surface, the angle at which the incident electron beam enters the specimen surface, and the composition of the specimen.

(c) The Fluorescence Effect

The absorption of X-rays occurs when the X-rays give up their energy to ionise other atoms. Thus if an X-ray of element Z_1 has an emission energy which is slightly higher than the energy required to ionise element Z_2 , i.e. the critical excitation potential, the emitted X-ray is likely to be absorbed and X-rays characteristic of the element Z_2 will be produced. Thus if the element Z_2 happens to be in the process of being measured the intensity of its characteristic radiation will be increased and the apparent concentration therefore artificially increased. This degree of enhancement depends on the relative excitation probability, the fluorescence yield and the depth of electron penetration.

In addition, in specimens containing elements of high atomic number, X-ray fluorescence by the white or continuous radiation may occur and must be taken into account for bulk specimens. The correction for fluorescence is termed Cr.

Atomic number effects and atomic absorption are always present to some degree when analysing bulk specimens, whilst fluorescence effects can only occur at discrete conditions, i.e. when a characteristic X-ray of one element is sufficiently energetic to produce a characteristic X-ray of another assuming a collision takes place. Obviously in multi-component systems these corrections are complex and are invariably performed with the aid of a computer. The program used was the National Bureau of Standards FRAME 3, which has been modified to suit the data generated on a S.E.M. with a solid state energy dispersive analyser. The most serious disadvantage of the program is that

it is designed for an electron microprobe analyser which uses crystal spectrometers to measure the intensities of the X-rays and is wavelength dispersive. In the case of the electron microprobe analyser, the resolution of the crystal spectrometers was such that overlapping peaks of X-rays from different elements was rarely a problem. However in the case of the solid state detectors, where all X-rays of energies above 1000 eV are measured simultaneously, coupled with a resolution of the solid state detectors in the order of 150 eV, they commonly give rise to overlapping peaks. Such overlapping peaks of the X-ray intensities must be corrected for, and this is carried out by a process called peak stripping. A common example in stainless steels is chromium and manganese. The energy of the chromium $K\beta$ peak and the manganese $K\alpha$ peak are for all intents and purposes the same and if the concentration of the manganese is to be measured the intensity in the peak due to the chromium $K\beta$ must be "stripped" out. The calculations are usually part of the computer program, but essentially the intensity of the chromium $K\beta$ peak is calculated given a knowledge of the chromium $K\alpha$ and the ratio of intensities between chromium $K\alpha$ and $K\beta$ peaks. This ratio is in the order of 6 : 1 and is subsequently subtracted from the combined peak to give the true manganese intensity. It was found however that alloys containing only iron, chromium and nickel had no overlapping peaks of any significance and could be accurately corrected by using the FRAME 3 program. Fig 13 gives a comparison of results obtained on the S.E.M. at Sheffield City Polytechnic with the results for the same samples obtained on an S.E.M. at the Steetley company which was equipped with fully automatic computerized quantitative microanalysis, including

"peak stripping", which gives very good correlation of results. Microanalysis carried out on alloys with a fourth element addition was carried out on an electron microprobe analyser using wavelength dispersive crystal spectrometers and giving accurate results without the need for peak stripping.

3.11 Simulation of Neutron Irradiation using a High Voltage Electron Microscope.

The use of electrons to create radiation damage in metal was achieved conveniently in the high voltage electron microscope (H.V.E.M.) operating at 1MeV. For this purpose the A.E.I.E.M. 7 based at Harwell was used. A thin foil of the material under investigation was made by conventional techniques. Tilting the specimen is a pre-requisite and a single tilt non-eucentric tilt stage was used. Integral with the stage was a small molybdenum wound furnace that heated the sample "in situ". The size and concentration of voids created is a function of the temperature, and 500°C was adopted as a standard temperature which gave a sufficiently high void swelling rate consistent with the required void concentration, since too high a concentration of voids resulted in damaged regions which had a high concentration of small voids that overlapped and created further analysis difficulties at the measuring stage. The foil surfaces act as sinks for the Frenkel defects, resulting in a void free layer both at the top and bottom of the foil. Care has to be taken in the choice of foil thickness such that the void free layer is less than one third of the inter-void spacing.

The dose rate was also important and the following beam conditioning were used before the specimen was inserted. With

the screen horizontal the beam was switched on at 1MeV after conditioning at 1.1 MeV. The magnification to be used was then selected, in this case 17.3K for all the tests. The bias and condenser 1 were set to initial conditions of 1 and 8 respectively and the beam focussed, checking that the filament was saturated. The beam current was recorded continuously and the accelerator, Xs and Yx shifts were adjusted to give maximum current which is then the total beam current with no aperture inserted. The total beam current can be adjusted by changing condenser 1 to lower values to increase the current, and visa-versa. The centre beam current was recorded by inserting the 80 μm diffraction aperture and adjusting the bright field X and Y tilts until a maximum reading was achieved. Removing the aperture and tilting the screen to the normal operating position will give I_0 , the current reading with tilted screen and no sample. The sample was then inserted, an appropriate phase was chosen and the thickness selected according to experience. The current I was again recorded with the beam passing through the foil and a measure of the foil thickness at that point was given by:-

$$\text{Foil thickness, } t = f(I/I_0) \text{ -----(16)}$$

This value will depend on the material being examined but experience has shown that a value for I/I_0 for stainless steels of the order of 0.08 to 0.01 will give reasonable results. The instrument had been previously calibrated, and it is the centre beam current that is related to the dose rate since it is the volume impinged upon by the centre of the beam that is of interest.

The centre beam current, which was usually in the order of $13-16 \times 10^{-9}$ amps, is multiplied by a factor of .036 which is determined by a calibration of the instrument, and gives the dose rate in d.p.a. min^{-1} . The total beam current, usually in the order of $3.5-4.5 \times 10^{-7}$ amps, was adjusted to give a dose rate of approximately $0.5 \text{ d.p.a. min}^{-1}$. The use of an objective aperture, provided it is sufficiently large, does not interfere with the calibration procedure.

The specimen was then scanned and tilted until an area was found that was of the required thickness and had the dislocation network tilted to extinction, since it is difficult to analyse micrographs that are complicated by dislocation networks. Once the appropriate area was found the beam was switched off and the foil heated to an indicated temperature 20°C below that at which the test was to be carried out; previous workers have identified that the local heating of the foil by the influence of the electron beam is approximately 20°C . The heating stage is powered by lead acid batteries and controlled by voltage regulation, and a thermocouple inserted in the stage records the temperature and is read directly from a digital meter. When the required temperature had been reached, the beam was switched on and the specimen re-aligned. The specimen moves considerably on heating. Once aligned and the image focussed, the beam was focussed and the timer started. The procedure was to observe the foil in the focussed beam until voids began to appear when the test was then stopped by defocussing the beam and recording the image and time elapsed. It has been established

that whilst the beam is defocussed negligible irradiation damage is occurring. The process was continued with micrographs being taken at convenient time intervals up to the dose rate required. Once the voids have been established, at some convenient point the foil is tilted to another zone where again the dislocations are extinguished and the image is again recorded. This now provides a stereographic pair of images and with a knowledge of the angle between the micrographs the void layer thickness can be determined. Eventually a series of micrographs are produced that represent the void growth up to a given dose rate.

The micrographs were then printed at times 5 enlargement to enable the void swelling characteristics of an alloy to be analysed. The voided layer thickness was determined using a stereographic viewing table equipped to measure the lateral distance change caused by the angle between the stereographic pairs.

The resulting magnification was 86.5K, and a circle of D = 6cm was constructed to enclose a volume:-

$$\text{Volume } (V) = \frac{\pi \cdot D^2}{4 \times \text{magnification}} \times \text{voided layer thickness} \quad \text{--- (17)}$$

$$\text{The mean void diameter :- } d_v = \frac{1}{N_v} \sum_{i=1}^{N_v} (d_i^3)^{\frac{1}{3}} \quad \text{----- (18)}$$

where N_v is the number of voids measured, their shape being assumed to be a sphere of diameter d , which was taken to be the average lateral dimension for any particular void. At least 100 voids are measured for statistical accuracy. The total number of voids within the analysed volume are counted and recorded. From this

information the mean void size (\bar{d}_v), void number density ($N_v \cdot \text{cm}^{-3}$) and % void swelling ($\frac{\Delta V}{V}$) can be calculated for a series of doses leading to the relationship between void swelling and dose. All the samples tested were duplex austenite + ferrite alloys, only the austenite being irradiated since the oxidation of the ferrite was significant at quite short times which made the imaging of voids (if any) impossible.

3.12 Simulation of Neutron Irradiation using a Variable Energy Cyclotron (V.E.C)

The essential difference in technique between H.V.E.M. irradiation and V.E.C. irradiation was that the samples are irradiated before the thin foils are prepared. Specimens can only be irradiated to one dose level at any one irradiation although up to 12 specimens can be irradiated simultaneously.

Up to twelve three millimeter discs, $\sim 150 \mu\text{m}$ thick are made into a target by electro-plating a copper substrate around the discs. The upper surface is then polished to a mirror finish using a vibratory polisher and a slurry of $.025 \mu\text{m}$ Al_2O_3 . The target is mounted in the V.E.C. and, in this case, implanted with 10 atomic p.p.m helium at room temperature prior to testing to simulate the helium that is created as a result of transmutation reactions occurring as a result of neutron irradiation. It would be closer to neutron irradiation if the helium implantation occurred simultaneously with the irradiation but practical limitations make this very difficult. The target is then irradiated to a dose of 40 d.p.a. at 600°C , since it is known that void swelling will occur most favourably under these conditions. Due to practical machine limitations the irradiations

is then intermittent and the dose was built up with a series of irradiations taking approximately 20 hrs for 40 d.p.a. A consequence of this is that the temperature will cycle between ambient and 600°C several times and this must be taken into account when examining the resultant microstructures. The irradiation used for these experiments was 46 MeV Ni⁶⁺ ions and irradiation damage can be considered to occur at a distance into the disc equal to the average path length of the ions. In the case of 46 MeV Ni⁶⁺ ions it is in the order of 3 μm from the surface. The ions are monochromatic and produce a virtual monolayer of damage within the discs which is very difficult to locate by known techniques. Consequently the target is continuously tilted around its axis so as to increase the damage layer thickness. Nevertheless a damage layer that is between 2.5-3.5 μm below the surface requires an exacting technique to detect it.

Transmission electron microscopy was used to study the void swelling characteristics of the alloys under investigation. The method used to locate the damaged layer was by the use of a microhardness indentation and a knowledge of the relationship between a reduction in the length of the diagonal of the microhardness indentation and the reduction in thickness of the disc. The irradiated discs were cleaned, although generally there was a corrosion layer on the surface which was hard and difficult to remove. The discs were vibratory polished using 0.025 μm Al₂O₃ as the slurry until the metallic surface was just clear in the centre of the disc. A microhardness mark was then made in the

centre with another one near the edge such that the disc could be aligned so that it was always the same diagonal that was being measured. An initial reading was taken, the reduction in thickness of $3\mu\text{m}$ was equivalent to a reduction in indentation diagonal length of $21\mu\text{m}$ because the ratio was 7:1. In practice the value used is $19\mu\text{m}$ to allow for a flash electropolish of the damaged layer. With this stage complete the vibratory polished and electro-polished surface, which hopefully was the damaged layer, was stopped off with lacomit. The reverse side of the disc was then dished electrolytically using a suitable solution, in this case 10% perchloric acid in methanol and glycerol at room temperature, until $25\mu\text{m}$ of material remained. The final perforation was carried out manually at -40°C using 10% perchloric acid in methanol.

Transmission electron microscopy was then used to study the void swelling behaviour of the specimens. Micrographs were taken of the damaged region to determine the void swelling characteristics, and a stereographic pair was again used to calculate the thickness of the foil. Since the discs under irradiation will have been at 600°C for up to 15 hours it was likely that, in these particular alloys, microstructural changes will have occurred and these aspects are also investigated using electron microscopical and diffraction techniques.

4 Results

4.1.1 Metallography of Fe-Cr-Ni Experimental Alloys

The establishment of the constitution of the iron-chromium-nickel system required a knowledge of the microstructures of the experimental alloys. Particular alloys were chosen, examples of which are given in Figs 14-16. The figures show the equilibrated microstructures at the seven chosen temperatures, ranging from 1150-650°C. At 1150°C (the homogenisation temperature) the microstructures of the samples used were generally duplex (austenite + delta ferrite), the exceptions being 3A (18Cr-2Ni) which contained 100% delta ferrite and 1D (20Cr-23Ni), 1H (30Cr-33Ni) and 3C (18Cr-10Ni) being 100% austenite. The general form of the duplex microstructure is given in Fig 14, alloy 1B (27Cr-16Ni) indicated the (austenite + delta ferrite) region above 950°C, subscripted (a), (b), and (c) and the austenite-sigma region below 950°C subscripted (d),(e),(f),(g). The lower the temperature the finer was the microstructure with the large delta ferrite grains having transformed to sigma and new austenite together with a fine precipitate evident within the austenite phase. Transmission electron microscopy was used to investigate the finer precipitates which are shown for alloy 1B(27Cr-18Ni) at 800°C and 650°C respectively in Figs 17 and 18. Selected area electron diffraction (S.A.E.D.) was used to identify the large grains as being sigma phase whilst the finer precipitate within the austenite was delta ferrite. The fine precipitate is clearly shown in Fig. 18(a) and would appear to be randomly distributed within the austenite grains.

The microstructure of alloy 3A (18Cr-2Ni) is shown in Fig.15. At 1150°C the structure was completely ferritic but precipitated

significant amounts of austenite at 1050°C and below. The volume fraction of austenite decreased below 800°C, which could indicate either a slowing down of the approach to equilibrium or a shift towards higher nickel contents of the austenite - (austenite + delta ferrite) phase boundary. It was also clear that the precipitated austenite had not transformed to martensite on subsequent quenching to room temperature.

Alloy 3B(18Cr-7Ni), Fig 16, was predominantly austenite at 1150°C and only precipitated significant amounts of delta ferrite at 800°C and below. It is evident though that Figs 16, (f) and (g) show three phases and that alloy 3B(18Cr-7Ni) lies within the ($\gamma + \delta + \sigma$) three phase field.

Fig. 19 shows the equilibrated microstructures of alloy 1F(35Cr-28Ni) at 900°C and below. The microstructures above 900°C is essentially the same as that for alloy 1B(27Cr-16Ni). Isothermal treatment at 900°C produced a lamellar type of precipitate within the delta ferrite grains which increased in amount at 800°C. At 700°C the lamellar agglomerate was finer and laths of a phase identified as delta ferrite were seen within the austenite matrix. At 650°C the lamellar type structure was unresolvable by optical microscopy and many laths were seen to precipitate across the whole of the austenite grains.

The electron micrographs in Figs 20 indicated the nature of the cellular type structure of austenite + delta ferrite that had an orientation relationship that was due to Kurdjumov-Sachs and is shown in the stereographic projection, Fig 21. Fig 22 shows the microstructure of alloys 4A(45Cr-17Ni) and 4B(32Cr-5Ni) which

were designed to fall within the three phase fields that lie at either side of the (austenite + sigma) phase field in the Fe-Cr-Ni ternary system. Three temperatures were chosen for examination, namely 900°C, 800°C and 650°C respectively. Alloy 4A (45Cr-17Ni) clearly fell within the three phase field showing primarily ferrite (dark), austenite (white) and sigma, the sigma being the phase within the austenite. The microstructures at 800°C and 650°C comprised of austenite grains with small precipitates of sigma within them, and an aggregate structure that was comprised of austenite and delta ferrite. The analysis of alloy 4B (32Cr-4Ni) indicated a nickel content that was quite low and only the heat treatment at 650°C produced a three phase structure.

4.1.2 Microprobe Analysis

The major technique used for the construction of the ternary equilibrium diagrams was the determination of the composition of the individual phases by a SEM+EDAX technique. The compositions of the phases in a two phase structure will lie at the ends of a tie line and will define the position of the phase boundary, whereas in the case of a three phase structure the compositions will lie at the corners of the three phase triangle. This technique allows the use of relatively few samples for constructing the ternary equilibrium diagrams. At temperatures of 900°C and below the approach to equilibrium was recognised to be very slow. If equilibrium has been obtained then the concentrations of the individual elements will be constant throughout a particular phase. Fig 23 shows an elemental line scan, using the S.E.M.

with Xray analysis facilities for the elements iron, chromium and nickel, across an austenite grain in a two phase ($\gamma + \alpha$) microstructure. Even allowing for experimental error this confirms the attainment of equilibrium. Further evidence for this was provided by the micro-analysis results obtained in the transformation studies on alloy 3A (18Cr-2Ni), and shown in Fig 24, which indicate that no further change in the composition of the individual phases had occurred after 20hrs at 800°C. It can also be seen from Fig 24 that constitutional, i.e. phase proportion, equilibrium had not been reached after 20 hrs.

The compositions of the individual phases for the alloys examined are given in Table 5, and represent the compositions at the phase field boundaries. The major problem with this technique was that in the case of micro-analysis of bulk specimens there was a limit to the size of precipitate or second phase particle that could be analysed. The electron beam diameter is usually the limiting factor being of the order of 5 μ m. This was not however the only limiting factor since X-rays are generated within the well known pear-shaped excited volume which effectively increased the beam diameter. Electron penetration is a function of the average atomic number of the specimen and the accelerating potential, which in itself will be a function of the (elemental Xray) critical excitation potential. It became clear that cold working and isothermally treating at the lower temperatures of 700°C and below produced a very fine structure which rendered micro-analysis somewhat innacurate. It is obvious

that the use of scanning transmission electron microscopy with an analytical Xray attachment (electron beam diameters in the order of 100Å) would be a major advantage for this type of analysis.

4.1.3 The Isothermal Sections of the Ternary Constitutional Diagrams.

The isothermal sections of the iron-chromium-nickel ternary system are shown in Figs. 25-30. At 950°C and above these sections were simple to construct with the relatively large grain sizes exhibited by the phases in the specimens. Below 950°C however the diagrams became more complex and this, coupled with the fineness of the structure, resulted in some scatter in the results particularly at 650°C. An analysis of variance was used to obtain:

$$\frac{\Delta K}{K} = \pm \left[\frac{(I_A + B_A)}{(I_A - B_A)^2} + \frac{(I_S + B_S)}{(I_S - B_S)^2} \right]^{\frac{1}{2}} \text{-----(19)}$$

where I_A = Xray intensity of element A in the sample
 B_A = " " " the background at an energy near A
 I_S = " " " a standard of pure element A
 B_S = " " " the background at an energy near A

$\frac{\Delta K}{K}$ is the fractional relative error in K, where K is the uncorrected mass fraction of element A due entirely to the statistical errors in counting the characteristic X rays. It was usual to find a value of $\frac{\Delta K}{K} = \pm 1\%$ of the actual value of the composition for the conditions used. However many other aspects of microanalysis cause errors and have already been discussed in section 3. Thus it was decided that the data generally had a relative error of about $\pm 2\%$ of the actual alloy content of a phase, particularly at

the lower temperatures of 700°C and below. When the choice was between two values for a fixed point such as the austenite composition of a 3 phase field, e.g. for alloys 3B (18Cr-7Ni) and 4B (32Cr-4Ni) which both gave this composition, the analysis for the point was used for the alloy containing the greater amount of austenite since the specimen would contain austenite grains of greater size and therefore better accuracy in determining the result. In this case alloy 3B (18Cr-7Ni) was predominately austenite whilst alloy 4B (32Cr-4Ni) contained only a small fraction of austenite; accordingly alloy 3B (32Cr-7Ni) was used.

Where the results of a particular analysis appeared to be inaccurate by comparison with the bulk of the data they were repeated using an electron probe microanalyser (EPMA). This technique has the advantage of an infinite choice of accelerating voltage, a smaller beam size $\sim 1\mu\text{m}$ and automation for the microanalysis procedure. The results are shown as triangles on the isothermal sections. The tie lines (shown as dashed lines for the two phase regions) are those that were experimentally determined.

For several of the fixed points of the isothermal sections, i.e. the triple points at the corners of the three phase fields, no data has been generated directly in this work. In these cases the positions of these points were estimated from a general consideration of the experimental data and the published information of Raynor and Rivlin⁽⁹⁾. These points are

indicated by the open circles as opposed to the closed points.

4.2 Transformations in Fe-Cr-Ni Stainless Steels

4.2.1. Introduction

Because of the importance of equilibria to the constitutional studies, specimens were only examined in their initial and final states. It was however believed to be necessary to study the transformations that were occurring because of the necessity to check that equilibrium had indeed been reached and also to detect whether any transient or intermediate non-equilibrium phases had been formed during the approach to equilibrium. Two compositions were chosen to study (i); the precipitation of austenite from ferrite, alloy 3A (18Cr, 2Ni) and (ii); the precipitation of sigma phase from a duplex (austenite + ferrite) structure, i.e. alloy 1A (30Cr, 13Ni). The temperature chosen for all the transformation work was 800°C.

4.2.2 Transformations in Alloy 3A (18Cr-2Ni)

Homogenisation at 1150°C (24hr, WQ) produced a single phase structure of ferrite, Fig. 31(a). The black dots present in the micrograph were etch pits produced as a consequence of the prolonged etching needed to reveal the ferrite grain boundaries; as already mentioned the etching of ferrite/ferrite grain boundaries was very slow with 10% oxalic acid. After aging for 10 minutes at 800°C a very fine precipitate was seen on the grain boundaries, Fig. 31(b). Transmission electron microscopy was employed to determine the nature of this phase which was identified by selected area electron diffraction as Cr_{23}C_6 and is shown in Fig. 32. Fig. 31(c) shows the microstructure after

aging for 1hr, the Cr_{23}C_6 particles having developed and another phase, identified as austenite, was beginning to precipitate at the grain boundaries together with the Cr_{23}C_6 . After aging for 20hrs, Fig 31(d), the precipitation of austenite as laths within the ferrite grains was clearly observed together with a cellular growth of austenite and Cr_{23}C_6 . After aging for 97hrs, Fig 31(e), the austenite laths had clearly developed into an agglomerate occurring throughout the ferrite grains, with no observable change in the Cr_{23}C_6 . Fig 31(f), shows the microstructure after aging 200hrs; it would appear that the austenite was starting to coalesce and spheroidise as the equilibrium structure was approached. The Cr_{23}C_6 tended to redissolve, presumably the carbon partitioning to the austenite and the chromium to the ferrite. Fig 15(e) shows alloy 3A (18Cr-2Ni) after aging for 700 hrs, and it must be emphasised that this specimen was sealed in silica under argon. Nevertheless the microstructure forms a logical extension of the transformation series. The austenite laths were clearly becoming more equiaxed and the Cr_{23}C_6 appeared to have been completely redissolved.

4.2.3 Transformations in Alloy 1A (30Cr-13Ni)

Figs 33 (a-f) shows the microstructure of alloy 1A(30Cr-13Ni) after aging at 800°C for up to 120hrs. The solution-treated (1150°C) microstructure shown in Fig. 33(a) was duplex (austenite + delta ferrite), the delta ferrite being the slightly darker phase. After aging for 10 minutes, precipitation at the austenite/delta ferrite grain boundaries had clearly commenced, Fig. 33(b).

Transmission electron microscopy confirmed the grain boundary precipitate to be a mixture of sigma and Cr_{23}C_6 . Bright and dark field illumination was used to identify the various phases, coupled with selected area electron diffraction. The plates shown in Fig 34 are examples of the morphologies of the precipitating phases and the diffraction patterns from which the structures were determined. Also it was observed that the precipitates were growing into the delta ferrite phase, thus confirming the optical microstructural observations. After aging for 30 minutes, Fig. 33(c), the sigma phase was consuming the delta ferrite by growing inwards from the boundaries and forming an envelope of sigma phase around the transforming delta ferrite grains. It was also evident that as the transformation proceeded this type of reaction was followed by a cellular reaction that consumed the remaining delta ferrite. Fig. 33(d), shows the cellular structure more clearly and transmission electron microscopy has identified the duplex cellular region as (austenite + sigma).

The two phase region is shown in Fig. 35(a), with the diffraction pattern, whilst Fig 35(b), shows a similar region with as yet untransformed delta ferrite characterised by the heavy dislocation density. Figs, 33(e),(f), show the general microstructure after aging for 70 and 120hours at 800°C and showed a general spheroidisation of the microstructure as equilibrium was approached. The presence of delta ferrite is shown in the transmission electron micrograph, Fig. 36(b), as the phase containing a high dislocation density in the specimen aged for the longest time of 120hrs. This suggested that equilibrium had not been reached. Fig. 36(a) is

a bright field electron micrograph of a sigma particle that has a semi-coherent interface, with the interface misfit being taken up by dislocations.

4.2.4. Quantitative Metallography and Microanalysis

The type of transformation occurring in alloy 3A (18Cr-2Ni) ie $\alpha \rightarrow (\alpha + \gamma)$, lends itself to quantitative analysis in terms of both metallography and microanalysis. The volume fraction of the austenite phase was determined by the standard point counting method described in section (3.5), the results of which were plotted against aging time in Fig. 24(b). It can be seen that no further transformation took place after aging for 160 hrs. Selected samples were chosen for microanalysis, again by the SEM-EDAX technique described in Section 3.6, such that the composition of the transforming austenite could be determined as aging progressed. The Wt%Ni of the austenite is shown as a function of aging time in Fig. 24(a) and provides a direct comparison between the change in volume fraction and nickel content of the precipitating austenite phase.

4.3. Effects of Fourth Element Additions on the Constitution of Fe-Cr-Ni Alloys

Using the base compositions of several selected ternary alloys, a fourth element was added to determine its effect on the constitution and to study further the concept of nickel and chromium equivalents based on alloys that are more relevant to reactor core components, such as stainless steels and iron based superalloys used for wrappers and cladding in the fast reactor. Eight such elements were chosen, four of which were well known austenite formers:- manganese, copper, carbon and nitrogen and four ferrite and/or sigma formers:- silicon,

molybdenum, titanium and niobium. All of these occur in commercial stainless steels and iron based superalloys. Two temperatures were chosen to encompass the (austenite + ferrite) region and the (austenite + ferrite + sigma) region, being 1050°C and 800°C respectively. The percentage of the fourth element addition, the temperature and the volume fraction of the ferrite and/or sigma phase are given Table 6.

4.3.1. Quantitative Metallography and Structural Changes

4.3.1.1. Addition of Austenite Forming Elements (Mn,Cu,C and N)

(a) 1050°C

The optical microstructures for the four austenite forming elements are shown in Figs. 37-40. At 1050°C the general effects of adding the austenite forming element was to reduce the volume fraction of the delta ferrite, with the exception of copper. Increasing the copper addition first gave a decrease in the volume fraction of delta ferrite at 1wt%Cu followed by an increase in the delta ferrite content as the amount of copper increased. This was then followed by a decrease in the delta ferrite content at the highest copper content.

A further complication was introduced by the formation of large particles of a chromium carbide in the alloy containing carbon, the carbide being identified as massive Cr_{23}C_6 by selected area diffraction. In the case of the nitrogen bearing alloys, no nitrides were observed in the optical microstructures, there simply being a decrease in the amount of delta ferrite.

(b) 800°C

At 800°C, initially the effect of manganese was to increase the tendency towards the cellular structure typified in Figs 41 and 20. This has been shown to be austenite and delta ferrite

having an orientation relationship near Kurdjumov-Sachs as shown in the stereographic projection, Fig. 21. At higher concentrations of manganese a third phase was observed, which was identified as sigma phase and is clearly shown in the optical micrograph, Fig. 41(c).

At 800°C the effect of copper showed a similar effect to that observed at 1050°C, culminating in a very fine structure at 7wt%Cu, Fig. 42(c).

In the case of the carbon series, the effect was again similar to that observed at 1050°C, except that the structure was finer and showed an increased volume fraction of $Cr_{23}C_6$, Fig. 43.

At 800°C the effect of nitrogen was to decrease the volume fraction of delta ferrite, no nitrides were observed at this temperature.

4.3.1.2 Addition of Ferrite Forming Elements (Si, Mo, Nb and Ti)

(a) 1050°C

The base alloys chosen for the addition of the ferrite forming elements were within the (austenite + sigma) phase field at the lower temperature; these were alloy 1A (30Cr-13Ni) for silicon, alloy 1B (27Cr-16Ni) for molybdenum, alloy 1C (25Cr-18Ni) for niobium and alloys 1B and 1C for the titanium additions. At 1050°C silicon had a very large effect in producing delta ferrite, and increased the volume fraction from 0.46 to 0.75 with the addition of 3.75wt%Si Fig. 44.

With regard to the effect of molybdenum, Fig. 45, the first 1wt% of molybdenum had no effect on the constitution and this is thought to be due to the carbon removing the molybdenum from solution as a carbide. Fig. 46 shows a transmission electron

micrograph of alloy 1B(27Cr-16Ni) to which 1wt%Mo has been added which after equilibration at 1050°C showed a phase identified as M_6C . Further additions of molybdenum had the effect of increasing the delta ferrite content, but this effect did not continue progressively as the molybdenum content was increased.

Additions of niobium initially showed an increase in the delta ferrite content, Fig. 47. With an addition of 2wt%Nb a phase appeared which was identified as Fe_2Nb by selected area electron diffraction, Fig. 48.

The effect of the titanium addition is shown in Fig. 49. There was a general increase in delta ferrite with increasing titanium addition. Again the presence of TiC was confirmed by transmission electron microscopy, the TiC occurring as large random precipitates Fig. 50.

(b) 800°C

At 800°C the effect of silicon was to increase the amount of sigma phase and to refine the overall structure, Fig. 51. Morphologies of this type render it particularly difficult to carry out accurate quantitative metallography. Hence the results are less reliable than those achieved at 1050°C, but nevertheless, generally agree with the overall effect which would be expected.

The microstructure of the alloys containing molybdenum are shown in Fig. 52. There was a general increase in the amount of sigma phase as the molybdenum content increased, and there was a tendency to produce much more clearly defined areas of sigma as typified by Fig. 52(c).

The niobium containing alloys showed an increase in the

amount of sigma phase as the niobium content increased, but there was no evidence of Fe_2Nb in the microstructure of the 2wt%Nb alloy at 800°C , Fig. 53.

Additions of up to 1wt%Ti again showed little change in the constitution, which was consistent with carbide formation removing the titanium from solution. Significant changes in the volume fraction of delta ferrite were observed with further titanium additions, Fig. 54.

The effects of the various austenite and sigma/ferrite forming elements are summarised graphically in Figs 55-58..

4.3.2. Nickel and Chromium Equivalents

The conversion of the experimental data into nickel and chromium equivalents is of commercial importance, particularly in terms of alloy design and structural stability studies. The method used compares directly the effect of nickel and chromium on the constitution of the ternary system with that of the fourth element additions.

4.3.2.1. Nickel and Chromium Effects on the Constitution

The nickel and chromium effects have been derived directly from the experimentally determined isothermal sections of the ternary equilibrium diagram. Fig. 59 is an isothermal section of the ternary diagram at a temperature above 900°C showing an alloy of composition C, lying in a two phase field of (austenite + delta ferrite). From the lever rule, AC and CD are proportional to the relative amounts (mass) of austenite and delta ferrite respectively. The line lengths can be either measured, or calculated as below, to determine the mass fractions of austenite and delta ferrite. Calculation can be accomplished using the

cosine rule and a knowledge of the wt%Ni and wt%Cr of the alloy

from Fig 59 :-

$$AD^2 = AB^2 + BD^2 - 2(AB \cdot BD) \cos B, \text{ (Cosine rule) } \text{-----} (20)$$

In this case $\hat{B} = 60^\circ$ and $\cos 60^\circ = \frac{1}{2}$ (Fig 59)

Then equation 20 will reduce to:-

$$AD^2 = AB^2 + BD^2 - (AB \cdot BD) \text{-----} (21)$$

Now AB is $\propto (\%Cr_A - \%Cr_D)$

BD is $\propto (\%Ni_D - \%Ni_B)$

Thus the equation can be written:-

$$AD^2 = (\%Cr_A - \%Cr_D)^2 + (\%Ni_D - \%Ni_B)^2 - (\%Cr_A - \%Cr_D)(\%Ni_D - \%Ni_B) \text{---} (22)$$

Now $\%Cr_A$, $\%Cr_D$, $\%Ni_D$ and $\%Ni_B$ can all be derived directly from the isothermal section.

The same method can be used to determine CD and the relative fractions of austenite and delta ferrite can be determined since

$$AC + CD = AD \text{ which is proportional to } 1 \text{-----} (23)$$

The mass fraction of austenite is give by $\frac{AC}{AD}$

and the mass fraction of delta ferrite is given by $\frac{CD}{AD}$

To determine the effect of nickel on the constitution the bulk composition is now changed by adding nickel along a line that keeps the ratio of chromium to iron constant. This is a straight line designated CN, which must run directly to the nickel rich corner of the diagram. A new bulk composition is now chosen C' and the above procedure repeated, thereby determining the decrease in the mass fraction of delta ferrite as a function of nickel content. The procedure is continued until the phase boundary is reached. The method can be used equally well for the effect of chromium. The results can be shown by a graph of nickel content versus the mass fraction of delta ferrite as shown in Fig. 60.

4.3.2.2. Nickel and Chromium Equivalents of the Fourth Element

Additions.

The actual volume fractions of delta ferrite or sigma in the alloys with fourth element additions have been determined by quantitative metallography, and are given in Table 6.

It is noted that the mass fraction of a particular phase within a sample is different from the volume fraction and will be related via the phase densities. If however the density of the phases are very similar then the correction that would be applied to the volume fractions to convert them to mass fractions would be minimal. It has been found in the literature⁽⁸⁷⁾ that the density of austenitic and two phase stainless steels are very similar.

An austenitic stainless steel of nominal composition (20wt% Cr-10wt%Ni) had a density of $7.74 \times 10^3 \text{ kg.m}^{-3}$ whilst a two phase stainless steel of nominal composition (29wt%Cr-0wt%Ni) had a density of $7.63 \times 10^3 \text{ kg.m}^{-3}$. The density of sigma phase given in reference (87) was $7.60 \times 10^3 \text{ kg.m}^{-3}$. Using these densities to correct the volume fractions to mass fractions an alloy having a volume fraction of 0.2 would have a mass fraction of 0.198 which is somewhat less than the error associated with the determination of the volume fraction by point counting.

Also, when the mass fractions were determined from the isothermal sections of the ternary equilibrium diagram for particular alloys they showed very good agreement with the measured volume fractions, thus indicating that the relative densities of the various phases were very similar. In view of this it was thought unnecessary to correct the volume fractions for

the determination of nickel and chromium equivalents.

Using the graphs as illustrated in Fig. 60, the relative effects of the fourth element additions as nickel and chromium equivalents can be determined. In Fig. 60 the line represented by A is the volume fraction of the delta ferrite phase of the base ternary alloy, ie with no fourth element addition. The change in volume fraction of the delta ferrite with the fourth element addition was then determined by the point counting method already described. In the case of the example the volume fraction of delta ferrite has decreased from 0.2 to 0.1.

The equivalent amount of nickel required to have the same effect on the constitution can then be read off, in this case 3.25wt%Ni. The nickel equivalent is determined by dividing the wt% Ni equivalent by the wt% of the fourth element addition. This process is repeated for all the alloys within the series, which were then plotted as a graph of fourth element additions against nickel equivalents. The same process is carried out for the ferrite forming elements to determine their chromium equivalents.

It can be seen that as the wt% of the fourth element increases the wt% of chromium and nickel will decrease. This may well cause difficulty in deciding what base composition of nickel or chromium to use when calculating the equivalents. Since the reduction in nickel and chromium will be reduced in the same proportion to each other their relative effects on the constitution will tend to cancel each other out. Therefore the base composition of the ternary alloy has been used for the determination of nickel and chromium equivalents.

The other element that needs consideration is carbon. In the case of the higher additions of carbon, significant amounts of $M_{23}C_6$ were precipitated. This was taken into account by measuring the volume fraction of $M_{23}C_6$ and calculating the mass % of carbon involved in its formation in the following manner:-

The volume fraction of carbide must be converted to a mass fraction of carbide.

$$\text{From Density} = \frac{\text{Mass}}{\text{Volume}} \text{-----(24)}$$

$$M_c = \rho_c \cdot V_c \text{-----(25)}$$

$$\text{and } M_m = \rho_m \cdot V_m \text{-----(26)}$$

where M_c is proportional to the mass fraction of carbide
 M_m is proportional to the mass fraction of matrix
 ρ_c and ρ_m are the densities of carbide and matrix phase
 V_c and V_m are the volumes of carbide and matrix phase respectively

But

$$V_{fc} = \frac{V_c}{(V_c + V_m)} = V_c \cdot \frac{1}{(V_c + V_m)} \text{-----(27)}$$

$$\therefore V_c = V_{fc} (V_c + V_m) \text{-----(28)}$$

$$\text{and } V_m = V_{fm} (V_c + V_m) \text{-----(29)}$$

\therefore equations (25) and (26) become

$$M_c = \rho_c \cdot V_{fc} \cdot (V_c + V_m) \text{-----(30)}$$

$$\text{and } M_m = \rho_m \cdot V_{fm} \cdot (V_c + V_m) \text{-----(31)}$$

$$\text{Now } M_{fc} = \frac{M_c}{(M_c + M_m)} \text{-----(32)}$$

where M_{fc} is the mass fraction of carbide.

Substituting for M_c and M_m from (30) and (31):-

$$M_{fc} = \frac{\rho_c \cdot V_{fc} \cdot (V_c + V_m)}{\rho_c \cdot V_{fc} \cdot (V_c + V_m) + \rho_m \cdot V_{fm} \cdot (V_c + V_m)} \quad \text{-----(33)}$$

$(V_c + V_m)$ will cancel and $V_{fm} = (1 - V_{fc})$

$$\therefore M_{fc} = \frac{\rho_c \cdot V_{fc}}{\rho_c \cdot V_{fc} + \rho_m (1 - V_{fc})} \quad \text{-----(34)}$$

which will transpose to

$$M_{fc} = \frac{\rho_c}{\rho_c + \frac{\rho_m}{V_{fc}} - \rho_m} \quad \text{-----(35)}$$

Dividing through by ρ_c gives:-

$$M_{fc} = \frac{1}{1 + \frac{\rho_m}{\rho_c} (1 - V_{fc})} \quad \text{-----(36)}$$

The mass fraction of carbide x 100 will give the mass % carbide from which the individual amounts of chromium, iron and carbon can be determined.

The mass fraction of each element within the $M_{23}C_6$ will depend upon the stoichiometry of the carbide.

The $M_{23}C_6$ was taken as $Cr_{21}Fe_2C_6$.

The mass fraction of carbon in $M_{23}C_6$ then will equal:-

$$M_{fc}(\text{in carbide}) = \frac{(6 \times \text{Atomic wt. C})}{(21 \times \text{Atomic wt Cr}) + (2 \times \text{Atomic wt Fe}) + (6 \times \text{Atomic wt C})} \quad \text{--(37)}$$

$$M_{fc} = \frac{(6 \times 12.011)}{(21 \times 52.00) + (2 \times 55.85) + (6 \times 12.011)} \quad \text{-----(38)}$$

$$M_{fc}(\text{in carbide}) = 0.056$$

The mass% carbon that is associated with the carbide will then be:-

$$\text{Mass \% C} = \text{Mass \% Carbide} \times M_{fc}(\text{in carbide}) \quad \text{-----(39)}$$

The mass % chromium and iron are determined in a similar manner.

Table 7 summarises the amount of carbon, iron and chromium combined as $M_{23}C_6$ in the carbon series alloys.

When considering the elements that are carbide formers, namely molybdenum, titanium and niobium it was necessary to take account of the amount of alloying elements that formed carbides and hence would be lost from the matrix. Transmission electron microscopy confirmed that random carbides were evident in all the alloys containing molybdenum, titanium and niobium at both 800°C and 1050°C.

The solubilities of carbon in the presence of titanium and niobium have been determined by Pickering et al⁽⁸⁸⁾ who obtained solubility equations of the form:-

$$\log [Ti][C] = \frac{-6780}{T^{\circ}K} + 2.97 \text{ -----(40)}$$

$$\log [Nb][C] = \frac{-9350}{T^{\circ}K} + 4.55 \text{ -----(41)}$$

The solubility of carbon at 800°C for the lowest addition of titanium of .25wt%, was 0.002wt%C, whilst at 1050°C the solubility rose to 0.013wt%C. At 1wt%Ti addition the solubilities at 800°C and 1050°C were 0.0002wt%C and 0.0024wt%C respectively. The solubility of carbon with a niobium addition of 0.5wt% was calculated as 0.0001wt%C at 800°C and 0.003wt%C at 1050°C. The corresponding solubilities for an addition of 2wt%Nb were ~ 0 and .0009wt%C at 800°C and 1050°C respectively. Unfortunately solubility data is not available for molybdenum which, since it forms a M₆C (or M₂₃C₆) type carbide, will have a relatively large mass of molybdenum associated with carbon if carbides are formed. If the carbide formed was Mo₆C then .005wt%C will have combined with 0.24wt%Mo max.

It must be noted that, (1) even in the 0.25wt%Ti alloy at 1050°C the presence of a MC type carbide was evident. Also (2) the solubility data was determined using base alloys of (18Cr-13Ni-0.1C), and (3) The exact stoichiometry of the carbides was not

known. The alloys used in this work had $\sim 10\text{wt}\%$ more chromium, the effect of which is not known, and also the alloys will be two phase which again may affect the solubility of carbon in these alloys.

Considering all these points the corrections made, due to carbide formation was only significant in terms of the chromium equivalents for the molybdenum additions.

It was also evident that molybdenum did not have any detectable affect on the constitution, up to the first $1\text{wt}\%$ of addition. In consideration of these points it was decided to determine the amount of fourth element addition that would be taken up as a carbide if all the carbon in the alloy formed a carbide, this value being subtracted from the bulk addition for the purpose of chromium equivalent determinations.

In the case of the niobium additions, at the higher niobium contents Fe_2Nb was identified. A significant volume fraction (0.03) of Fe_2Nb was present in the highest niobium content alloy. The density of the intermetallic phase was calculated as $10.05 \times 10^3 \text{ kg.m}^{-3}$ which represented $1\text{wt}\%\text{Nb}$ that was 'tied up' in the form of Fe_2Nb and was subsequently subtracted from the bulk $\text{wt}\%\text{Nb}$ for chromium equivalent determination. In general the effect of fourth element additions on the constitution is not linear, the graphs for nickel and chromium equivalents being given in Figs. 61-67.

4.3.3 Partitioning of Fourth Element Additions

In attempting to understand the reasons why various elements affect the constitution in particular ways a knowledge of the partitioning of an element between the various phases is valuable.

The partitioning of elements between phases has been determined

by a quantitative microanalysis using an X-ray wavelength spectrometer. This was necessary because of the overlapping of the energy peaks for the fourth element when using an energy dispersive system.

The results are given in the form of the composition of the phases and are summarised in Table 8.

4.3.4 Irradiation Damage

The void swelling behaviour of a number of the quaternary alloys has been examined using the High Voltage Electron Microscope (H.V.E.M.) irradiation and irradiation in a Variable Energy Cyclotron (V.E.C.). Both methods use an energetic source of charged particles to produce structural damage within the specimens which, at the temperature of interest for fast reactors, **generally** manifests itself as the nucleation and growth of voids. This is due to a higher supersaturation of vacancies than interstitials, which is a consequence of the preference of dislocations for interstitial point defects than for vacancies. These vacancies can then migrate to form clusters and coalesce to produce voids within the material.

4.3.4.1 H.V.E.M. Irradiation

The H.V.E.M. used electrons at 1 MeV, at a temperature of 500°C and a dose rate of approximately 0.5 d.p.a. per minute, to produce the damage. Alloys containing 1 and 4 wt% Si; 1, 3 and 8 wt% Mn; and 7.5 wt% Cu have been studied using the H.V.E.M. Fig. 68 shows a typical series of micrographs illustrating the increase in void size with increasing dose. There were three important parameters which were determined from the electron micrographs, namely:- (i) void number density (N_v), (ii) mean void volume (\bar{v})

and (iii) relative swelling $\frac{\Delta V}{V}$. These results were obtained in the following manner. The void number density was determined by counting the voids occurring within a specific volume. To do this the thickness of the void layer must be known and this is obtained from stereo-microscopy carried out on a stereographic pair of micrographs produced on the same test specimen. In the H.V.E.M. the specimens were in the form of thinned discs $\sim 4,000-5,000\text{\AA}$ in thickness and because of this both the bottom and top surface will act as sinks for interstitials and vacancies and hence produce a void free layer at the surface of the foil. The thickness measurement for the foil is taken between the top and bottom of the damage layer. The number of voids in a given volume was counted and is usually expressed in terms of the void number density, N_v . The mean void size is calculated by measuring the diameter of the voids. The actual shape is in the form of a tetrakaidecahedron but in practice a spherical shape is assumed. The mean void diameter (\bar{d}_v) is determined as:-

$$\bar{d}_v = \frac{1}{N} \cdot \sum_{i=1}^{N_v} (d_i^3)^{\frac{1}{3}} \quad \text{-----(42)}$$

where d is equal to the void diameters
and N is equal to the total number of voids measured.

The mean void volume (\bar{v}) is then equal to:-

$$\bar{v} = \frac{1}{6} \pi \cdot \bar{d}_v^3 \quad \text{-----(43)}$$

The total volume of voids within a volume V of void containing material is given by:-

$$V = V \cdot N_v \cdot \bar{v} \quad \text{-----(44)}$$

The relative void swelling is expressed as either:-

$$\frac{\Delta V}{V} \quad \text{or} \quad \frac{\Delta V}{(V-\Delta V)} \quad \text{-----(45)}$$

The relative percentage void swelling versus irradiation dose is given in Figs. 69 and 70 for the additions of silicon and manganese respectively. In addition to those alloys shown, tests were carried out on the 4%Si alloy and the 7.5%Cu alloy. In both cases no voids were detected up to the total dose of 30 d.p.a. The dislocation structure which also developed with irradiation is shown for the 7.5wt%Cu alloy in Fig. 71(a)

4.3.4.2 V.E.C. Irradiations

The V.E.C. uses positively charged particles to cause damage to the structure, and any one experiment was confined to the use of one specific dose. Irradiation was carried out using 46 MeVNi⁶⁺ ions, at a temperature of 600°C, to a total dose of 40 d.p.a. A typical electron micrograph illustrating V.E.C. induced void swelling, is shown in Fig. 72.

The V.E.C. was used to study alloys containing manganese, copper, silicon and molybdenum. The quantitative analysis was carried out in much the same way as that for the effects of H.V.E.M. irradiations except that due to a different preparation technique, (Section 3.12) there was no void free surface layer in the V.E.C. specimens. In fact the voids cut the foil surfaces and care had to be taken when deciding whether a void cut a free surface or was wholly within the foil. For counting purposes the voids which cut the foil surfaces were taken as $\frac{1}{2}$ voids. Otherwise the same procedure as outlined for H.V.E.M. irradiations was adopted.

The results of the V.E.C. irradiation are summarised as relative percentage void swelling against fourth element addition in Fig. 73.

The time taken to achieve a dose of 40 d.p.a. in the V.E.C. was \sim 20hrs and the effect of the combination of temperature and irradiation caused a considerable increase in the transformation rate of delta ferrite to (sigma + new austenite) in these alloys. The structure of the samples would be expected to undergo a transformation of the ferrite to (austenite + sigma) but 20 hrs at 600°C is insufficient to start the transformation under purely thermal conditions. It can be seen quite clearly in Fig. 74 that considerable transformation of the ferrite had occurred under V.E.C. irradiation and that the structure was that which would be expected to result from equilibration for much longer times, i.e. over 1000 hrs. It can also be seen that the newly formed austenite has begun to swell by the formation of voids. This behaviour was noted in all the alloys irradiated in the V.E.C.

5 Discussion

5.1 Constitution

5.1.1 Microstructure of the Fe-Cr-Ni Base Alloys

In general the equilibrated alloys exhibited similar microstructures, that were essentially dependent on the ageing temperature. Above 900°C the form of the isothermal sections of the ternary equilibrium diagram was relatively simple. Since at the higher temperatures recrystallization occurred, as shown by the equiaxed structure and the annealing twins within the austenite grains, the structures developed were easy to identify and interpret. A similar type of microstructure was observed over the whole range of alloys investigated, i.e. either single phase (austenite) or (ferrite), or duplex (austenite and ferrite), the duplex microstructure being shown clearly in Figs 14 (a, b and c). This type of structure was ideal for the determination of the phase compositions by quantitative micro-probe analysis.

At lower temperatures of 900°C and below the microstructures became more complex. The structure became finer and difficult to interpret. It was clear that complete recrystallisation did not occur, particularly in specimens aged at 700°C and 650°C. In the alloys that were within the (austenite + sigma phase) field at lower temperatures, the delta ferrite that was in equilibrium at the solution treatment temperature transformed to sigma phase and new austenite. This often resulted in a cellular structure that was very fine and presented difficulties for quantitative micro-probe analysis.

Series 1 (which is the constant 57wt%Fe with varying chromium

and nickel) of the base ternary alloys was designed to fall within the (austenite + sigma) phase field at lower temperatures below 900°C. Subsequent examination of alloy 1F(35Cr-28Ni) found no evidence of sigma phase even at 650°C, which must place the alloy in the (austenite + delta ferrite) phase field to the left of the (austenite + sigma phase) field. This represented a significant change in the phase boundaries at that alloy composition to those that had previously been reported by other workers⁽⁴⁾.

The transformation of the delta ferrite during aging below 900°C produced a cellular type growth of the austenite and delta ferrite that is shown in Fig 20 with the phases exhibiting the orientation relationship of Kurdjumov and Sachs. This was in agreement with the orientation relationship reported by Beckett⁽³⁹⁾.

In series 3(constant 18wt%Cr) of the base ternary alloys, it was found that alloy 3B(18Cr-7Ni) was within the three phase field of (austenite + delta ferrite + sigma phase) at 700°C and below. This again was unexpected from the previous published work⁽⁴⁾ but did give a valuable result since it established the austenite corner of the three phase field.

The two alloys in series 4,(45Cr-17Ni) and (32Cr-4Ni), were designed to fall within the three phase (austenite + ferrite + sigma phase) fields that lie to either side of the (austenite + sigma phase) field. These alloys, when it was possible to identify that three phases were present, provided information that established the corners of the three phase fields. Not always was it possible to analyse all three phases in any given alloy. Unfortunately the lower nickel alloy did not fall within

the three phase field, except at 650°C, because the aimed for nickel content was not precisely obtained.

The transformation of the ferrite occurring at 800°C was studied in some detail for alloys 1A(30Cr-13Ni) and 3A(18Cr-2Ni). Alloy 1A(30Cr-13Ni) was within the (austenite + sigma phase) field at 800°C, whilst alloy 3A(18Cr-2Ni) fell within the (austenite + alpha ferrite) phase field. The alloys were solution treated at 1150°C to equilibrate the structures prior to aging.

In the case of alloy 1A(30Cr-13Ni) the resultant microstructure was two phase (austenite + delta ferrite). Upon aging the delta ferrite decomposed to a cellular structure of austenite + sigma phase. The sigma phase initially nucleated at the austenite-delta ferrite grain boundaries, and eventually formed an envelope of sigma around the delta ferrite grain, Fig 33(c). The remaining ferrite then transformed to the familiar cellular structure of (austenite + sigma phase) and consumed the remainder of the delta ferrite, Fig 33(d). This was due to the sigma phase decreasing the chromium content of the delta ferrite to such a level that further formation of sigma phase was not possible unless accompanied by the formation of new austenite which itself was depleted in chromium. The composition of this remnant delta ferrite therefore was such that it transformed to equilibrium (austenite and sigma phase). The phases eventually coalesced to form a microstructure of primary austenite and a dispersion of new austenite and sigma phase.

For alloy 3A(18Cr-2Ni) the 1150°C solution treatment resulted in a microstructure that was single phase ferrite. Upon aging for

10 minutes at 800°C this alloy precipitated $M_{23}C_6$ on the grain boundaries. After 1 hour aging a further phase, identified as austenite, nucleated at the ferrite grain boundaries and was closely associated with the $M_{23}C_6$. The $M_{23}C_6$ was probably providing sites that are denuded in chromium which would promote the nucleation of austenite. In the vicinity of the grain boundaries the austenite again formed a cellular type structure with the $M_{23}C_6$ (39). After further aging for 20 hours at 800°C the austenite began to grow as laths into the ferrite grains. There was evidence that the $M_{23}C_6$ after long aging times began to redissolve. The reason for this is that it is possible that $M_{23}C_6$ is not an equilibrium phase, and that the chromium partitioned to the ferrite whilst the carbon partitioned to the austenite. This would undersaturate the ferrite with respect to $M_{23}C_6$ which consequently dissolved. This re-resolution of the $M_{23}C_6$ after long aging times has been observed by Lismer et al (16).

5.1.2. The Attainment of Equilibrium

It is well known that the Fe-Cr-Ni alloys, at temperatures below 900°C, are slow to reach equilibrium. This has necessitated the use of long aging times together with the use of prior cold working to accelerate the approach to equilibrium. Unfortunately the use of cold working led to a very fine structure which made it difficult to carry out quantitative micro-analysis. It is essential that equilibrium has been reached before micro-analysis is carried out since the compositions of the phases will not be on the phase boundaries until equilibrium is reached. For this to be the case the composition of a particular phase must be uniform throughout the grain. Fig. 23 shows a series of elemental X-Rays

scans across an austenite grain for iron, chromium and nickel. It is clearly demonstrated that within experimental error the element composition across the grain was constant, thereby confirming that the alloys had indeed reached equilibrium. Micro-probe analysis on a series of specimens from alloy 3A(18Cr-2Ni) used to study the transformation characteristics at 800°C are given in Fig. 24(a) for the nickel content of the transforming austenite with time. In comparison, the volume fraction of the austenite is shown in Fig. 24(b). It can be seen that the nickel content of the austenite phase rises to a constant value after ~ 20 hrs. This could lead to some difficulty in interpretation since the implication that the concentration of elements in one phase was in equilibrium must dictate that the second phase is also in equilibrium in a two phase system. If this were the case then there would be no further change in the constitution and the alloy would be in equilibrium. Clearly this is not the case since the volume fraction of the austenite phase continues to increase for up to ~ 200hrs.

It is thought likely the explanation of this apparent contradiction lies in the fact that the partitioning of nickel in this particular alloy is quite small. It is probable that the partitioning of the nickel is asymptotic and reaches a value quite close to equilibrium relatively quickly and that the quantitative analysis technique is not sufficiently accurate enough to detect the further small changes of nickel concentration with time.

5.1.3 The Isothermal Sections of the Fe-Cr-Ni Ternary System

The experimental evidence on the constitution of the Fe-Cr-Ni system has been presented in the form of isothermal sections,

Figs. 25-30, for temperatures ranging from 1150°C to 650°C. There are two basic forms of the isothermal sections:-

1. At 950°C and above the diagram consists of two single phase fields of austenite and delta ferrite with a two phase region between them, Fig. 25. This general form persists to the solidus and is in good agreement with the most recent review of the Fe-Cr-Ni system by Rivlin and Raynor⁽⁹⁾. The broken lines in Fig 26 represent the position of the phase boundary at 1100°C according to reference (9).
2. At 900°C and below sigma, is also present as an equilibrium phase which complicates the diagram. The form of the diagram remains the same down to 650°C, the most important point being the tendency for sigma to be stable at lower chromium levels so that the (austenite + sigma phase) field extends further towards the iron-rich corner of the diagram as the temperature decreases. The broken lines within the two phase fields are experimentally determined tie lines and conform well with the geometry of the two phase fields.

5.1.4. The Effect of Fourth Element Additions

The microstructural changes occurring with the addition of a fourth element to the base Fe-Cr-Ni alloys have been investigated using quantitative microscopy. In the first instance the austenite forming elements:- manganese, copper, carbon and nitrogen and the delta_ferrite/sigma phase forming elements:- silicon, molybdenum, niobium and titanium were added in various amounts to study their effect on the constitution. Temperatures of 1050°C and 800°C were chosen such that the alloying effects could be studied at the high temperature (austenite + delta ferrite) region and the low temperature (austenite + sigma phase) region. The equilibrated

alloys were examined to determine the change in volume fraction of the delta ferrite or sigma phase as the amount of the fourth element addition increased.

5.1.4.1. Austenite Forming Elements (Mn,Cu,C and N)

(a) 1050°C

The general effect of the austenite forming element was, as would be expected, to reduce the amount of delta ferrite, but the copper additions had a non-linear effect on the amount of delta ferrite. At an addition of 7.5wt%Cu the microstructure contained a copper rich phase generally found at the grain or phase boundary triple points. This must be due to the solubility for copper in this alloy being exceeded and could account for the severe hot shortness found in these types of alloys with relatively high copper additions. This would suggest that the solubility of copper is somewhat lower than is generally believed for these alloys, although it is known that chromium additions will reduce the solubility of copper in Fe-Cr-Ni alloys. (89)

Additions of carbon had a relatively large effect in reducing the delta ferrite content, but this was complicated by the precipitation of $M_{23}C_6$, which is quite clearly seen in Fig 39. The amount of carbon and chromium that is combined as $M_{23}C_6$ must be taken into account when a quantitative analysis of the effects of alloy additions is performed. The graph shown in Fig. 55 indicates the reduction in the volume fraction of delta ferrite versus the bulk addition of the austenite forming elements. The erratic effect of copper is clearly seen.

(b) 800°C

The effect of the alloy additions at 800°C is summarised

in Fig.56.. It is apparent that at the lower temperature of 800°C, manganese becomes a sigma forming element above ~ 3wt% alloy addition, which can also be seen from the microstructures in Fig.41.

Nitrogen is clearly a strong austenite former but the addition of carbon which was made to a base alloy that was within the (austenite + sigma phase) field at 800°C, shows an inflection in its effect of reducing the sigma phase content. The carbon clearly stabilizes the austenite phase but is again complicated in interpretation by the precipitation of $M_{23}C_6$. Due account must be made for the carbon and chromium tied up as $M_{23}C_6$ when calculating the nickel equivalent values.

The effect of the copper addition at 800°C again changes from a delta ferrite stabilizer at the lower additions to essentially a neutral element at the higher levels of addition.

The results at 800°C suggest that manganese would be unsuitable as a substitute for nickel in the commercial austenitic alloys because of the tendency to promote the formation of sigma phase. It is not known why copper reverses its austenite forming capability as the copper content increases, although its low solubility will in any case limit the amount of copper that could be safely added without causing hot shortness.

Both carbon and nitrogen have large effects in reducing the amount of delta ferrite and sigma in the alloys which is advantageous when the stability of the austenitic structure is important. There was no detectable formation of nitrides at 1050°C or 800°C which may well have distinct benefits by not reducing the contents of other elements

from solid solution, whilst at the same time stabilizing the austenitic structure. On the other hand a relatively small addition of carbon promoted the precipitation of $M_{23}C_6$, which in itself reduced the amount of chromium in solid solution and this could affect the corrosion resistance of the alloy. It is well known however that the precipitation of $M_{23}C_6$ on the grain boundaries enhances the creep resistance of the alloy and that $M_{23}C_6$ is precipitated deliberately in the austenitic creep resisting alloys.

5.1.4.2. Ferrite/Sigma Phase Forming Elements (Si,Mo,Nb and Ti)

(a) 1050°C

At the higher temperature silicon is a very effective delta ferrite former producing a change in volume fraction of the delta ferrite from 0.41 to 0.74 with the addition of 3.75wt%Si. The potent effect of silicon as a delta ferrite former would appear to be linear, as shown by the straight line relationship between the change in delta ferrite content and the Wt%Si addition, Figs. 57,58.

All the other elements were less potent as delta ferrite formers than silicon, although their effects were complicated by the precipitation of carbides and in the case of the niobium additions, by the formation of Laves phase, Fe_2Nb , which is clearly seen in Fig. 48(c). The general effect of the formation of carbide and intermetallic phases will be to reduce the effective amount of the alloy addition in solid solution, and also in the case of carbides to reduce the level of carbon which in itself will have an effect on the constitution and microstructure. Thus, the effect of carbide precipitation is two-fold in reducing the effective delta ferrite forming capabilities of the alloying

additions and the effect of the carbon itself in stabilizing the austenite phase whilst in solid solution. These effects are represented in Fig. 57 by the apparently poor delta ferrite forming ability of the carbide forming additions.

(b) 800°C

At the lower temperature silicon, whilst still having a constant effect with alloy addition, is a somewhat less potent sigma phase former than ferrite former. Both molybdenum and titanium are effective sigma phase formers after the effect of carbide precipitation has been taken into account. The precipitation of a Laves phase in the 2wt%Nb alloy was not detected at this temperature which would agree with the tendency of Laves to be a high temperature phase and to be unlikely to precipitate in the presence of sigma phase. Nevertheless the sigma phase forming capabilities of niobium are small when compared with the other sigma forming elements such as molybdenum and titanium.

5.1.5 Nickel and Chromium Equivalents

In order to quantitatively assess the effects of the alloying elements on the constitution, in terms of nickel or chromium equivalents, the effects of nickel and chromium must first be determined. These effects have been calculated using the isothermal sections of the Fe-Cr-Ni ternary diagram so that the potency of either austenite, delta ferrite or sigma forming elements may then be determined. The method used compares directly the amount of an alloying element with the corresponding amount of nickel or chromium necessary to produce the same change in the microstructure.

It is recognised that in general the potency of a particular element will vary with the amount added, generally becoming weaker

Insert : A

In the case of Mn and Cu additions, where the addition was large, this inevitably resulted in a commensurate decrease in the Ni and Cr contents of the alloys. In order to obtain a realistic Ni equivalent for the quaternary addition, the nickel required to produce the same constitutional change as the quaternary addition was augmented by the amount by which the nickel had been reduced compared with the base ternary alloy. It should be borne in mind that this could have considerably over-emphasised the nickel equivalent value, but such an over-emphasis would only be markedly significant where large (i.e. 8%) quaternary additions were made.

in effect as the amount of alloy addition increases. The results therefore are presented as graphs of percent alloy addition versus the nickel or chromium equivalent.

5.1.5.1 Austenite Forming Elements (Mn, Cu, C and Ni)

The nickel equivalent of manganese is shown in Fig 61. At 1050°C the value ranges from 1.25 at about 1wt%Mn down to ~ 0.75 for 8wt%Mn. At 800°C, Fig 61, shows the Ni equivalent becoming negative, indicating that at the lower temperatures manganese is a sigma or even a ferrite former and not an austenite former as is widely believed. It was thought better to present manganese as a negative nickel equivalent rather than as a chromium equivalent since the two are not precisely the same. Also an examination of the isothermal section of the ternary equilibrium diagram shows that from the position of the base alloy (35Cr-28Ni) a reduction in nickel content rather than an increase in chromium will tend towards the (austenite + sigma phase) field. Hence above ~ 3wt%Mn the nickel equivalent of manganese at 800°C becomes negative.

The nickel equivalent of copper is given in Fig. 62. Because of the erratic effect copper has on the constitution and microstructure the curves are difficult to interpret.

The nickel equivalent at 1050°C decreased sharply after 1wt%Cu followed by a gradual increase as further copper was added. The nickel equivalent at 800°C was entirely negative, but became zero at ~ 7.5wt%Cu.

Insert →
Ⓐ The effect of carbon on the constitution was complicated by the formation of the $M_{23}C_6$ carbide phase. This essentially removes

carbon, chromium and a small amount of iron from solution, assuming the stoichiometry of the phase to be $(Cr_{21}Fe_2)C_6$. To quantify the effect of carbon on the constitution it was necessary to determine the amount that remained within the matrix of the alloy since it was the carbon that was in solid solution in the matrix that affects the constitution.

The amount of carbon lost to the carbide has been determined from a knowledge of the volume fraction of the carbide phase present and the density of the individual phases. Since the alloy used had a high percentage of chromium the density of the matrix phases austenite, ferrite and sigma was taken to be $7.9 \times 10^3 \text{ kg.m}^{-3}$. The value was chosen because it had been found both in the literature (section 4.3.2.2) and by the analysis of results from the base ternary alloy work that the densities of the γ , α and σ phase were very similar and that the value chosen represented the higher chromium containing alloys, see Pearson⁽⁸⁷⁾. The density of $M_{23}C_6$ was given by Goldshmidt⁽⁹⁰⁾ as $6.97 \times 10^3 \text{ kg.m}^{-3}$.

It is evident from the data presented that at 800°C the solubility of carbon was approaching zero. The values calculated for carbon in the $M_{23}C_6$ generally agrees well with the bulk carbon addition to the alloy. Further, in all cases the carbon as $M_{23}C_6$ at 800°C was slightly higher than that added. This must be due to errors either in the determination of the volume fraction of $M_{23}C_6$ or the bulk concentration of carbon in the alloys. It is noted that the error in the volume fraction was taken as a maximum of $\pm 2.4\%$ which could account for the excess carbon given for the 800°C sample since 1% by volume of $M_{23}C_6$ is equal to 0.045wt%C in the alloy. Conversely the chemical determination of the carbon content,

which uses the technique of burning off the carbon to combine with oxygen, may be giving a low value, due to the high chromium levels increasing the fusion temperature of the material, thus giving incomplete burning of the sample and a resultant low carbon determination.

Accepting the possible errors, it is clear that very little carbon is left in solution after the equilibrating treatments at both 1050°C and 800°C. It is then impossible to adopt the approach used to quantify the effects of carbon which has been used for the other fourth element additions. A further significant factor is the depletion of chromium from the matrix, although the removal of chromium given in Table 7 cannot in itself account for the observed changes in constitution. It is probable that the constitutional changes are due to a combination of effects such as the removal of chromium from the matrix and also the carbon addition, which will appreciably alter the base ternary equilibrium diagram, because of its austenite forming ability.

Unfortunately because of the vanishingly small solubility of carbon in these alloys it has not been possible to produce a graph of carbon content versus the nickel equivalent. The nickel equivalent for nitrogen however was very consistent over the temperature range studied. There was very little change in the equivalent value with either temperature or the amount of nitrogen addition, the value being ~ 22 for nitrogen additions of 0 to 0.014wt%. The nickel equivalent of nitrogen at 1050°C and 800°C is given in Fig. 63

5.1.5.2 Ferrite Forming Elements (Si, Mo, Nb and Ti)

The effect of chromium on the microstructure of base ternary alloys was determined in the same manner as that for nickel. The chromium equivalent were calculated by comparing the effect of

the alloying additions against the relative effect of chromium.

Silicon is a potent delta ferrite former at 1050°C but has markedly less effect as a sigma former at 800°C. At 1050°C the relative strength of the silicon as a delta ferrite former decreases as the alloy addition increases. However at 800°C the effect of silicon as a sigma former could be regarded as constant, within experimental error, up to ~ 4wt%Si. Fig 64 presents the chromium equivalent curves for silicon at 1050°C and 800°C.

The chromium equivalent curves for molybdenum are shown in Fig 65 and plainly indicate that molybdenum is more potent as a sigma former than a delta ferrite former. The shape of the curve at 1050°C is consistent with the molybdenum forming a carbide of the Mo₆C type and hence having a zero chromium equivalent up to ~ 1wt%Mo. The chromium equivalent then increases sharply up to ~ 2wt%Mo before decreasing as further additions are made. This result is consistent with the general effect that the potency of the alloys as austenite, delta ferrite or sigma formers decreases with increasing alloy addition.

Molybdenum is a known sigma phase former and exhibits a higher chromium equivalent at 800°C which is within the (austenite + sigma phase) region. There was a slight increase in the chromium equivalent after ~ 1wt%Mo, before the effect levelled off towards 4wt%Mo.

The curves for the chromium equivalent of niobium are shown in Fig 66. Niobium displayed a similar type of effect on the constitution as did molybdenum except that niobium was a stronger ferrite former at 1050°C than a sigma former at 800°C.

The effect of the intermetallic Laves phase, Fe_2Nb , present at the higher temperature has been taken into account for the determination of the chromium equivalent for the 2wt%Nb addition.

The effect of titanium, Fig 67, clearly shows that it was quite potent as a delta ferrite former at $1050^{\circ}C$. It must be noted however that the titanium content of the matrix has been adjusted for both carbon and nitrogen and that the nitrogen was somewhat higher in the titanium alloys than was found in the general run of the alloys, ranging from .015 to .027wt%N₂, whilst the nitrogen content in general was below .01wt%. This may have caused a correction that was too large since it is unknown how much carbon or nitrogen will remain in solution. Nevertheless the curves follow the same general trend of a less pronounced chromium equivalent effect as the alloy addition was increased.

The sigma forming potency of titanium was still increasing with increasing level of addition at $800^{\circ}C$, although it seems likely that the effect will be less potent as further titanium is added.

5.1.5.3. Comparison with Existing Equivalent Data

Since all the previous data for nickel and chromium equivalents has been presented in the form of a single value, it is difficult to compare directly the commonly used values with this work. Table 1 summarises the results that have been published and is presented as the relative tendency of the elements to form delta ferrite.

Where comparisons can be made for the austenite forming elements the values are given as austenite formers for this work and are compared against delta ferrite formers which for

manganese will be a negative value. However a direct comparison of the data for the austenite forming elements shows generally good agreement with the published values. Manganese has been quoted as -2 and -0.5 by Thielemann⁽²⁶⁾ and Newell⁽²⁷⁾, which certainly encompasses the range of values from 1.3 to 0.75 determined in the present work.

The value of Binder et al⁽²⁸⁾ for nitrogen compares very well with the nickel equivalent for nitrogen given in this work at both 1050°C and 800°C.

All the chromium equivalent values can be compared directly with the published data and it is interesting to note that Thielemann⁽²⁶⁾ gives the most potent delta ferrite former as titanium, which is in agreement with the present work although the value quoted of 7.2 is somewhat higher than suggested in this work. Also the order of potency suggested by Thielemann⁽²²⁾ is generally the same as that presented here, but again giving values that are generally higher. The value of chromium equivalent for silicon given by Pryce et al⁽²²⁾ of 3 is in excellent agreement with an average value obtained by this work at 1050°C. The value for molybdenum, given by Binder⁽²⁸⁾ of 1.4 and that of Schaeffler⁽²⁰⁾, De Long⁽²¹⁾ and Pryce et al⁽²²⁾ who all give a value of 1, are well encompassed by the range of values present for molybdenum on Fig 67 at 1050°C. The value of 0.5 for the chromium equivalent for niobium given by Schaeffler⁽²⁰⁾ and De long⁽²¹⁾ is lower than the range of values obtained in this work. The only comparison of the chromium equivalent of alloying additions as sigma formers is the result given for titanium by Hattersley et al⁽¹¹⁾ who worked on very similar alloy compositions

to those used in the present work, essentially studying the effects of titanium on the austenite/(austenite + sigma phase) boundary in Fe-Cr-Ni base ternary alloys. The range of values they obtained was from 1.2 to 1.9 which compare very well with those presented in Fig 67. although Hattersley's values are for a range of temperature.

It would appear that the results obtained for the sigma forming capabilities of elements, is the first time that the distinction has been made between their effects on sigma phase and on delta ferrite. Hence no comparison can be made for the lower temperatures used in the present work. However the potency of the elements as sigma formers is generally less than their potency as delta ferrite formers, the exception being molybdenum which is a known sigma former.

For the data to be used reliably for the prediction of the constitution of Fe-Cr-Ni alloys it must be noted that the values refer to alloys that are essentially carbon and nitrogen free, and adjustments must be made to account for amounts of interstitial elements present in commercial alloys. Also the effects of the alloy additions have been determined for specimens that have been equilibrated for long periods, and may not therefore be representative of cast or unequilibrated structures. Finally it would seem reasonable to suggest that the values of nickel and chromium equivalents can be applied only to alloys that are within the range of compositions investigated in this work.

The adjustment of the bulk concentrations of the fourth element addition for the purpose of the determination of nickel and chromium equivalents has been made somewhat arbitrarily, by deciding that all the carbon and nitrogen, where appropriate, is available to form carbides, nitrides or a combined carbonitride. In most cases the

adjustments were minimal, the most significant being that for molybdenum because of the M_6C type carbide that is formed whereas titanium and niobium for a $M C$ type carbide.

The practical significance of the chromium and nickel equivalent values which have been presented, will enable the prediction of phase stability with greater accuracy than previous data has allowed. It has been established in this work that the effect of the various austenite and ferrite forming elements, excepting nitrogen, alter as a function of concentration. The present work has established the equivalents of the austenite/ferrite forming elements, over a range of compositions which cover the common levels of additions to the austenitic stainless steels and iron-nickel based superalloys that are commonly used as wrappers and canning material in fast reactors. Further, at lower temperatures the distinction between the effect of the alloying additions as ferrite and sigma formers has been presented, which will again increase the accuracy of the nickel and chromium equivalent approach to predicting phase stability.

5.1.6 Partitioning of the Fourth Element Additions

This particular section of the work was carried out to investigate if there was a relationship between the partitioning of the alloy additions and the relative effects the alloys had on the constitution. The results obtained using a microprobe analyser with a wavelength dispersive spectrometer are presented in Table. 8.

Because of limited instrument availability it was only possible to carry out analysis on 3 series of the alloy additions,

Insert B

A mass balance calculation showed that the Mn and Si values obtained in the partitioning determinations led to total Mn and Si contents for alloys which were somewhat different from the average chemical compositions reported in Table 4. It should be noted however, that these partitioning results were obtained by micro-probe analysis, and were normalised to 100%. Thus they may well be inaccurate compared with the chemically analysed bulk compositions.

namely, manganese, copper and silicon.

A partitioning parameter (P) can be defined as:-

$$(P) = \frac{\text{wt\% alloy in austenite}}{\text{wt\% alloy in ferrite}} \text{ ----- (46)}$$

Thus the greater the difference of P from unity, the greater is the degree of partitioning. Values of the partitioning parameter (P) are given in Table 8.

nsent
⑧ → In all cases partitioning tended to increase as the fourth element concentration increased, except for the case of silicon for which partitioning appeared to be constant above 2wt%Si, at ~0.88.

For manganese and silicon the partitioning was not very high, particularly for silicon, which, at 1wt%Si had not partitioned at all within experimental error and yet had a significant effect on the constitution. Silicon is four times as effective as chromium in increasing the delta ferrite content at this level of addition. In the case of manganese a similar situation can be seen to apply, with very little partitioning, although in all cases the partitioning was always in favour of the phase that was stabilized by the element concerned. The results for copper showed a significant degree of partitioning of the copper to the austenite phase. Significantly the very high partitioning of the copper to the austenite phase had markedly increased the chromium content of the delta ferrite phase, which may in some part explain the erratic effect of the copper addition, stabilizing the delta ferrite by rejecting chromium from the austenite phase and thereby reducing the volume fraction of austenite and increasing that of the delta ferrite. It is unfortunate that the

partitioning at the 1wt%Cu addition was not analysable, due to the non-uniform distribution of the copper within the individual phases, which in itself may well account for the variable effects of the copper additions on the constitution of the alloys.

The effect of partitioning on the constitution of the quaternary alloys is complex because in the tetrahedron representing the isothermal quaternary equilibrium diagram, the tie-lines do not lie in a plane parallel to the Fe-Cr-Ni face of the tetrahedron. In fact these tie-lines make different angles with the Fe-Cr-Ni face for different amounts of quaternary alloy addition. Consequently in attempting to interpret the effects in terms of the Fe-Cr-Ni equilibrium diagram, it is the projection of the tie-lines on this diagram which is being used. This projection will depend upon the angle the actual tie-lines make with the Fe-Cr-Ni face of the quaternary tetrahedron and consequently the constitution is not readily accounted for by these projected tie-lines.

5.1.7 Prediction of Phase Stability

The concept of using the average electron vacancy number of an alloy to predict the formation of sigma phase in austenitic stainless steels and super alloys has been developed over many years, and has been successfully used in the design of alloys. The development of electron vacancy calculations has centred mainly on the superalloys, and essentially determines the electron vacancy number N_v of the matrix of a particular alloy. If the value of N_v is greater than a certain value, an alloy of that composition will be prone to sigma formation. It is widely acknowledged that the void swelling characteristics of a particular alloy are critically dependant upon the constitution,

and data has been produced, Fig 9, showing the relationship between swelling percent and the average electron vacancy number of the alloy. It is noted that when the value of N_v is equal to or greater than 2.5, void swelling increases sharply, and as N_v can be related to composition alloys that are susceptible to void swelling may be predicted.

The theory has been developed from pioneering work by Pauling⁽²⁹⁾ who determined the individual electron vacancy numbers for the elements from a consideration of the bonding and non-bonding orbitals of the 3d shells of the transition elements.

A similar approach, initially developed to predict the formation of intermetallic compounds, has been used by Hume-Rothery⁽⁹¹⁾. Essentially it uses the number of electrons per atom, e/a , and Hume-Rothery suggested that intermetallic phases would precipitate when the average e/a ratio reached a certain value. This approach took no account of the 3d orbitals that are required for bonding, whereas Pauling's work does account for the need of bonding orbitals in the 3d shell. However since the atomic size of the transition elements is very similar, the number of 3d orbitals required for bonding would be similar and so the individual electron vacancy numbers for the transition elements would simply decrease by 1 as the atomic number increased. This simplistic approach is now known to be inaccurate and other workers⁽⁹²⁾ have developed electron vacancy numbers from band theory which will take account of orbitals required for bonding, which is not a constant value for the transition elements.

For the commercial use of electron vacancy concepts, a

Insert C

The average values of N_v , e/a or V in Table 9 for the austenite/austenite plus sigma and austenite/austenite plus ferrite phase boundaries are very similar. This suggests that these two phase boundaries in the ternary system are closely parallel to a constant N_v , e/a or V number.

prediction of the composition of the matrices is necessary, which is, in the case of austenitic stainless steels and super-alloys, a very complex procedure that is based on assumptions about the microstructure and the type and composition of carbide and intermetallic phases that are precipitated. In the present work the individual matrix compositions have been experimentally determined and the relevant electron vacancy theories have been tested against the experimental results.

The isothermal sections of the ternary equilibrium diagram determined experimentally have been used to identify the compositions at which the formation of a second phase from austenite is expected, i.e. the austenite/sigma phase and austenite/ferrite phase boundaries. Using the phase boundary compositions, the methods developed by Pauling and Hume-Rothery and the electron valence numbers determined by Gabbay⁽⁹²⁾, the average values have been determined and are presented in Table 9. Two phase boundaries were chosen at 3 temperatures of 900°, 800° and 650°C, those being the austenite/(austenite + sigma phase) and the austenite/(austenite + alpha ferrite) phase boundaries.

It is quite clearly seen that the average electron valency numbers due to Gabbay⁽⁹²⁾, termed V, are by far the most consistent and it is suggested that a reappraisal of the present electron vacancy values may well be beneficial for the accurate prediction of second phase formation.

The individual element electron valence numbers determined by Gabbay⁽⁹²⁾ are given below:-

<u>Cr</u>	<u>Mn</u>	<u>Fe</u>	<u>Co</u>	<u>Ni</u>
3.4	3.5	3.5	3.2	2.9

5.1.8 Irradiation Damage

Introduction

A major aspect of the research programme has been the study of the constitution of iron-chromium-nickel alloys and their suitability for use in fast reactors. It is well known that the effects of irradiation on structural components in terms of the nucleation and growth of voids within the material is affected quite markedly by the alloy composition and constitution. The irradiation experiments undertaken have been carried out in an attempt to correlate the effects of alloy additions and constitution on the void swelling characteristics of two phase austenite + delta ferrite alloys within the iron-chromium-nickel system.

5.1.8.1 H.V.E.M. Irradiation

A typical series of micrographs obtained from an H.V.E.M irradiation study is shown in Fig.68. The sample was 1A(30Cr-13Ni) + 1wt%Si addition and Fig 68 shows the growth of voids within the foil as the irradiation dose increased. Whilst all the alloys investigated were two phase (austenite + delta ferrite) it was found that only the austenite phase exhibited appreciable void swelling under the operating conditions used. It is well known that the void swelling characteristics of alloys and structure types is temperature dependent and that body centred cubic phases tend to swell in a lower temperature regime than do the face centred cubic phases. Thus the ferritic phase showed a pronounced resistance to void swelling under the conditions used for the irradiation . Also the ferritic phase

suffered from pronounced oxidation at 500°C which prohibited the observation of the ferritic phase for any length of time.

The major advantage of the H.V.E.M. for irradiation experiments is its speed, the dose rate being $0.5 \text{ d.p.a. min}^{-1}$, which is considerably faster than any other simulation technique used at present (the typical dose for a fast reactor is $\sim 25 \text{ d.p.a. year}^{-1}$). Secondly the growth of the damage structure both in terms of voids and the dislocation network created as a consequence of the irradiation can be observed directly as the irradiation proceeds, giving a very clear indication of the void swelling characteristics of the alloy under investigation.

The disadvantages of using electrons to simulate neutron irradiation is the difference in the nature of the irradiating particles. Neutrons having a relatively large mass and low elastic scattering cross section, due to its charge neutrality, will generate high energy Primary-Knock-On (P.K.O.) atoms which are responsible for the cascades of damage which occur at the end of the path length of the P.K.O. These cascades are responsible for the vacancy rich areas, which collapse to form vacancy clusters and a network of dislocations formed as a result of the interstitials created in the collision process. It is worth noting that voids will not grow within the structure unless the temperature is high enough for vacancy diffusion and that it is known that vacancy clusters formed as a result of irradiation damage are stable up to $\sim 350^{\circ}\text{C}$. In comparison electrons, having an energy of the order of 1 MeV , are capable of dislodging only 1 atom from its lattice site per incident electron. It follows

that structural damage caused by electrons is different from the neutron case since no cascades are created. This is the major disadvantage of using electrons to simulate neutron damage. Nevertheless the use of the H.V.E.M. has produced many consistent results and is recognised as a useful method of irradiation simulation, offering a relatively easy and rapid technique of studying irradiation damage.

The effect of the fourth element additions on the void swelling characteristics of the alloys investigated are shown in Fig 69 and 70 for the additions of silicon and manganese respectively, silicon being added to alloy 1A(30Cr-13Ni) and manganese added to alloy 1F(34Cr-28Ni). The effect of copper on alloy 1F was also investigated, irradiation in the H.V.E.M. being carried out on the 7.5wt%Cu alloy which produced very low swelling results coupled with the production of a low dislocation density, shown in Fig 71(a). The addition of silicon is well known to reduce void swelling by its affinity for interstitials, hence not allowing them to escape from the vacancy rich region. This effectively allows recombination of interstitials and vacancies and thus reduces void swelling by eliminating the excess of vacancies. Manganese would appear to have a similar effect in reducing void swelling. However the 8wt%Mn alloy shown in Fig 71(b), shows a definite tendency for the voids to align themselves along crystallographic directions which was probably due to the distribution of the interstitial gases nitrogen and oxygen present in the alloys as trace elements. Specifically the nitrogen level of impurity increased as the manganese addition increased from 0.005wt%N to 0.023wt%N. In the V.E.C. manganese however had the effect of

markedly increasing the void swelling, whilst copper had a similar effect on void swelling, as it did on the alloy constitution, namely reversing its role as an austenite/ferrite former with increasing addition. It is probable that the residual gases will take up preferential sites within the lattice and thus provide preferential sites for void nucleation, Fig 71(b).

5.1.8.2 V.E.C. Irradiation

Whilst the use of the V.E.C. for the simulation of neutron damage has several disadvantages in terms of specimen preparation, highlighted in section (3.12), the use of energetic self ions to simulate primary-knock-ons produces damage within the specimen that is fundamentally the same as that for neutrons. 46 MeV Ni^{6+} ions were used to simulate self ions having a path length of $\sim 3\mu\text{m}$, this being primarily due to the high elastic scattering cross-section of the charged particles. The fixed-energy of the particles resulted in layer of damage within the specimen which is effectively equal in depth to the path length of the particle. The effective dose rate is approximately 2 d.p.a. hr^{-1} but because of machine constraints the dose must be built up in stages which has caused microstructural problems since it involves cycling the specimens between ambient and the test temperature several times for even moderate dose levels. This problem is particularly severe for alloys susceptible to martensite formation during cooling to ambient temperature.

The effect of V.E.C. irradiation on a series of alloys containing molybdenum is shown in Fig 72. The quantitative results of the V.E.C. irradiations carried out on alloys containing silicon,

molybdenum, manganese and copper are shown in Fig 73. Both silicon and molybdenum markedly reduced void swelling, silicon being the most potent whilst molybdenum had little effect up to the first 1Wt% addition.

A further effect on the microstructure of the specimen that had been irradiated was the formation of sigma phase and new austenite from the ferritic phase, shown in Fig. 74. The duration of the test was \sim 20hrs at 600°C and significant transformation of the ferrite had taken place. It is well known that transformations in these alloys at temperatures lower than 900°C are extremely slow, being in the order of hundreds of hours for the transformations to start at 600°C. Clearly the irradiation had significantly increased the transformation rate and sigma, as opposed to ferrite, had precipitated in this particular alloy. Under simple thermal conditions the alloy lies just within the (austenite + delta ferrite) phase field, Fig 29, but it is known that as the temperature decreases there is an expansion of the sigma phase field. Sigma is commonly found in irradiated austenitic alloys which would not be expected under purely thermal conditions. It is obvious that the diffusion rates of the species within the system are significantly increased as a result of irradiation, which would be expected since irradiation both dislodges atoms from their lattice sites and creates highly disordered regions within the material. It can also be seen from Fig 74 that the newly transformed austenite had begun to swell through the production of voids, whilst the sigma phase was void free.

5.1.8.3 General Discussion of Results

In terms of the base ternary alloys used it is clear that

an increase in nickel content of the alloy gave a decrease in relative void swelling $\frac{(\Delta V)}{V}$. Alloy 1B(27Cr-16Ni) had a relative void swelling $\frac{(\Delta V)}{V}$ value of 19.6 percent whilst base alloy 1F(34Cr-28Ni) had a corresponding $\frac{\Delta V}{V}$ -value of 3.4 percent. This is in agreement with other workers, Harries⁽⁶⁰⁾ showing that increasing the nickel content will have a pronounced effect on reducing void swelling.

A comparison between H.V.E.M. and V.E.C. irradiation, given the differences in operating conditions, would suggest good agreement for the results of void swelling, except for the case of manganese, although it has been noted that doubts exist as to the validity of the H.V.E.M. results on the 8wt%Mn alloy because of the non-uniformity of the void distribution, which would tend to give a result that was low. The effects of silicon and copper on void swelling show good agreement although only one H.V.E.M. result was obtained on a copper bearing alloy.

The reason why solutes affect void swelling is not fully understood although it is widely known that solutes will affect the defect trapping capability of the matrix. Silicon is known to trap interstitials because of the small size of the silicon atom providing extra volume for the interstitials. The effect will be that the interstitials cannot escape from the vacancy rich area and recombination and annihilation of the Frenkel pairs will be enhanced. This will reduce the number of vacancies available for void growth and swelling will be decreased. It must be noted that silicon will only have this effect whilst in solid solution, and precipitation of intermetallics such as Ni_3Si , which is now

well known in silicon bearing stainless steels, effectively removes the defect trapping ability of the silicon solute. Again a similar mechanism can be postulated for molybdenum, having a larger atomic size than the base components, will again form defect trapping sites that will effectively reduce the swelling because the compressively strained lattice will provide preferential sites for vacancies.

In an attempt to identify the nature of the very small voids in the $1F(34Cr-28Ni) + 7.5wt\%Cu$ V.E.C. irradiated specimen, (it was thought they may be a copper-rich precipitate), a transmission electron microscope microprobe analytical technique was used to identify the composition of the feature. It was found that whilst the features were in fact voids the copper content was increased around the void. It was also found that $7.5wt\%Cu$ was above the solubility for copper in this particular alloy, probably due to the high chromium level in the base alloy. It would then seem plausible to suggest that solutes such as copper, whose solubility limit has been exceeded within the alloy system, would migrate to void surfaces to reduce the overall energy of the system. The copper solute atoms will then combine with the vacancies as they arrive at the void and hence reduce the void swelling.

It is not understood why manganese increases the susceptibility of alloys to void swelling save that in the lower temperature regime below $900^{\circ}C$ its effects on the constitution would be opposite to the effect of nickel, which is known to reduce void swelling.

Clearly the void swelling characteristics of an alloy are

critically dependent on the constitution of the system, which was highlighted by Harries⁽⁶⁰⁾ who suggested that void swelling would be at a minimum in a single phase field, at a maximum in the three phase field and at an intermediate value in a two phase field. The results presented do not all fall into this general pattern, if one considers silicon which has a pronounced effect in increasing the proportions of ferrite or sigma phase whilst significantly reducing the relative void swelling. Molybdenum has a similar but reduced effect on both the constitution and void swelling to that for silicon. Manganese on the other hand displays the opposite effect by promoting sigma formation and increasing the void swelling of the alloys. The effect of copper in terms of void swelling can be compared with its effect on the constitution in that it appears to reverse its effect on both the constitution and void swelling as the copper content increases.

5.1.9 Partitioning

The partitioning of the fourth element additions between the austenite/ferrite phases is somewhat surprising. Silicon had a very significant effect on the constitution and void swelling characteristics of the alloys, but there was no evidence of partitioning at 1wt%Si and only marginal partitioning between the austenite and ferrite phases as the silicon content increased, Table 8. For the manganese additions, a similar trend was shown, whilst for copper the partitioning was significant.

The relative effects of these alloy additions on the constitution and void swelling characteristics of the alloys cannot therefore be readily explained in terms of partitioning.

It would seem more likely that the fourth element additions have different effects on the stability of a particular structure type i.e. an addition of silicon for instance may increase the lattice strain energy of the face centred cubic austenite phase significantly more than it would for a body centred cubic delta ferrite phase. The changes in constitution observed, which for the case of silicon will be an increase in delta ferrite content, are then seen in the context of reducing the overall lattice energy of the alloy. The evidence of this work would suggest that this is a more plausible explanation for the observed constitutional changes rather than simple solute partitioning.

6 Conclusions

6.1 Base Ternary Constitution

(I) The constitution of the Fe-Cr-Ni ternary system has been investigated by micro-probe analysis and is presented as isothermal equilibrium sections at six temperatures with the range 1150°C to 650°C.

(II) The form of the isothermal sections were consistent with the published data although several differences in the shape of the phase fields and boundaries in the isothermal sections were found, compared with previously published data.

(III) The two and three phase regions consisting of (austenite + sigma phase) and (austenite + ferrite + sigma phase) were found to be stable at lower chromium and higher iron contents than reported previously. Sigma was an equilibrium phase at 18wt%Cr at the iron rich corner of the (austenite + sigma) phase field at 650°C.

(IV) The three phase region (austenite + ferrite + sigma phase) which is found at the higher nickel side of the (austenite + sigma phase) region, extended to higher chromium levels as the temperature decreased. The ferrite triple point of the three phase field contained 84wt%Cr at 650°C. The same three phase field however, did not extend to the high nickel levels of 43wt%Ni in earlier work by Andrews⁽³⁾. In particular alloy 1F(34Cr-28Ni) which was designed to fall within the (austenite + sigma phase) field was in fact within the (austenite + ferrite) phase field at all temperatures down to 650°C.

(V) The form of the (Fe-Cr-Ni) ternary system presented in this work shows good agreement with the recent

critical review by Raynor and Rivlin⁽⁹⁾, particularly at 800°C and above.

(VI) Isothermal transformation of delta ferrite resulted in a structure of (austenite + ferrite) which generally formed as a cellular structure. This became finer as the temperature decreased. The austenite and ferrite showed the Kurdjumov-Sachs orientation relationship, namely:-

$$\begin{aligned} \{111\}_{\gamma} & // \{110\}_{\alpha} \\ [\bar{1}\bar{1}0]_{\gamma} & // [111]_{\alpha} \end{aligned}$$

(VIII) Isothermal transformation which resulted in a structure of (austenite + sigma phase) occurred by the transformation of the delta ferrite phase initially to sigma, resulting in an envelope of sigma phase forming around the transforming ferrite grain. The formation of sigma phase continued until the equilibrium composition of (austenite + sigma phase) was reached for that particular alloy, and thereafter a cellular structure of (new austenite + sigma phase) began to precipitate and consume the remaining ferrite.

6.2. Nickel and Chromium Equivalents of the Fourth Element Additions

The relative potency of the fourth element additions as nickel and chromium equivalents varied with the amount of alloy addition, generally becoming less potent as the alloying addition increased. The values of nickel and chromium equivalents over the range of alloy additions made are given in graphical form in Fig 61-67, which gives the nickel and chromium equivalents as a function of fourth element addition at 1050°C and 800°C, which was the temperatures at which the quaternary alloys were equilibrated.

6.3. Partitioning of the Fourth Element Additions

For the elements investigated the partitioning of the fourth element additions between the austenite and ferrite phases was less than expected although in all cases the partitioning increased as the alloy additions increased.

Partitioning is expressed by the parameter P defined as the ratio of fourth element addition in the austenite phase to that in the ferrite phase. The results obtained were:-

<u>Alloy Addition</u>	<u>Partitioning Parameter (P)</u>
1Wt%Mn	1.21
3Wt%Mn	1.40
8Wt%Mn	1.49
2Wt%Cu	3.21
7.5Wt%Cu	4.17
1Wt%Si	0.98
2Wt%Si	0.88
3.75Wt%Si	0.89

6.4 Electron Vacancy Phase Stability Prediction

The electron vacancy values due to Gabbay⁽⁹⁰⁾ were the most consistent for predicting the phase stability of austenite over a wide range of alloy compositions. The electron vacancy values for Fe, Cr and Ni being:- 3.5, 3.4 and 2.9.

6.5 Irradiation Damage

(I) For VEC irradiation at 600°C the addition of manganese increased the relative void swelling $\frac{\Delta V}{V}$ from 3.50% to 17.0% for an addition of 8Wt%Mn and a dose of 40 d.p.a.

This behaviour was inconsistent with the effects of manganese during H.V.E.M. irradiation at 500°C.

(II) Copper exhibited variable behaviour under VEC irradiation, first increasing the swelling followed by a decrease as further additions of copper were made.

The VEC irradiation results for copper at 7.5Wt% addition

agree well with a result for the same alloy in the H.V.E.M., both irradiations predicting low void swelling.

(III) Silicon exhibited a pronounced ability to suppress void swelling in the VEC, reducing the value of $\frac{\Delta V}{V}$ from 19.00% to 4.5% for the addition of 1Wt%Si and a dose of 40 d.p.a.

A similar although less potent effect was evident for silicon in the H.V.E.M. irradiation. An alloy containing 4Wt%Si exhibited no swelling when irradiated in the H.V.E.M.

(IV) Molybdenum containing alloys irradiated in the VEC showed a pronounced tendency to reduce void swelling from 19.5% to 7% as the molybdenum addition increased from 0Wt% to 3.74Wt%

7 Future Work

In common with all experimental research work the questions answered are generally outweighed by the question either unanswered or created as a result of the research work, this thesis being no exception.

7.1 Base Fe-Cr-Ni Ternary Constitution

There has been extensive work carried out on the constitution of the Fe-Cr-Ni ternary system. The results for the Fe-Cr-Ni system studied in this work are in very good agreement with the recent review of the system by Raynor and Rivlin⁽⁹⁾. Nevertheless results at 700°C and below are questionable because of the very long equilibration time required and the resultant fine structure developed.

The quantitative microanalysis of phase composition of very small volumes has been made possible by the advent of the S.T.E.M. facilities. It would be of real benefit to extend the technique of phase boundary determinations used in this work to alloys equilibrated at lower temperatures with frequent cold work. The resultant fine structures could be analysed quite adequately coupled with the precise techniques of phase identification using selected area electron diffraction.

It is also thought possible that the use of diffusion couples, provided equilibrium was obtained, would provide a very useful method of producing a specimen of varying composition and hence range of "alloys" from one specimen.

7.2 The Effect of Fourth Element Additions

Generally the effects observed in terms of the constitution were much as was expected. However several alloying elements, particularly manganese and copper, did not act as simple austenite formers.

Manganese was a potent sigma phase former at 800°C and copper had a variable effect, changing from a delta ferrite former to austenite former as the alloy addition changed. Clearly the commonly held view on the effects of these elements is in need of reappraisal. Also, whilst no direct evidence has been found in this work, it is thought that the base alloy composition itself, may have a bearing on the effect of the various alloy additions. This will undoubtedly affect the various "potencies" of the alloy additions as the base composition changes. It follows that the effect and potency of alloying additions on the constitution may well be different when added in the presence of other alloying additions which is the general case in reality. Thus it would also be of value to study the effect of multi-alloying additions.

7.3. Partitioning of Alloy Additions

In a duplex alloy the amount of partitioning between the phases of the alloy components is of real importance. Many properties rely on the composition of the matrix. Unfortunately the partitioning results for the present work are not extensive and further work on partitioning would again be advantageous. The results presented would suggest that elemental partitioning between the component phases is somewhat less than expected particularly at the lower levels of addition.

7.4. Irradiation Damage

The irradiation work undertaken in this project has resulted in a quite limited assessment of the effects of various alloying additions on the void swelling properties of certain duplex stainless steel compositions. Before any quantitative model of the effects of compositional changes for real steels can be proposed,

it is necessary to determine the effects of individual alloy additions. It is recognised that many alloys added together, may not have the same effect as when added singly . Nevertheless a better understanding of the compositional and constitutional effects on void swelling will require the determination of the effects of the individual additions over a range of temperature and doses.

References

- (1) Jenkins C.H.M., et al, J.I.S.I., 136 1937 p.187.
- (2) Bradley A.J., et al, An Xray Investigation of Iron-Chromium-Nickel Alloys, J.I.S.I. 2 1941 p.273
- (3) Andrews K.W., The System Iron-Chromium-Nickel, United Steel Companies Report 1950.
- (4) Schafmeister P., et al, Arch Eisenhüttenwes, 12 1939 pp.459-464.
- (5) Rees W.P., et al, Constitution of Iron-Chromium-Nickel Alloys at 650^o-800^oC, J.I.S.I. July 1949 p325.
- (6) Cook A.J., et al, ibid, 171 1952 pp.345-353.
- (7) Kaufman L., et al, Computer Calculations of Phase Diagrams, Academic Press, New York 1970.
- (8) Hillert M., Hardenability Concepts with Applications to Steels, Eds Doane & Kirkaldy, Met Soc. of A.I.M.E. 1978, p5.
- (9) Raynor G.V., et al, A Critical Evaluation of the Iron-Chromium-Nickel System. International Metals Review 1980 No 1.
- (10) Jones J.D., et al, Constitution of Certain Austenitic Stainless Steel with Particular Reference To Aluminium, J.I.S.I. Jan 1966 p1.
- (11) Hattersley B., et al, Constitution of Certain Austenitic Stainless Steels. J.I.S.I. July 1966, p45.
- (12) Schultz J.W., et al, Metall Trans 3 1972 pp2479-2483.
- (13) Hasele M., et al, NBS Special publication 496, March 1978 pp910-954.
- (14) Irvine K.J., et al, J.I.S.I. 192 1959 pp227-228.
- (15) Pickering F.B., Evolution of Stainless Steels A.S.M./M.S. publication p3.
- (16) Lismer R.E., et al, J.I.S.I. May 1952 p49.
- (17) Pryce L, et al J.I.S.I. Nov. 1956 p289.
- (18) Nicholson M.E., et al, Trans A.S.M. 44 1952 p601.
- (19) Shao L., et al, Met Trans 10A May 1979 p585.
- (20) Schaeffler A.L., Metal Progress, Nov 1949, p680.
- (21) De Long W.B., Metal Progress, 77 1960 p98.

- (22) Pryce L., et al, J.I.S.I. 184 1956 pp289-301.
- (23) Pryce L., et al, ibid, Aug 1960 p145.
- (24) Hammond C.M., ASTM Special Technical Publication 369 1965, p48.
- (25) Eichelman G.H., et al, Trans.Am.Soc.Met., 45, 1953 pp77-95.
- (26) Thielemann R.H., Am.Soc.Test.Mat.Proc. 40 1940, p788.
- (27) Newell W.D., et al U.S.Patent 2118683 1938.
- (28) Binder W.D., et al, Trans.Am.Soc.Met. 41 1949 p1301.
- (29) Pauling L., Physical Review 54 1938, p899.
- (30) Rideout S.P., et al, J of Metals, Oct. 1951, pp872-876.
- (31) Sully A.J., et al, J. of Heat Treatment, 1 1948, p228.
- (32) Pearson W.B., Nature 167 1951, p110.
- (33) Greenfield P., et al, Trans A.I.M.E., 200 1955 pp253-257.
- (34) Greenfield P., et al, ibid, 206 1956, pp265-275.
- (35) Boesch W.J., et al, Metal Progress 86 1964 p109.
- (36) Woodyatt L.R., et al, J.TMS, 236 1966, pp519-527.
- (37) Decker R.F., Int.Symposium, (Strengthening Mechanisms in Steels) Zurich, Climax Molybdenum Co., 1969, p147.
- (38) Palentine T., Private Communication.
- (39) Beckitt F.R., J.I.S.I., May 1969, p632.
- (40) Pickering F.B., J.I.S.I. Special Report No. 64 1959, p118.
- (41) Southwick P.D., et al, Metal Science July 1980, p253.
- (42) Tuma H., et al, Arch Eisenhuettenwes, 41 No.10, 1976, p983.
- (43) Peckner D., et al, Handbook of Stainless Steels, McGraw-Hill, 1977.
- (44) Decker R.F., et al, Am.Inst.Min.Metall., Pet.Eng.,Con.Proc., 28, 1965, p69.
- (45) Andrews K.W., et al, Interpretation of Electron Diffraction Patterns, Hilger and Watts, 1967.
- (46) Sullivan C.P., et al, ASM Technical Report C70-9.1, 1970.

- (47) Denham A.W., et al, J.I.S.I. 207 1969, p585.
- (48) Chaturvedi M.C., et al, J.I.S.I. 207 1969, p593.
- (49) Kaufman L., et al, NBS Special Report 496, Gaithersburg, 1977.
- (50) Brown C., et al, J.Nucl.Mat., 66 1977, pp201-202.
- (51) Baron J.I., et al, J.Nucl.Mat., 51 1974, p266.
- (52) Greenwood G.W., et al, J.Nucl.Mat. 1(4) 1959, pp305-324.
- (53) Cawthorne C., et al, AERE Report R5269 1969, pp446-460.
- (54) Cawthorne C., et al, Nature 216 1966, pp575-576.
- (55) Nelson R.S., Ed., Proc. Consultant Symposium, Harwell AERE Report R7934, Jan. 1975.
- (56) Anderson R.G., KTG/BNES Conf.Karlsruhe, Dec. 1974.
- (57) Mayer R.M., et al, J.Nucl.Mat., 95 1980 (7 papers)
- (58) Glowinski L.D., et al, J.Nucl.Mat., 61 1976, p22.
- (59) Nelson R.S., et al, J.Nucl.Mat., 37 1970, pp1-12.
- (60) Harries D.R., Consultant Symposium Harwell, AERE Report R7934, Jan 1975, pp1-17.
- (61) Williams T.M., et al, J.Nucl.Mat., 88 1977, pp69-81.
- (62) Williams T.M., et al, ibid 68 1977, pp22-34.
- (63) Williams T.M., et al, ibid, 79 1979, pp28-42.
- (64) Makin M.J., et al, Int.Conf. Scottsdale, Arizona, June 1977.
- (65) Bramman J.I., et al, Proc.BNES Conf.Reading, 1971, p27.
- (66) Hudson J.A., et al, see Ref. 8, p213.
- (67) Stals L., et al, KTG/BNES Int.Conf. Karlsruhe, 1974, p132.
- (68) Johnston W.G., et al, J.Nucl.Mat. 54 1974, p24.
- (69) Harries D.R., ref 64, p287.
- (70) Johnston W.G., et al, Proc.ASM Mat.Sci.Seminar, Cincinnati, Nov. 1975, p429.
- (71) Watkin J.S., et al, Int. Conf. Scottsdale June 1977, p84.
- (72) Kaufman L., et al, Treatise on Solid State Chemistry, Plenum Press New York, 1975.

- (73) Mosedale D., et al, Int.Conf. Scottsdale, 1977, p129.
- (74) Harries D.R., et al, to be published.
- (75) Venker H., et al, J.Nucl.Mat, 60 1976, p347.
- (76) Bates J.F., HEDL-SA-1068, April 1976.
- (77) Leitnaker J.M., et al, J.Nucl.Mat., 49 1973/74, p57.
- (78) Bates J.F., ASTM Special Technical Publication No.570, 1970, p1.
- (79) Bloom E.E., et al, Scripta Met., 10, 1976, p303.
- (80) Nelson R.S., et al, J.Nucl.Mat. 37 1970, p1.
- (81) Bullough R., et al, Proc.BNES Conf., Reading 1971, p79.
- (82) Bagley K.Q., et al, Proc.BNES Conf., Reading 1971, p45.
- (83) Brager H.R., J.Nucl.Mat., 57 1975, p103.
- (84) Ellis J.A., et al, ASTM Special Technical Publication No611., 1976, p195.
- (85) Pickering F.B., Monograph No.1, The Basis of Quantitative Metallography, Inst. of Mets. 1976.
- (86) Gladman T., et al, J.I.S.I., 210 1972, p916.
- (87) Pearson A., A Handbook of Lattice Spacings. and structures of Metals and Alloys. Pergamon Press 1958.
- (88) Pickering F.B., Private Communication.
- (89) Salter W.J.M., J.I.S.I. Dec. 1967, p1619.
- (90) Goldshmidt H.J., Interstitial Alloys, Butterworth, 1969.
- (91) Hume-Rothery.W., Structures of Metals and Alloys, Inst. of Metals. London 1936.
- (92) Gabbay I., D.Phil. Thesis 1981, *Oxford Univ.*

TABLE 1

The potency of common additions in stainless steels given as the tendency to form delta ferrite after the reference given.

<u>Element</u>	<u>Thielemann</u> (26)	<u>Newell</u> (27)	<u>Binder</u> (28)	<u>Schaeffler</u> (20)	<u>Pryce et al</u> (22)	<u>Hattersley</u> (1)
C	-40	-30	-23	-30	-21	
N			-20	-30	-11.5	
Ni	-3	-1	-0.5	-0.5	-0.5	
Mn	-2	-0.5				
Ti	+7.2					1.2-1.9 (Sigma)
Si	+5.2			+1.5	+3	
Nb	+4.5			+0.5		
Mo	+4.2	+(2xCr)	+1.4	+1	+1	

(% delta ferrite change per wt% addition)

TABLE 2

The occurrence of intermetallic phases between alloying elements commonly found in austenitic stainless steels and nickel based super-alloys, after Decker cited in ref (43).

A

	Ti	Zr	Hf	V	Nb	Ta	Cr	Mo	W
Mn	Sigma B ₂ A Chi	B ₂ A Chi	B ₂ A Chi	Sigma BA Chi	B ₂ A Chi	B ₂ A Chi	Sigma Chi	Sigma Chi	Chi
Fe	B ₂ A BA Chi	B ₂ A	B ₂ A	Sigma BA Chi	Sigma B ₂ A	B ₂ A	Sigma	Sigma B ₂ A Chi Mu	B ₂ A Mu
Co	B ₂ A BA G	B ₂ A BA G	B ₂ A BA G	Sigma B ₃ A Chi	B ₂ A G	B ₂ A G	Sigma	Sigma B ₃ A Mu	B ₃ A Mu
Ni	B ₃ A BA G	G	G	Sigma B ₃ A Chi G	B ₃ A Mu G	B ₃ A Mu G	Sigma	B ₃ A	

B

Identification	Nominal Composition		Chemical Analysis		Micro-probe Analysis	
	FeWt%, CrWt%, NiWt%		FeWt%, CrWt%, NiWt%		FeWt%, CrWt%, NiWt%	
1A	57	30	56.11	30.25	55.09	32.03
1B	"	27	56.42	26.70	56.80	28.01
1C	"	25	56.70	25.40	57.22	26.14
1D	"	20	56.63	20.10	57.09	21.04
1E	"	15	57.39	15.21	57.99	15.97
1F	37	35	37.61	34.07	38.48	35.48
1G	"	32	37.42	31.94	53.77	22.98
1H	"	30	37.71	30.21	52.20	25.13
1I	"	25	38.54	24.44	38.02	25.29
1K	"	20	38.35	20.15	37.50	20.62
2A	86	12	84.14	12.26	83.39	12.77
2B	83	"	83.05	12.05	82.11	13.46
2C	78	"	78.11	11.92	78.36	12.22
2D	68	"	67.87	12.09	69.20	11.59
2E	58	"	57.54	11.70	59.49	12.26
2F	48	"	49.00	12.00	49.33	12.36
3A	80	18	79.78	17.94	79.12	18.97
3B	75	"	74.73	18.16	74.64	18.50
3C	72	"	72.07	18.03	70.80	18.79
3D	62	"	61.17	17.94	62.30	18.95
3E	52	"	52.03	18.07	52.35	18.73
3F	42	"	41.34	17.99	42.36	18.92
4A	38	45	-	44.80	.009	.020
4B	64	32	-	32.17	.015	.023

* Iron analysis by difference

Carbon, nitrogen and oxygen for the main series of alloys

C	.007 wt%
N ₂	.004 wt%
O ₂	.040 wt%

Manganese Series (1F)

<u>Identification</u>	<u>Mn Wt%</u>	<u>Cr Wt%</u>	<u>Ni Wt%</u>	<u>C Wt%</u>	<u>N₂ Wt%</u>
Mn0	0	34.07	28.22	0.001	0.003
Mn1	1.10	33.97	27.49	0.007	0.014
Mn3	2.95	33.35	26.30	0.005	0.016
Mn8	8.01	31.50	24.86	0.005	0.023

Copper Series (1F)

	<u>Cu Wt%</u>				
Cu0	0	34.07	28.22	0.001	0.003
Cu1	1.10	33.90	27.34	0.005	0.008
Cu2	2.12	33.60	26.27	0.005	0.007
Cu7	7.50	31.60	24.68	0.005	0.008

Carbon Series (1A+1F) + 2%Cr

C0		34.85	18.88	0.003	0.004
C1		33.90	18.81	0.090	0.003
C2		33.20	18.44	0.130	0.008
C3		33.70	17.98	0.280	0.004

Nitrogen Series (1G+3%Cr)

N0		33.91	29.00	0.009	0.004
N1		33.55	29.17	0.007	0.040
N2		34.45	29.26	0.006	0.068
N3		34.60	29.27	0.008	0.140

cont.

Cont. 2

Silicon Series (1A)

	<u>Si Wt%</u>	<u>Cr Wt%</u>	<u>Ni Wt%</u>	<u>C Wt%</u>	<u>N₂ Wt%</u>
S0	0	30.00	13.32	0.001	0.007
S1	0.85	29.80	13.14	0.001	0.007
S2	1.80	29.60	12.64	0.001	0.007
S4	3.75	28.90	12.61	0.003	0.007

Molybdenum Series (1B)

	<u>Mo Wt%</u>				
Mo0	0	27.00	16.30	0.009	0.007
Mo1	0.92	26.70	16.05	0.008	0.007
Mo2	1.98	26.30	16.05	0.009	0.005
Mo4	3.74	26.15	15.95	0.005	0.004

Niobium Series (1C)

	<u>Nb Wt%</u>				
Nb0	0	25.35	17.93	0.001	0.008
Nb $\frac{1}{2}$	0.48	25.30	17.82	0.001	0.012
Nb1	1.06	25.10	17.41	0.002	0.006
Nb2	2.16	24.75	17.00	0.001	0.007

Titanium Series (1B+1C)

	<u>Ti Wt%</u>				
Ti0	0	26.05	17.93	0.003	0.006
Ti $\frac{1}{4}$	0.34	26.10	17.11	0.006	0.016
Ti $\frac{1}{2}$	0.54	26.00	16.90	0.007	0.027
Ti1	1.05	25.60	16.69	0.006	0.015

TABLE 5

The microanalysis of the individual phase compositions
at the given equilibration temperature.

Phase Composition

Code	Temp °C	Austenite		Ferrite		FeWt%	Sigma CrWt%	NiWt%
		FeWt%	CrWt%	CrWt%	NiWt%			
1A	650	57.08	25.78	17.01		52.98	38.04	7.84
"	700	64.29	20.79	14.89		52.93	38.24	7.67
"	800	61.05	22.19	16.77		49.33	42.85	6.33
"	900	59.38	23.19	17.43		50.59	39.80	8.20
"	950	58.10	24.58	17.24	51.82			
"	1050	57.29	25.44	17.17	53.29	37.09		7.22
"	1150	57.60	25.40	16.88	53.96	34.79		8.54
								10.37
1B	650	56.57	25.19	18.09		52.52	36.79	9.64
"	700	57.92	22.87	19.31		51.69	37.32	9.91
"	800	58.67	21.88	19.63		47.52	43.36	7.54
"	900	58.44	23.40	18.20		48.81	41.73	8.18
"	950	57.94	24.19	17.84	50.89	40.21		7.64
"	1050	57.78	24.14	18.08	52.25	38.10		8.52
"	1150	56.94	25.43	17.54	53.25	35.27		10.59
1C	650	57.56	20.59	22.19		46.56	45.00	7.25
"	700	57.54	20.83	21.96		49.41	42.13	7.10
"	800	55.67	22.52	22.07		45.99	43.69	9.00
"	900	57.03	23.26	19.82		47.28	43.39	7.92
"	950	56.13	23.81	20.18	49.31	41.13		8.30
"	1050	55.19	25.02	19.80	51.55	37.54		9.90
"	1150	54.73	25.44	19.82	52.30	34.88		11.98

cont.

Cont. 2

Code	Temp	Phase Composition								
		Austenite		Ferrite		Fewt%	Sigma CrWt%	NiWt%		
		Fewt%	CrWt%	NiWt%	Fewt%	CrWt%	NiWt%	Fewt%	Sigma CrWt%	NiWt%
3A	650	78.04	16.50	5.45	80.37	17.71	1.92			
"	700	81.61	15.16	3.22	79.41	18.72	1.84			
"	800	80.09	14.62	5.29	80.37	17.83	1.80			
"	900	82.14	14.74	3.12	78.76	19.68	1.52			
"	950	82.03	14.70	3.25	79.29	18.99	1.70			
"	1050	82.59	13.77	3.64	80.50	18.05	1.45			
"	1150				Single Phase					
3B	650	76.58	18.13	5.24	76.00	21.59	2.34	61.55	35.39	3.03
"	700	76.10	17.56	6.97	71.29	26.91	2.53	60.07	36.89	2.76
"	800	74.97	18.12	6.87	70.05	27.46	2.46			
"	900	74.92	18.51	6.50	70.27	26.74	2.92			
"	950	74.62	18.61	6.74	70.93	25.75	3.15			
"	1050	74.46	18.92	6.59	71.06	25.20	3.73			
"	1150	74.56	18.89	6.49	71.87	23.89	4.16			
3C	800	71.66	18.28	10.05	67.64	28.65	3.71			
1F	800	40.90	26.20	32.90	20.67	74.32	5.01			
	900	38.80	29.67	32.86	25.18	65.03	7.49			
	950	38.30	29.98	32.20	28.14	60.24	9.65			
	1050	37.15	31.39	31.93	31.34	53.59	13.60			
1H	650	51.46	22.60	25.28				43.27	43.29	12.33
	700	50.65	22.97	25.70				49.85	29.26	20.81
	800	50.33	23.46	25.50				45.31	41.76	11.80
	900	49.53	25.66	24.06				43.54	44.55	9.61

cont.

Phase Composition

cont. 3

<u>Code</u>	<u>Temp</u>	<u>Austenite</u>		<u>Ferrite</u>		<u>Sigma</u>	
		<u>FeWt%</u>	<u>CrWt%</u>	<u>FeWt%</u>	<u>CrWt%</u>	<u>FeWt%</u>	<u>CrWt%</u>
1I	700	37.63	23.64	27.68	48.67		
4A	650	42.66	25.90	35.56	52.60		
	800	42.77	27.44	35.74	51.96		
	900	41.89	28.58	36.02	51.28		
4B	650	69.95	22.85	57.50	40.35		

TABLE 6

The effect of fourth element additions on the constitution of the experimental alloys, given as a change in the volume fraction of either delta ferrite or sigma phase.

IdentificationManganese Series

	<u>Mn Wt%</u>	<u>1050°C Vf</u>	<u>Phase</u>	<u>800°C Vf</u>	<u>Phase</u>
Mn0	0	0.20	δ	0.20	δ
Mn1	1.10	0.18	"	0.18	"
Mn3	2.95	0.15	"	0.19	(δ + σ)
Mn8	8.01	0.12	"	0.33	"

Copper Series

	<u>Cu Wt%</u>	<u>1050°C Vf</u>	<u>Phase</u>	<u>800°C Vf</u>	<u>Phase</u>
Cu0	0	0.20	δ	0.20	δ
Cu1	1.10	0.17	"	0.24	"
Cu2	2.12	0.19	"	0.25	δ + Cu
Cu7	7.50	0.15	"	0.20	"

Carbon Series

	<u>C Wt%</u>	<u>1050°C Vfδ</u>	<u>M₂₃C₆ Vf</u>	<u>800°C Vfδ</u>	<u>M₂₃C₆ Vf</u>
C0	0	0.35	0	0.44	0
C1	0.09	0.25	0.04	0.32	0.045
C2	0.13	0.20	0.05	0.30	0.055
C3	0.28	0.18	0.07	0.25	0.07

Nitrogen Series

	<u>N₂ Wt%</u>	<u>1050°C Vf</u>	<u>Phase</u>	<u>800°C Vf</u>	<u>Phase</u>
NO	0.004	0.17	δ	0.17	δ
N1	0.040	0.10	"	0.16	"
N2	0.068	0.08	"	0.15	"
N3	0.140	0.04	"	0.14	"

Silicon Series

	<u>Si Wt%</u>	<u>1050°C Vf</u>	<u>Phase</u>	<u>800°C Vf</u>	<u>Phase</u>
Si0	0	0.41	δ	0.40	σ
Si1	0.85	0.53	"	0.43	"
Si2	1.63	0.59	"	0.49	"
Si4	3.75	0.74	"	0.60	"

Molybdenum Series

	<u>Mo Wt%</u>	<u>1050°C Vf</u>	<u>Phase</u>	<u>800°C Vf</u>	<u>Phase</u>
Mo0	0	0.18	δ	0.22	σ
Mo1	0.92	0.18	"	0.25	"
Mo2	1.98	0.23	"	0.34	"
Mo4	3.74	0.23	"	0.47	"

cont. 2

<u>Identification</u>	<u>Niobium Series</u>				<u>Phase</u>
	<u>Nb Wt%</u>	<u>1050°C Vf</u>	<u>VfFe₂Nb</u>	<u>800°C Vf</u>	
Nb0	0	0.02	0	0.13	σ
Nb $\frac{1}{2}$	0.48	0.03	0	0.14	"
Nb1	1.06	0.06	Trace	0.17	"
Nb2	2.16	0.07	0.03	0.19	"

	<u>Titanium Series</u>				
	<u>Ti Wt%</u>	<u>1050°C Vf</u>	<u>Phase</u>	<u>800°C Vf</u>	<u>Phase</u>
Ti0	0	0.09	δ	0.16	σ
Ti $\frac{1}{4}$	0.34	0.10	"	0.16	"
Ti $\frac{1}{2}$	0.54	0.14	"	0.18	"
Ti1	1.05	0.16	"	0.26	"

The volume fractions are reported to an accuracy of \pm 3.1%

TABLE 7

The mass % of carbon, chromium and iron that was tied up as $M_{23}C_6$ in the carbon bearing alloy series.

	<u>Sample</u>	<u>VfM₂₃₋₆C</u>	<u>Wt%M₂₃₋₆C</u>	<u>Wt%C</u>	<u>Wt%Fe</u>	<u>Wt%Cr</u>
0.09wt%C	1050°C	0.04	3.26	0.179	0.278	2.79
	800°C	0.045	3.68	0.206	0.320	3.15
0.13wt%C	1050°C	0.05	4.09	0.229	0.356	3.50
	800°C	0.055	4.50	0.252	0.392	3.85
0.28wt%C	1050°C	0.063	5.16	0.289	0.449	4.42
	800°C	0.070	5.70	0.319	0.496	4.88

TABLE 8

The micro-analysis results of selected quaternary alloys showing the partitioning of the fourth element additions between the austenite and delta ferrite phases.

Manganese Series

<u>1F1050°C + 1%Mn</u>	<u>Fe Wt%</u>	<u>Cr Wt%</u>	<u>Ni Wt%</u>	<u>Mn Wt%</u>	<u>PARTITIONING PARAMETER (P)</u>
Austenite	35.66	33.82	29.02	1.49	1.21
Ferrite	30.12	55.82	12.81	1.23	
<u>1F1050°C + 3%Mn</u>					
Austenite	34.96	33.09	28.33	3.60	1.40
Ferrite	29.67	55.48	12.26	2.58	
<u>1F1050°C + 8%Mn</u>					
Austenite	33.22	31.43	26.45	8.91	1.49
Ferrite	28.52	54.12	11.34	5.97	

Copper Series1F1050°C + 1%Cu

Austenite
Ferrite

Results obtained not analysable

1F1050°C + 2%Cu

Austenite
Ferrite

35.23 32.32 30.02 2.41
29.52 55.50 14.28 0.75

Cu Wt%

3.21

1F1050°C + 7%Cu

Austenite
Ferrite

32.54 30.52 28.63 8.29
28.03 58.76 12.02 1.99

4.17

Silicon Series1A1050°C + 1%Si

Austenite
Ferrite

57.50 25.65 16.75 1.03
53.67 36.88 9.12 1.05

Si Wt%

0.98

1A1050°C + 2%Si

Austenite
Ferrite

56.40 25.23 16.35 2.01
52.90 35.46 9.36 2.28

0.88

1A1050°C + 4%Si

Austenite
Ferrite

54.55 24.97 17.25 3.17
51.88 33.68 10.88 3.56

0.89

TABLE 9

Comparing the prediction of the onset of sigma phase or delta ferrite formation by the method due to (i) Pauling and (ii) Hume Rothery. The third values termed (**V**) uses electron vacancy concepts due to Pauling but have developed the individual element values using band theory.

Austenite/(Austenite + Sigma Phase) Boundary

<u>Alloy</u>	<u>Temp.</u>	<u>Atomic Concentration</u>			<u>Nv</u>	<u>e/a</u>	<u>V</u>
		<u>Fe</u>	<u>Cr</u>	<u>Ni</u>			
1	900°C	0.65	0.24	0.12	2.92	7.84	3.45
2	"	0.59	0.27	0.16	2.93	7.94	3.45
3	"	0.50	0.27	0.24	2.74	8.02	3.37
4	"	0.41	0.31	0.28	2.70	7.94	3.30
1	800°C	0.69	0.22	0.14	2.92	7.64	3.40
2	"	0.64	0.22	0.21	2.82	7.84	3.40
3	"	0.55	0.23	0.24	2.62	7.88	3.32
4	"	0.50	0.26	0.28	2.69	7.96	3.33
1	650°C	0.75	0.20	0.05	2.96	7.70	3.46
2	"	0.69	0.20	0.11	2.84	7.82	3.42
3	"	0.50	0.24	0.26	2.61	8.04	3.32
4	"	0.42	0.28	0.30	2.60	8.04	3.29

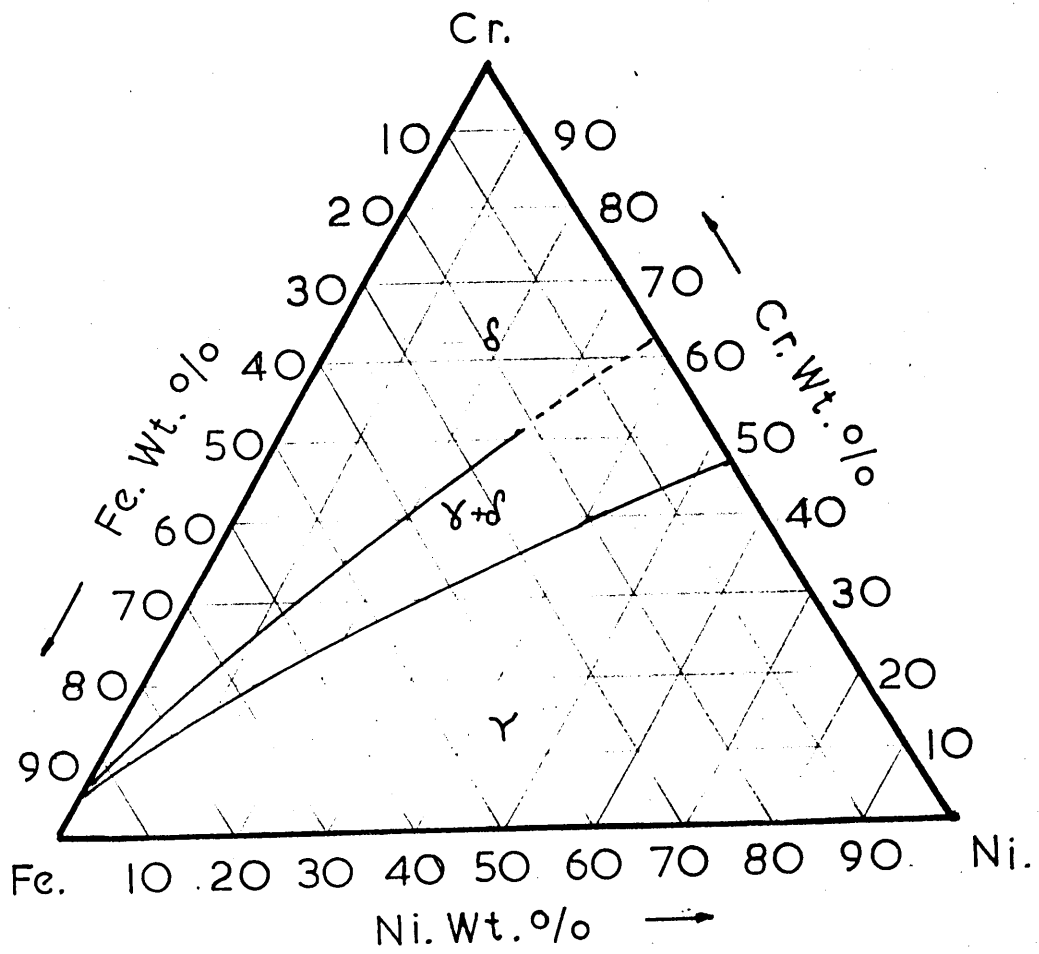
Austenite/(Austenite + Alpha Ferrite) Boundary

1	900°C	0.89	0.11	-	2.88	7.78	3.49
2	"	0.81	0.16	0.03	2.92	7.74	3.47
3	"	0.71	0.21	0.08	2.92	7.74	3.43
4	"	0.65	0.24	0.12	2.93	7.84	3.45
1	800°C	0.96	-	0.04	2.58	8.08	3.48
2	"	0.91	0.06	0.04	2.72	7.94	3.48
3	"	0.85	0.11	0.04	2.80	7.86	3.47
4	"	0.78	0.16	0.06	2.86	7.80	3.44
1	650°C	0.86	-	0.14	2.38	8.28	3.42
2	"	0.83	0.06	0.11	2.56	8.10	3.43
3	"	0.81	0.11	0.08	2.71	7.94	3.44
4	"	0.78	0.16	0.06	2.86	7.80	3.44

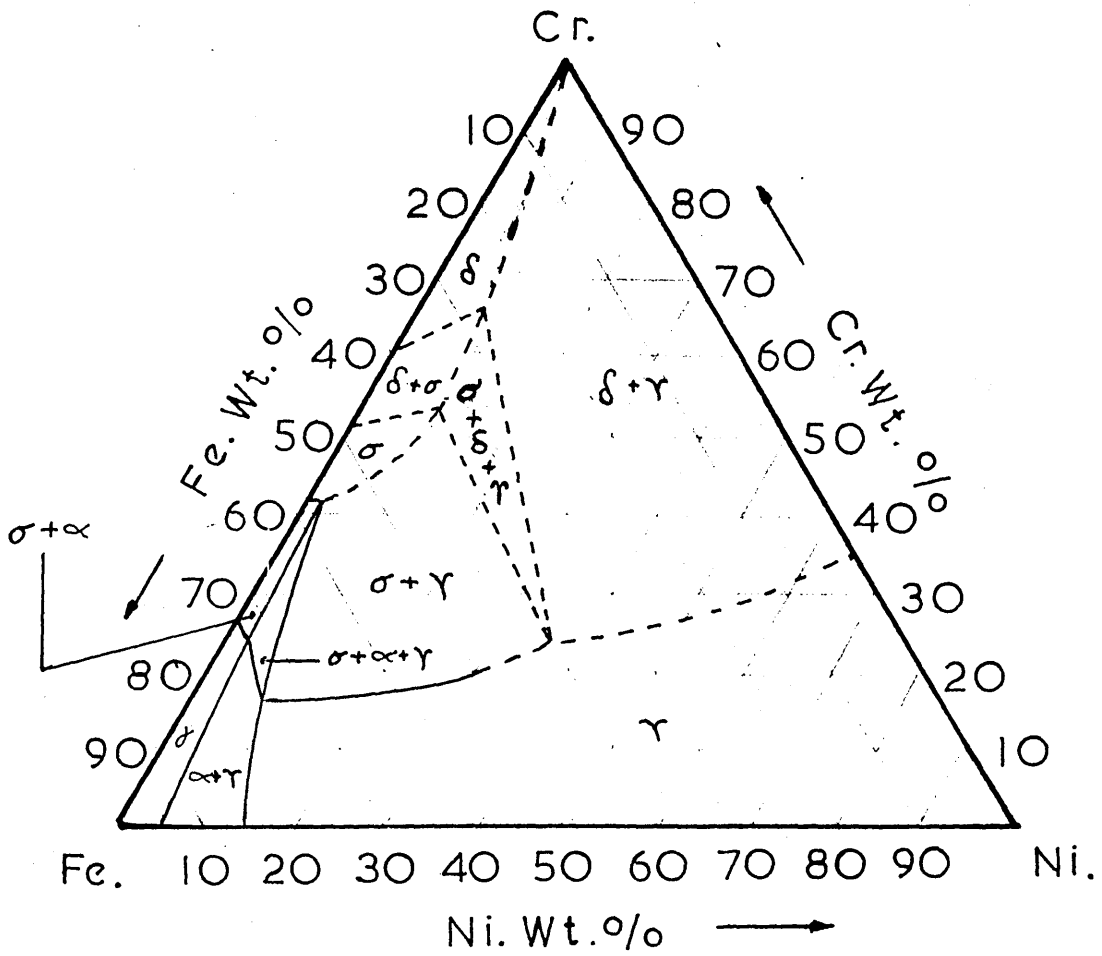
Fig. 1

Shows the general form of the isothermal sections of the Fe-Cr-Ni system. Fig. 1(a) represents the system at 1300°C, Fig. 1(b) at 650°C whilst Fig. 1(c) is a detail of the (austenite + sigma phase) region at 800°C.

(a) 1300°C Cr.-Fe.-Ni. Isotherm



(b) 650°C Cr-Fe-Ni Isotherm



(c) Phase Boundaries At 800°C

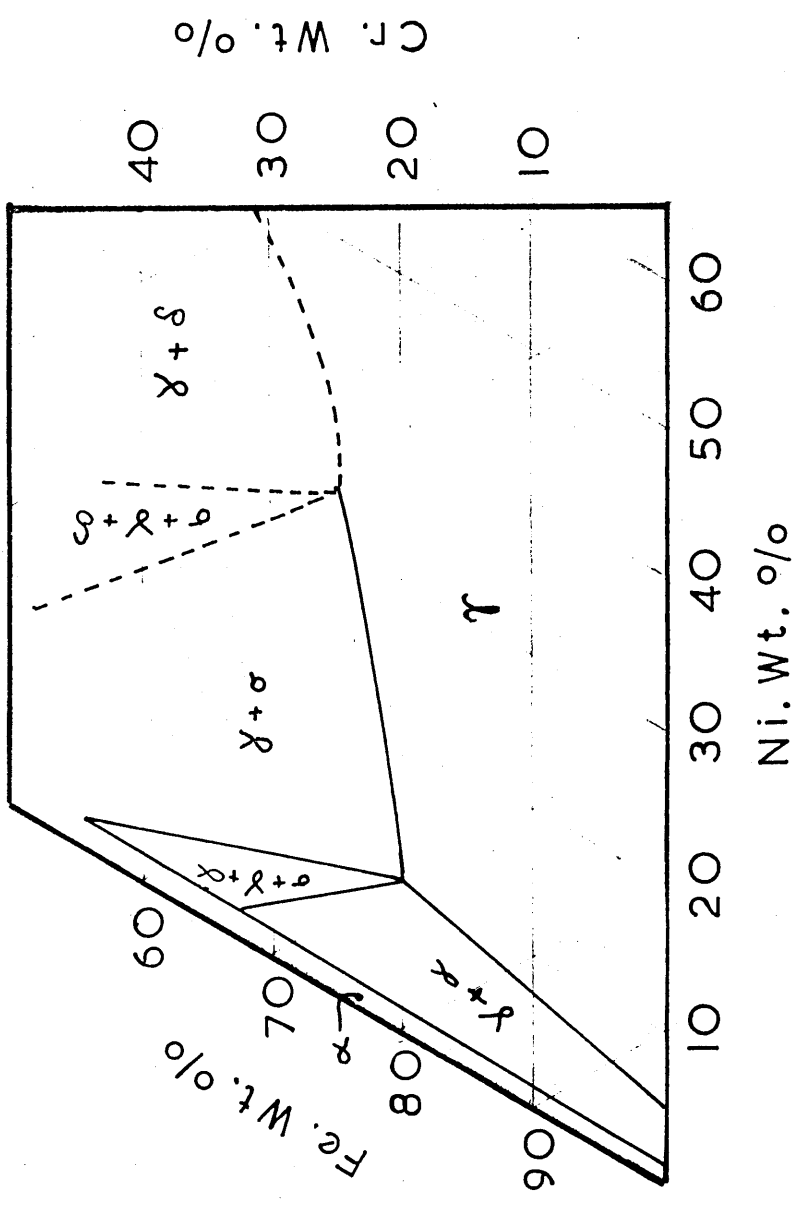
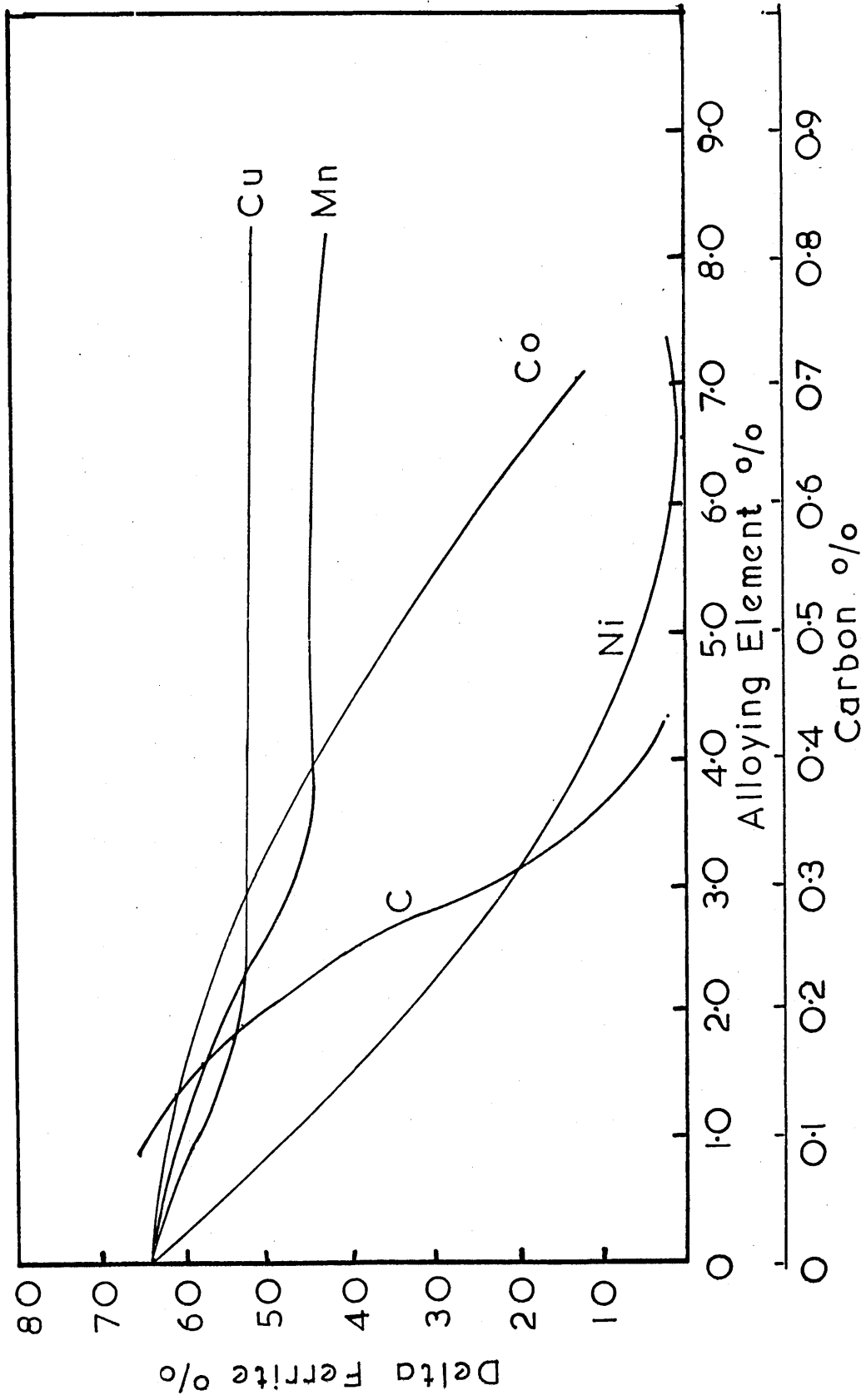


Fig. 2

(a) shows the effect of alloying additions on the delta ferrite content of a (17Cr-0.1C) steel equilibrated at 1050°C.

(b) The effect of alloying additions on the delta ferrite content of a (17Cr-4Ni-0.1C) steel equilibrated at 1050°C.

(a) Solution Treated At 1050°C



(b)
Solution Treated At 1050°C

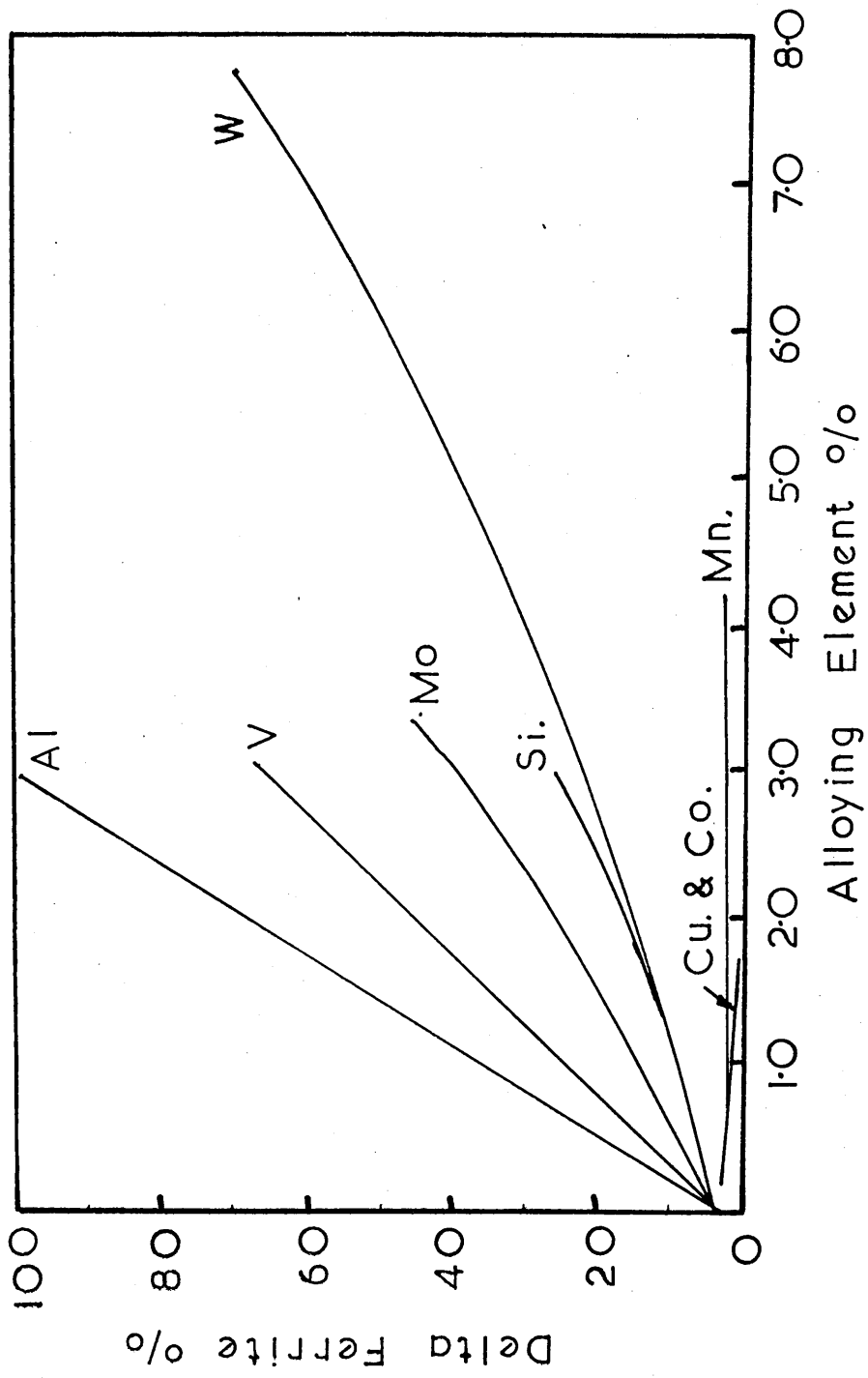


Fig. 3

(a) shows the Schaeffler Diagram⁽²⁰⁾ used for predicting the % delta ferrite content from a knowledge of the nickel and chromium equivalent values.

(b) Is the modified Schaeffler Diagram according to De Long⁽²¹⁾

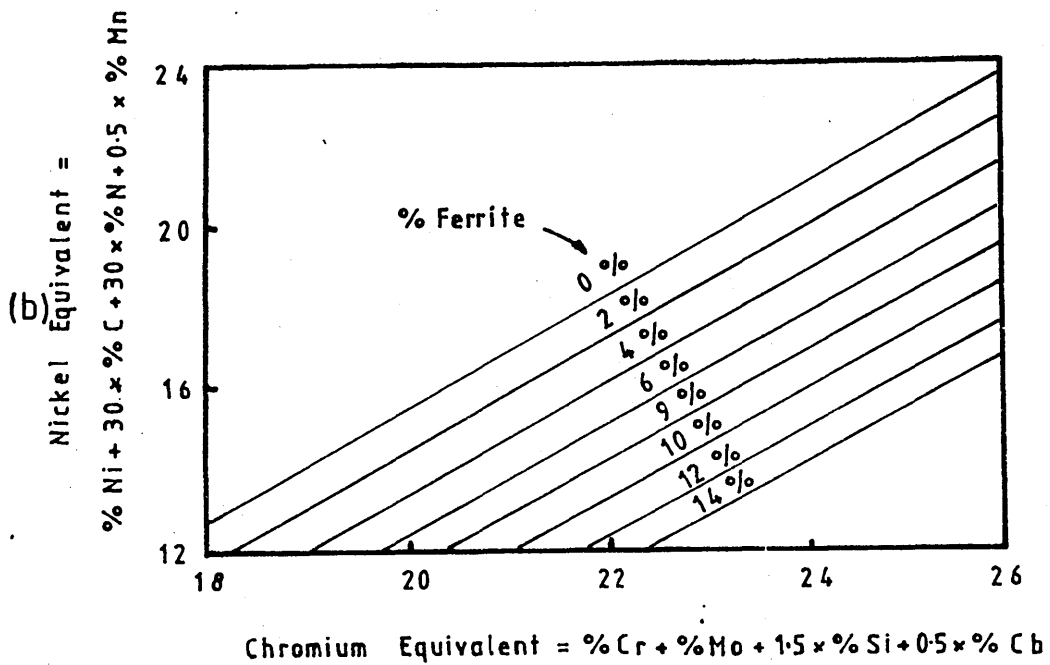
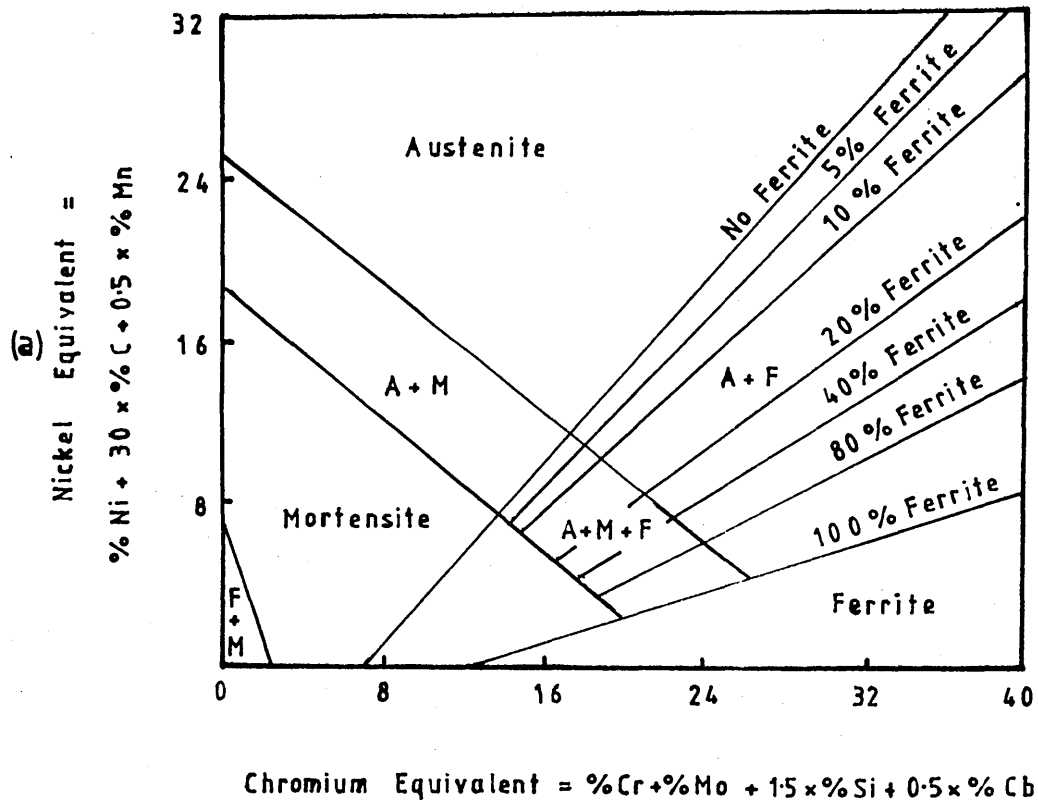


Fig. 4

Shows a "C" curve for the formation of sigma phase in a duplex stainless steel after Beckett⁽³⁹⁾.

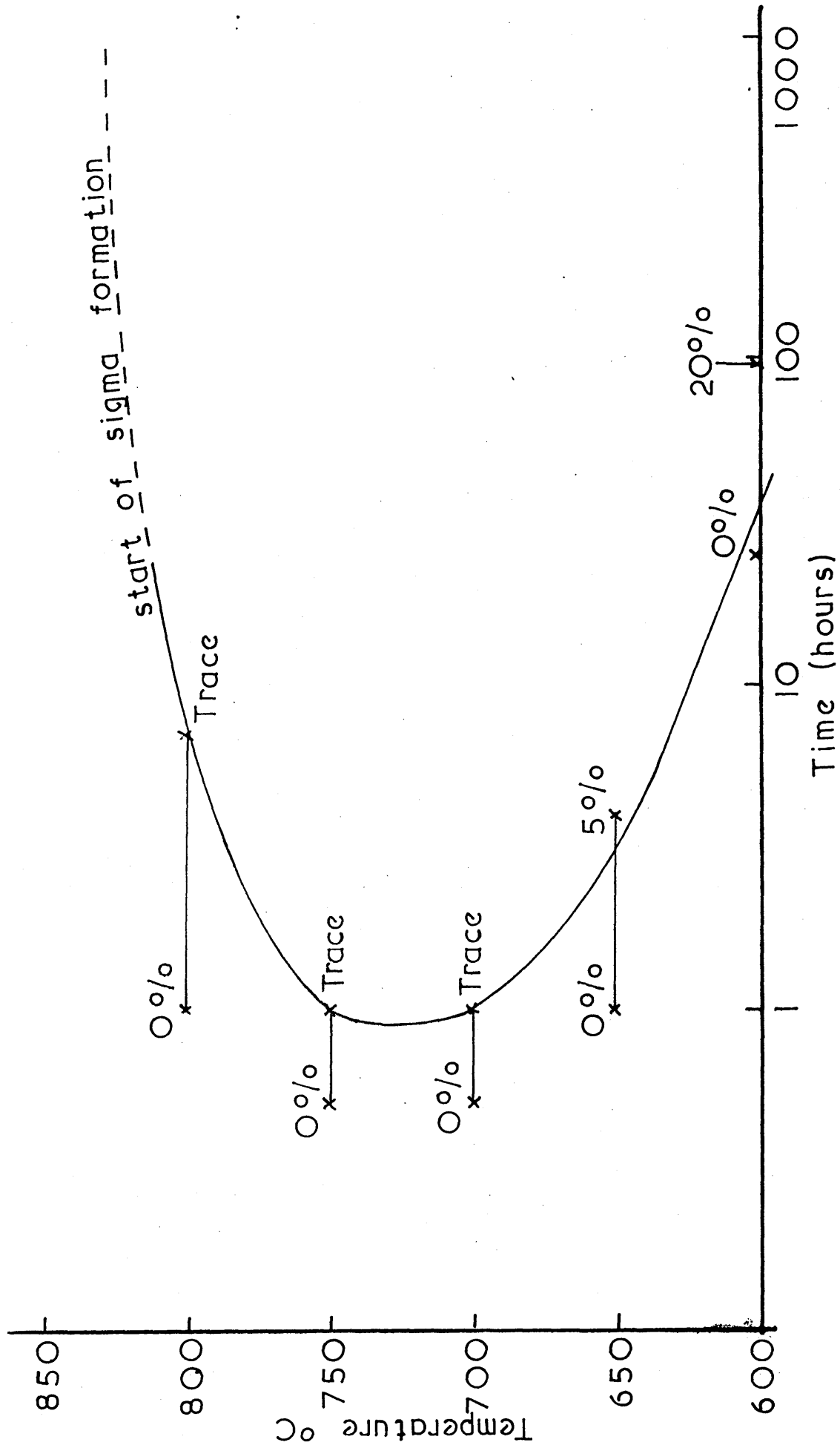


Fig. 5

Shows the effect of irradiation temperature and cold working
on the void swelling properties of an austenitic stainless steel. (60)

(Neutrons, dose = 44 d.p.a.)

Fig. 6

Shows the percentage swelling with increasing dose for annealed
and cold worked austenitic stainless steels. (60)

(Neutrons)

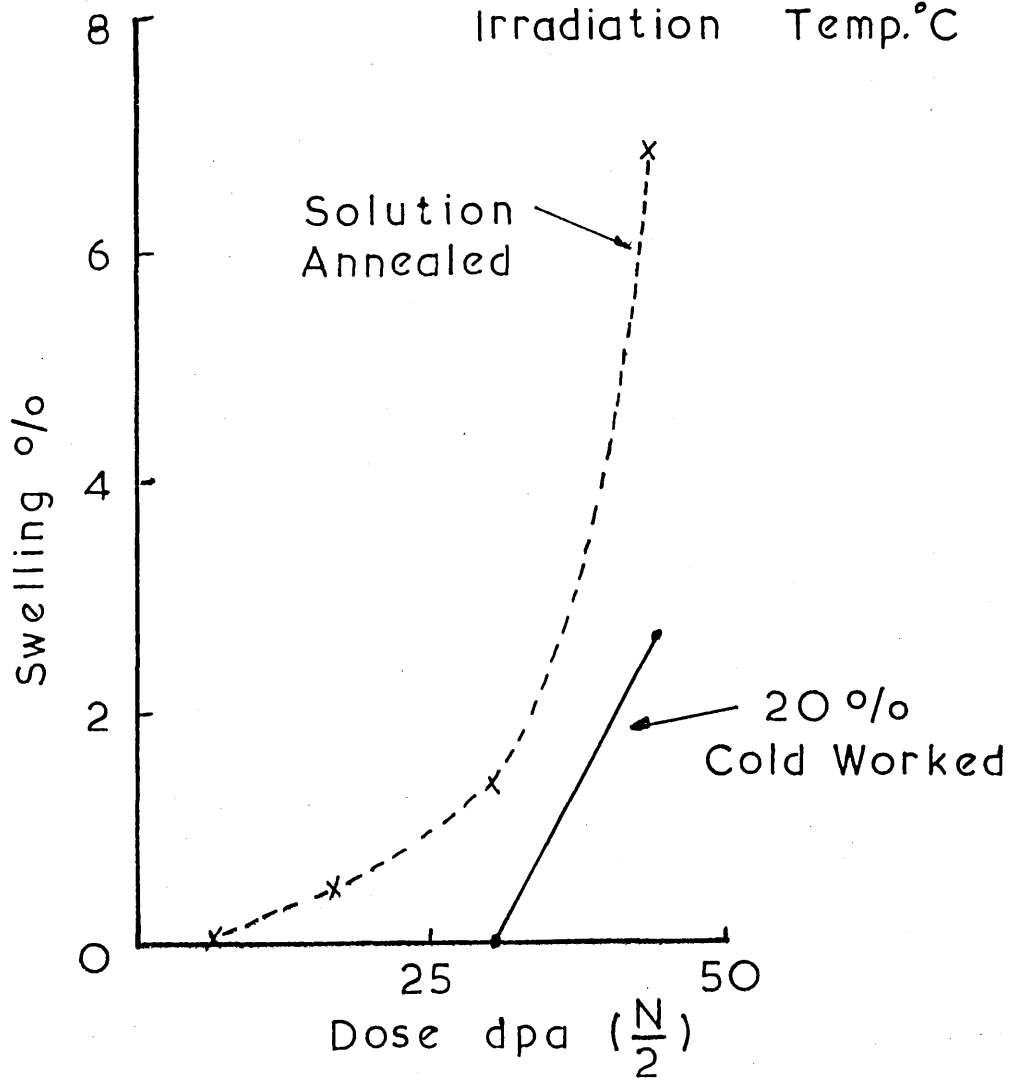
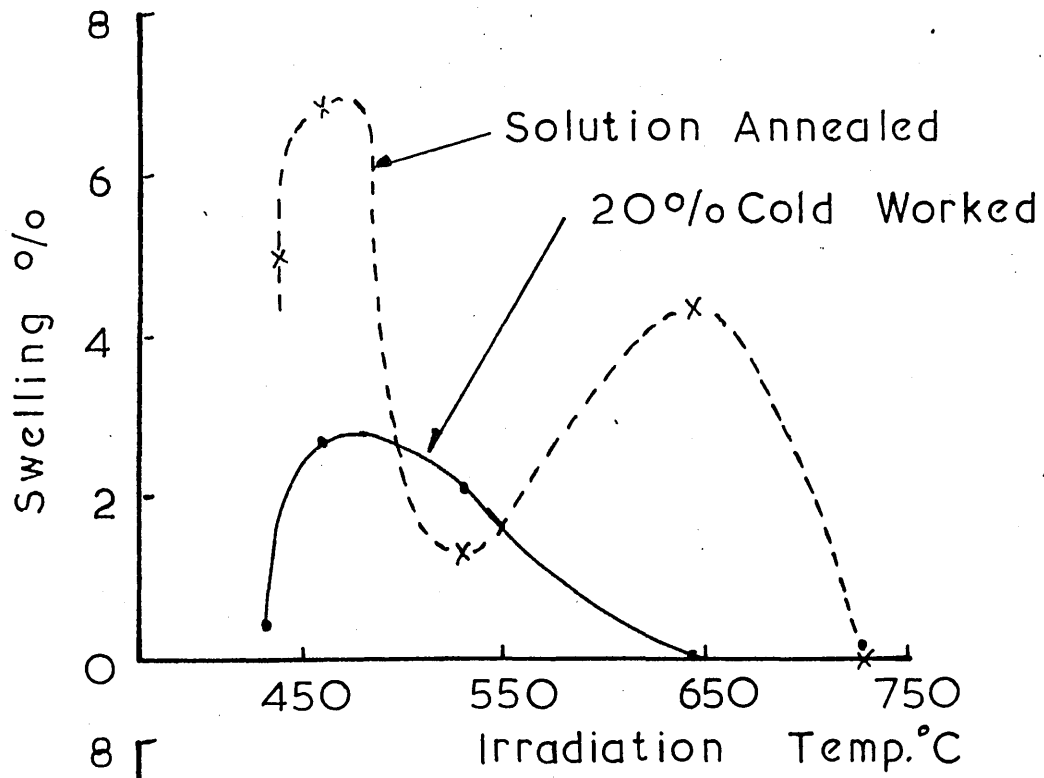


Fig..7

Shows the percentage void swelling as a function of nickel equivalent and also indicates the typical phases found in stainless steels with the nickel equivalents given.

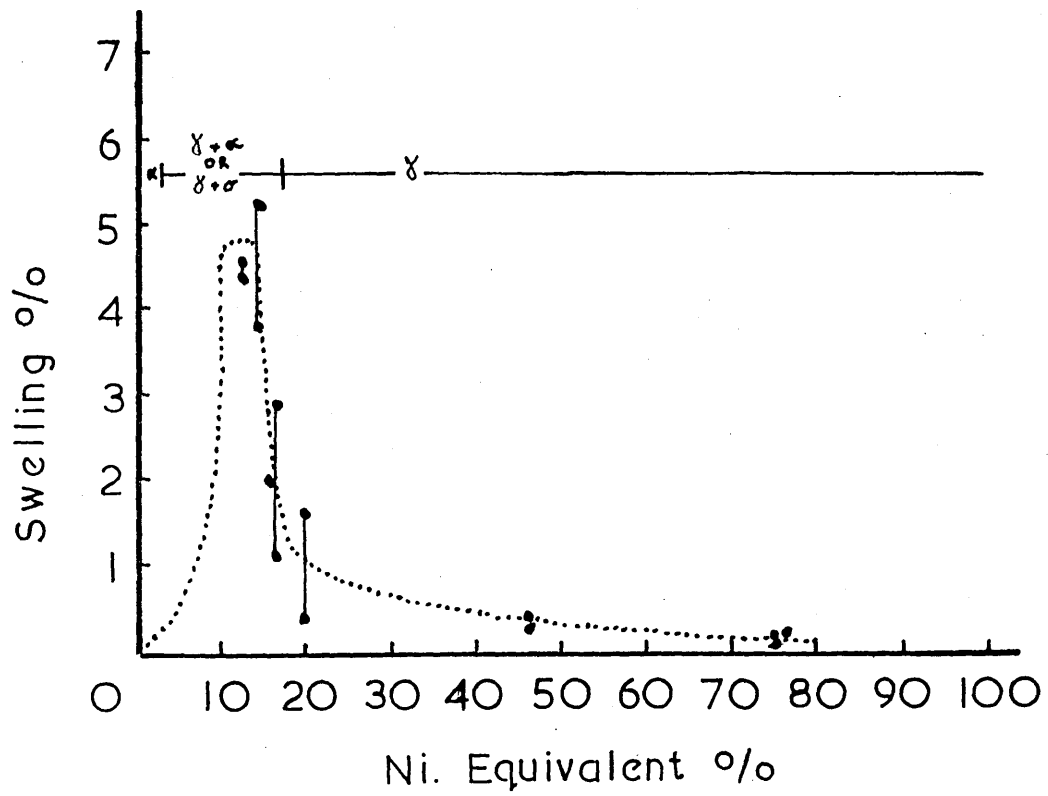


Fig. 8

Shows the calculated isothermal section of the Fe-Cr-Ni system at 450°C. Superimposed are a selection of commercial alloys given in the table with the alloys swelling percent at 450°C after 40 d.p.a. indicated in brackets.

() % SWELLING
 AT 40dpa / 450°C

- A M316 (4.3)
- B FV548 (1.5)
- C 321 (0.9)
- D 347 (1.4)
- E G68 (2.3)
- F 316 (2.1)
- G 316L (5.7)
- H PE16 (CAST 1)
(1.6)
- I PE16 (CAST 2)
(2.0)
- J PE16 (CAST 3)
(2.6)
- K PE16 MATRIX
(0.8)

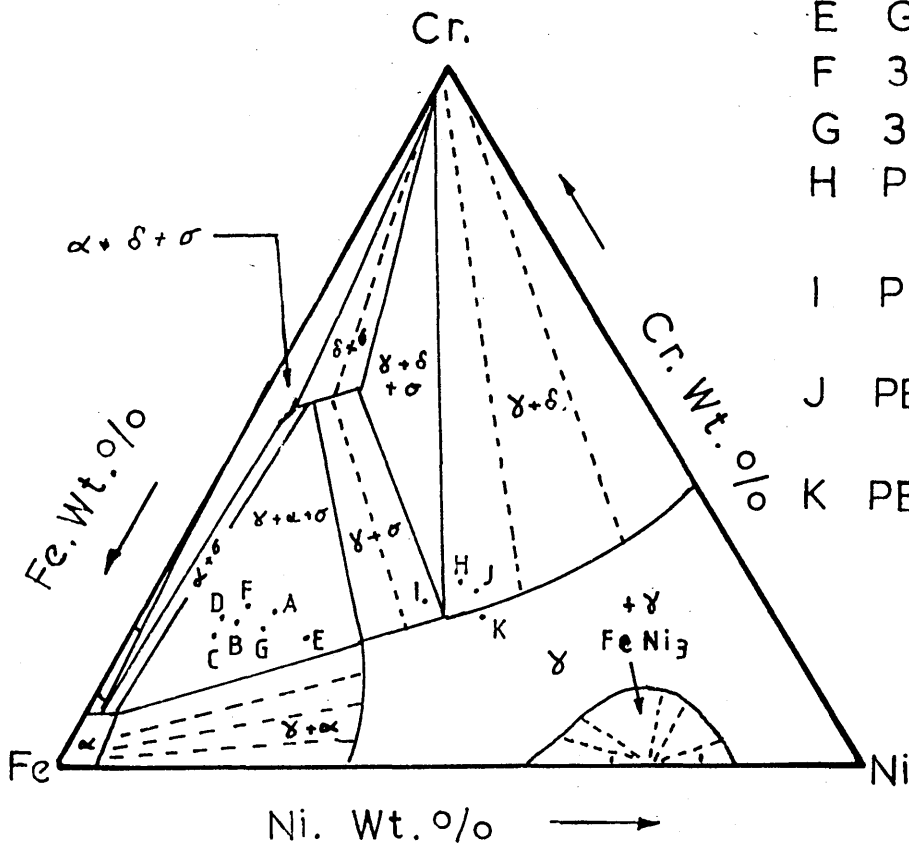
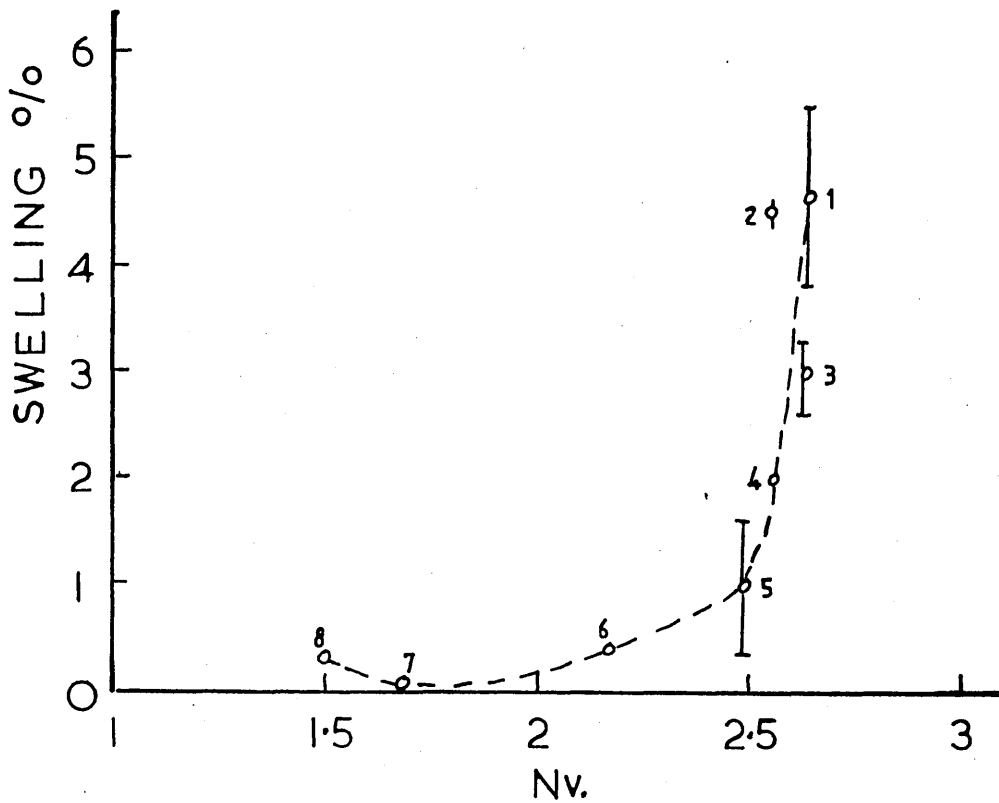


Fig. 9

Shows the relationship between electron vacancy number (N_v) and percentage swelling for the alloys shown. A sharp inflection occurs when N_v is ~ 2.5 which agrees well with the predicted onset of sigma phase when N_v becomes greater than 2.52 as given in ref (37).



46.5 MeV. Ni.⁶⁺ IONS 40dpa 600°-625°C

- 1 316 Austenitic Steel
- 2 321 Austenitic Steel
- 3 M316 Austenitic Steel
- 4 FV548 Austenitic Steel
- 5 12R72H^V Austenitic Steel
- 6 NIMONIC PE 16 ALLOY
- 7 NIMONIC 80A ALLOY
- 8 NIMONIC 75 ALLOY

Fig. 10

The shape of the modified copper hearth used for the manufacture of the high purity quaternary alloys.

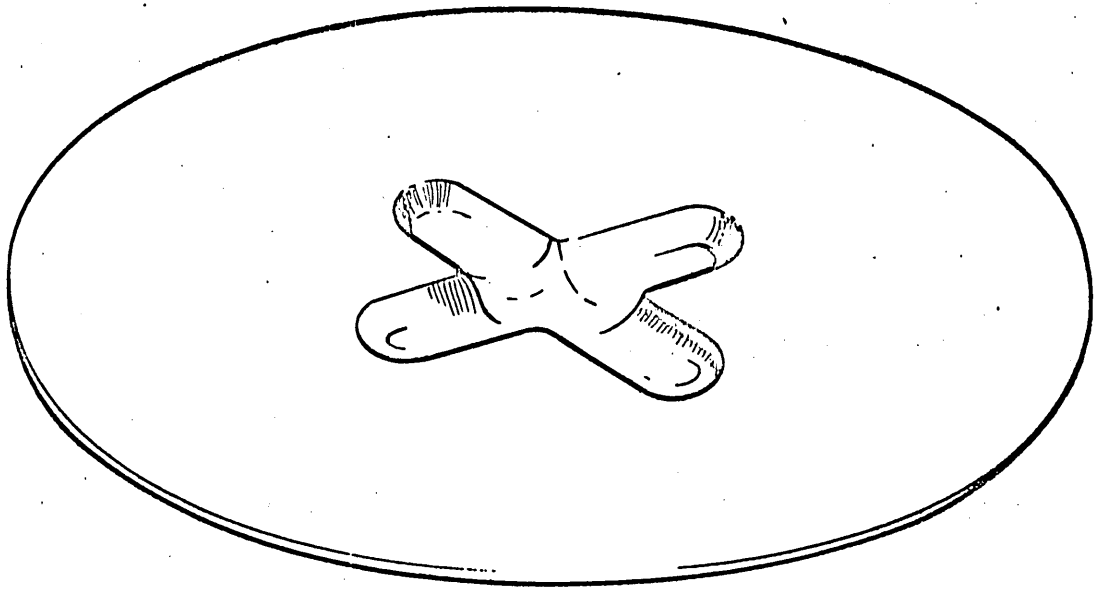


Fig. 11

The scanning electron microscope holder showing the central hole for the specimen and the peripheral holes for element standards.

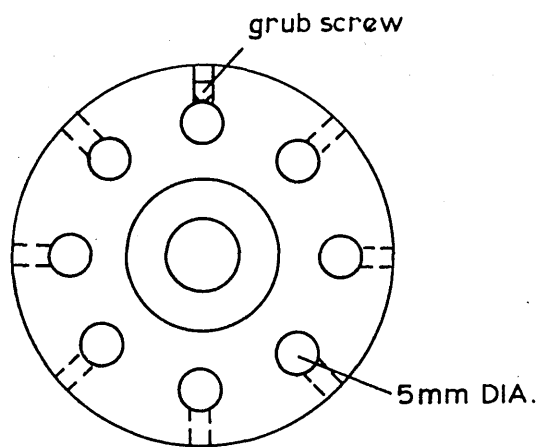
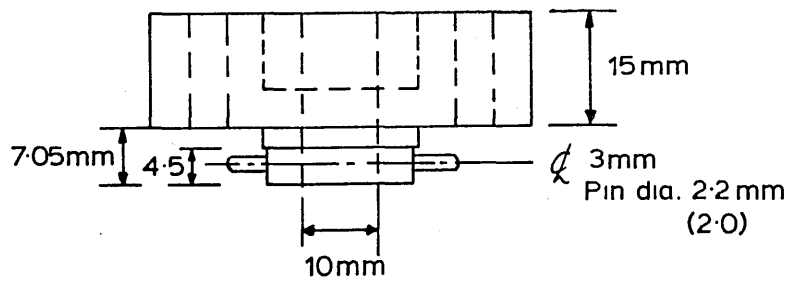
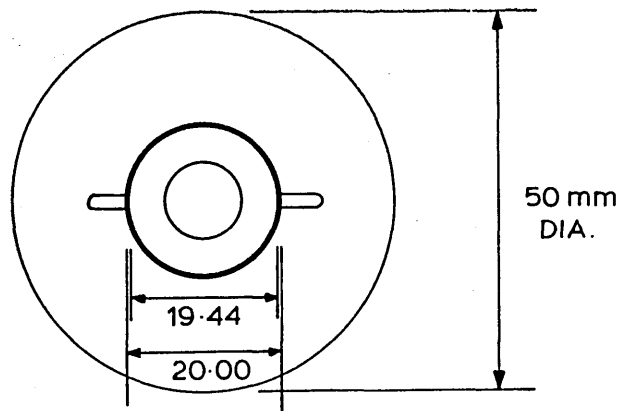
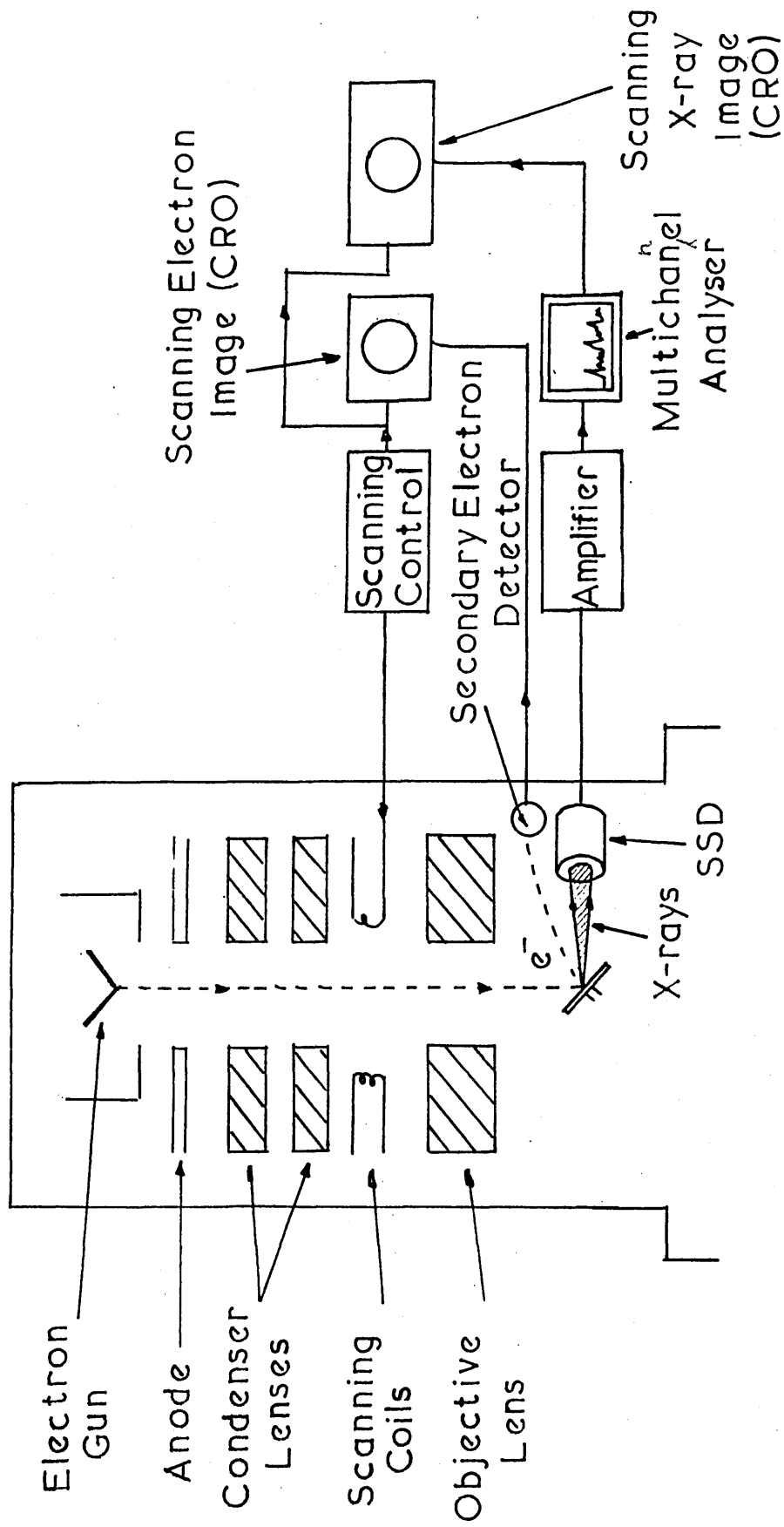


Fig. 12

A schematic diagram of the scanning electron microscope with the energy dispersive X-Ray analysis attachment shown.



X ray Microanalysis in the Electron Microscope

Fig. 13

A comparison of the results determined on the Sheffield City Polytechnic Philips PSEM 500 and ZAF corrected using the N.B.S. FRAME 3 computer programme with those determined using the fully quantitative PSEM 500 located at the Steetley Company.

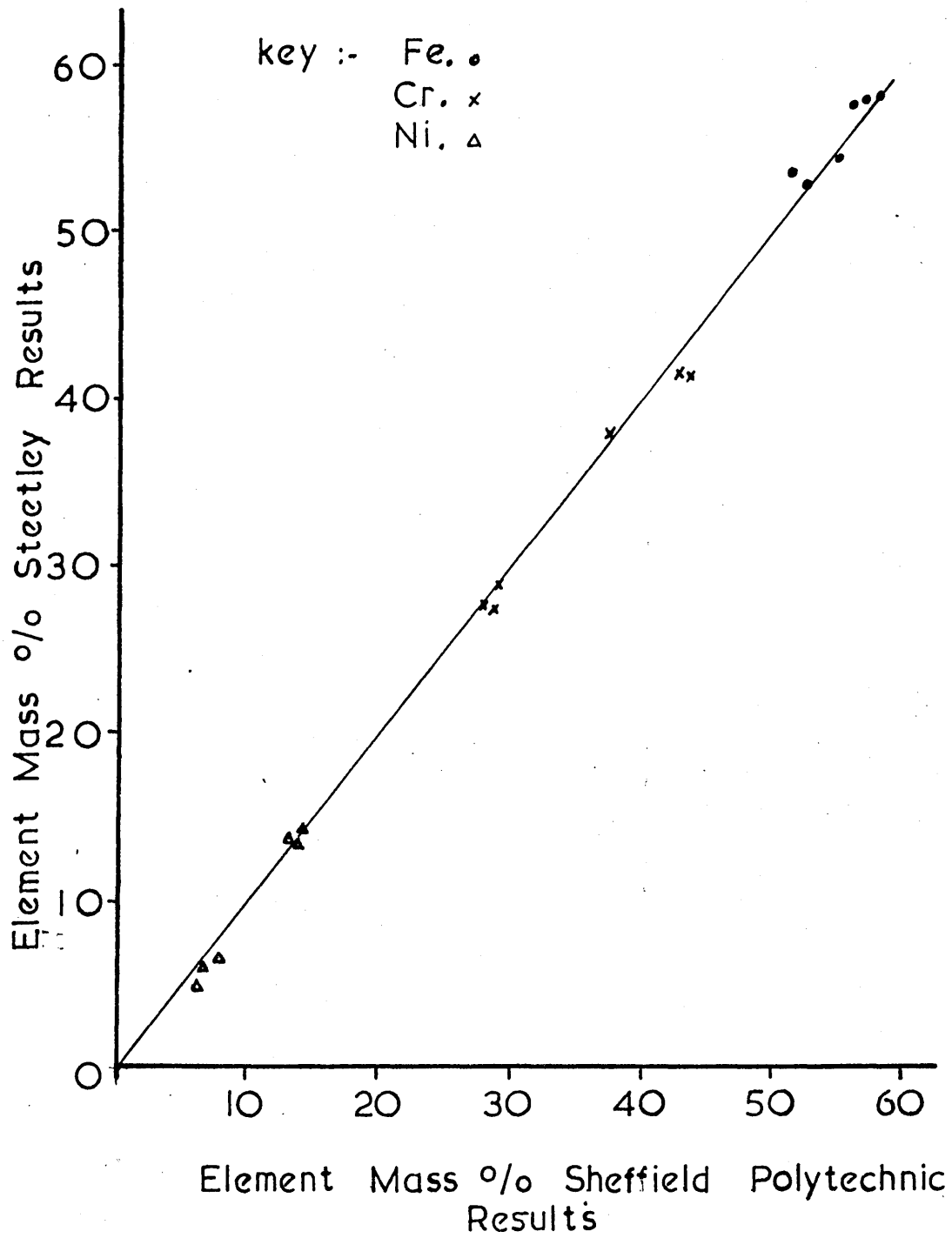


Fig 14

Shows the equilibrated microstructure of alloy 1B(27Cr-16Ni) at the heattreatment temperatures given. This alloy lies in the (austenite + delta ferrite) field at 950°C and above and in the (austenite + sigma phase) field at 900°C and below. The darker phase is delta ferrite or sigma phase whilst the lighter phase is austenite.

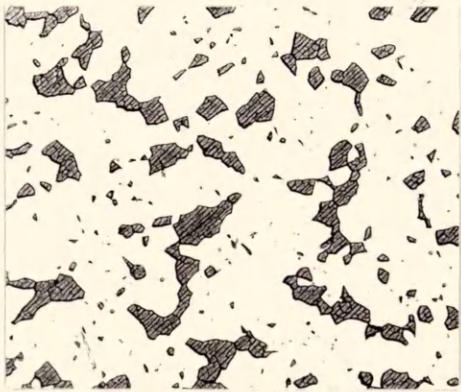
Etchant 10N. K OH Electrolytic at ~4V

- (a) 1150°C
- (b) 1050°C
- (c) 950°C
- (d) 900°C
- (e) 800°C
- (f) 700°C
- (g) 650°C



a

X450



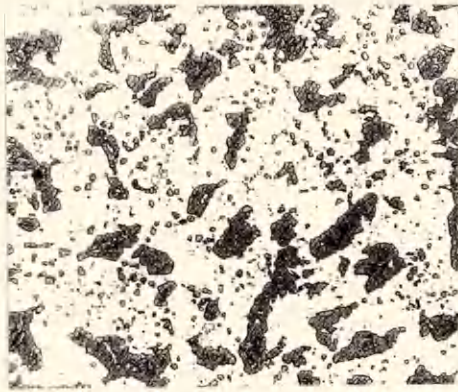
b

X450



c

X450



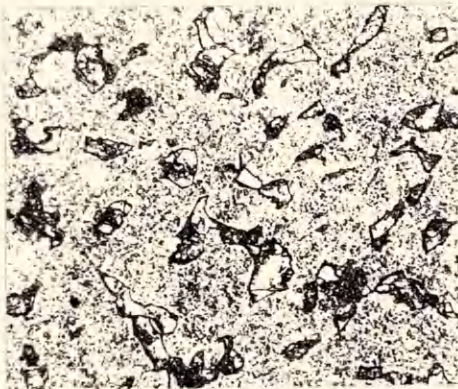
d

X450



e

X450



f

X450



g

X450

Fig 15

Shows the equilibrated microstructures of alloy 3A(18Cr-2Ni) at the heattreatment temperatures given. At 1150°C the alloys are entirely ferritic as illustrated in (a) but precipitates significant amounts of austenite at heattreatment temperatures. The two phase microstructure of austenite + delta ferrite persists down to 650°C. The delta ferrite phase is continuous whilst the austenite is discrete islands enclosed by dark lines indicating the tendency of oxalic acid to preferentially etch the austenite/delta ferrite grain boundaries.

Etchant 10% Oxalic acid, Electrolytic at ~ 4V.

(a) 1150°C

(b) 1050°C

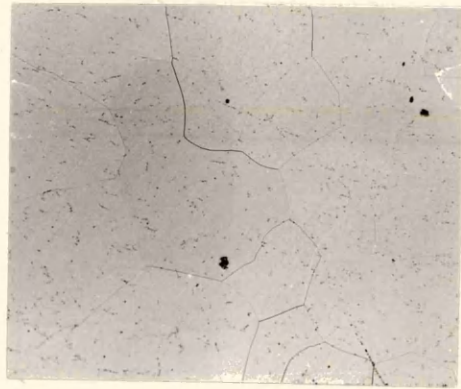
(c) 950°C

(d) 900°C

(e) 800°C

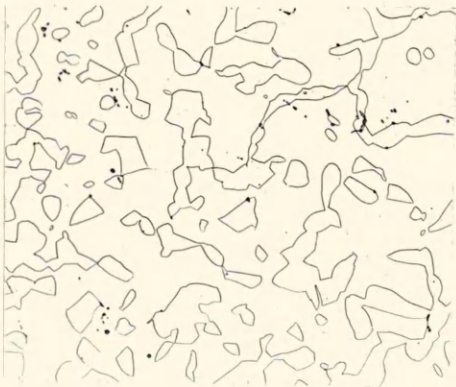
(f) 700°C

(g) 650°C



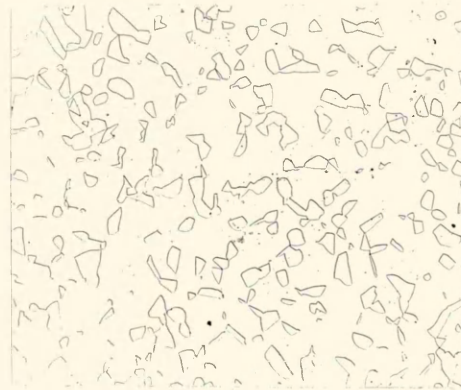
a

x 50



b

x100



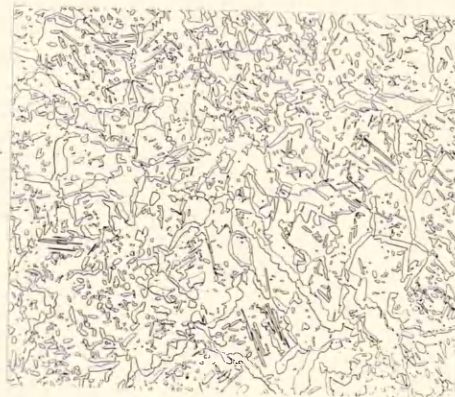
c

x 50



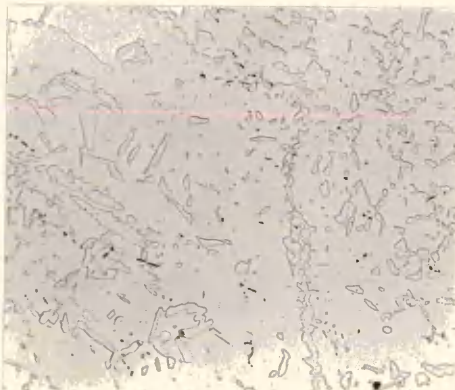
d

x100



e

x100



f

x100



g

x100

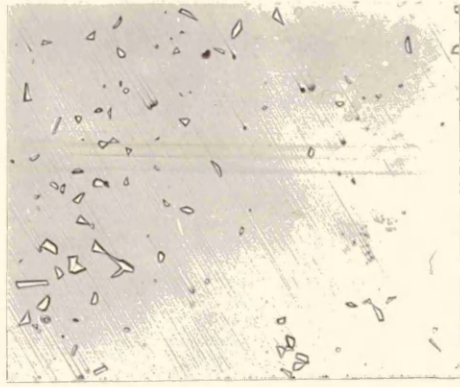
Fig 16

Showing the equilibrated microstructure of alloy 3B(18Cr-7Ni)

This alloy is predominantly austenitic at temperatures from 800°C to 1150°C. At 650°C the microstructure is three phase comprising of (austenite + ferrite + sigma phase)

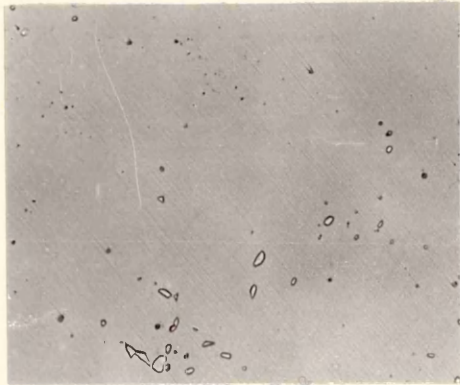
Etchant 10% Oxalic acid, Electrolytic at ~ 4V

- (a) 1150°C
- (b) 1050°C
- (c) 950°C
- (d) 900°C
- (e) 800°C
- (f) 700°C
- (g) 650°C



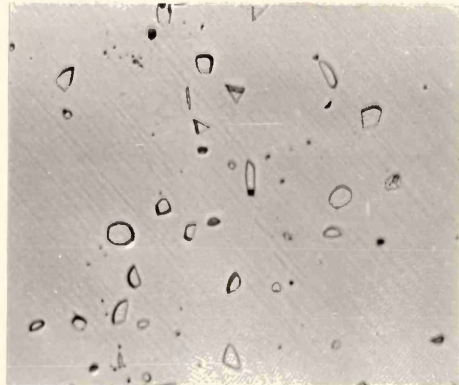
a

x200



b

x200



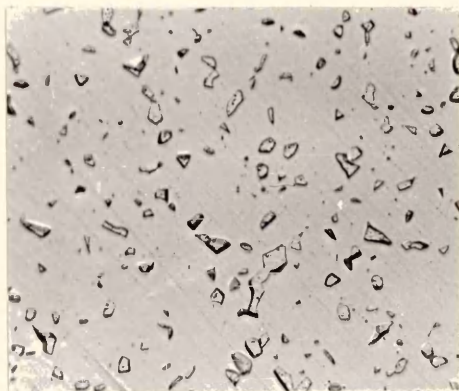
c

x450



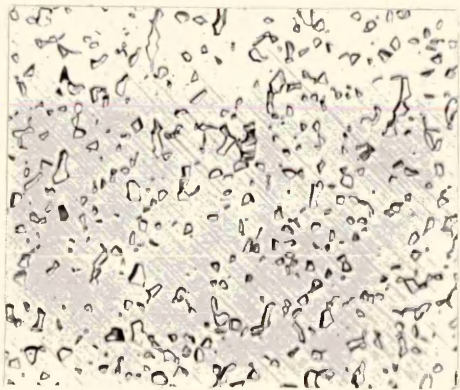
d

x450



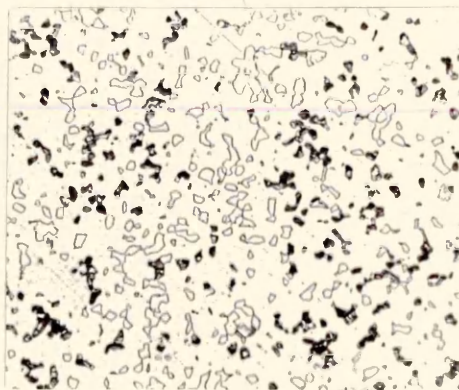
e

x450



d

x450



f

x450

Fig 17

Transmission Electron Micrographs of 1B(27Cr-16Ni) after heattreatment at 800°C showing the austenite phase in (a) and sigma phase in (b) and (c).

Polished at ambient temperature in 6% perchloric acid in acetic acid.



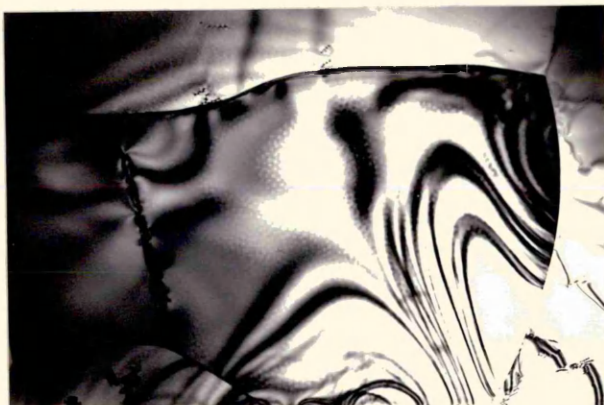
a

x50K



b

x70K



c

x30K

Fig 18

Transmission Electron Micrographs of 1B(27Cr-16Ni) after heattreatment at 650°C. The micrograph at (a) shows the fineness of the microstructures developed at 650°C. Micrograph (b) shows an aggregate of sigma phase and (c) an unrecrystallised grain of delta ferrite.

Polished at ambient temperature in 6% perchloric acid in acetic acid.



a

x5K



b

x25K



c

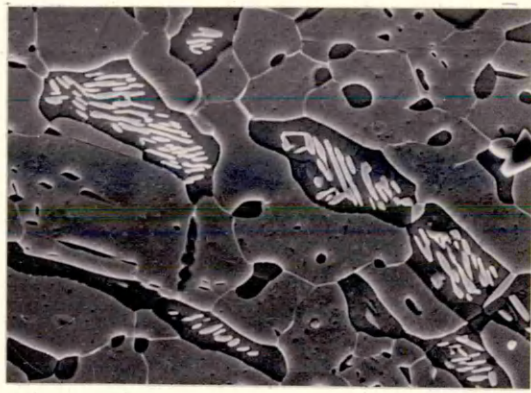
x35K

Fig 19

Scanning Electron Microscopy of alloy 1F(35Cr-28Ni),
showing the cellular structure of (austenite + delta ferrite)
which was evident at temperatures of 900°C and below.

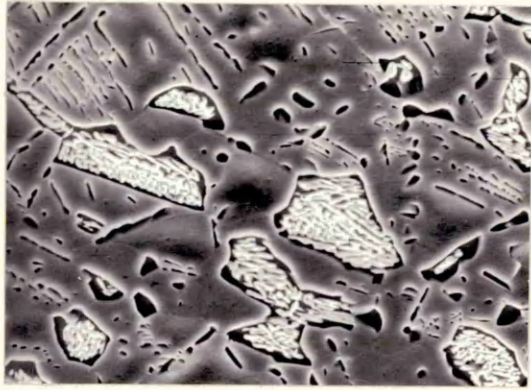
Etchant 10% v/vo Oxalic acid, Electrolytic at ~ 4V

- (a) 900°C
- (b) 800°C
- (c) 700°C
- (d) 650°C



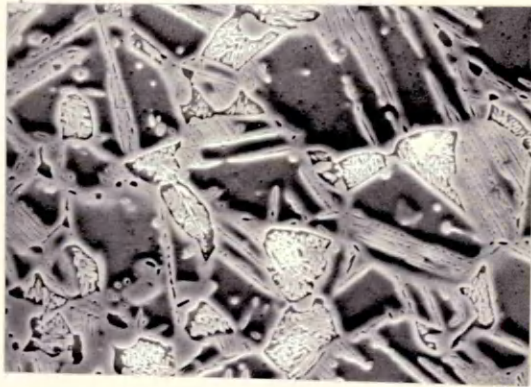
a

x1500



b

x1500



c

x1500



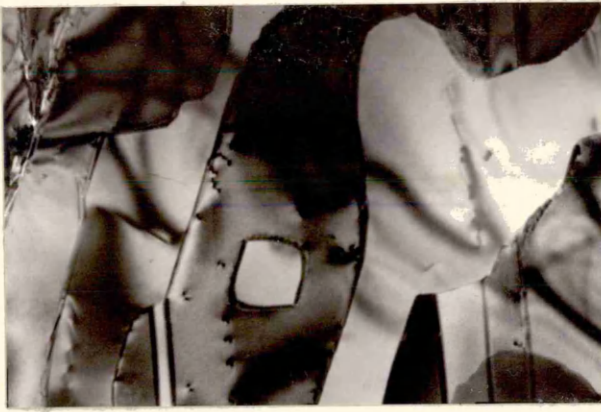
f

x1500

Fig 20

Transmission Electron Microscopy of the cellular structure developed in alloy 1F(35Cr-28Ni) at 800°C. Micrograph (a) is in bright field, whilst (b) and (c) are dark field images of delta ferrite and austenite respectively. The diffraction pattern at (d) was consistent with the stereographic projection of the orientation relationship presented in Fig 21.

Polished in 6% perchloric acid in acetic acid.



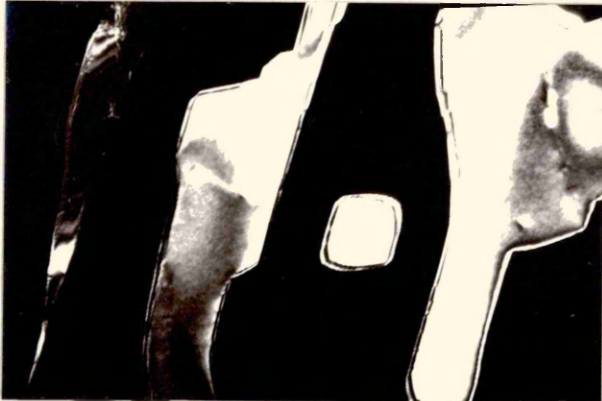
a

x 66K



b

x 66K



c

x 66K



d

Fig 21

The stereographic projection of the orientation relationship between austenite and delta ferrite due to Kurdjumov Sachs.

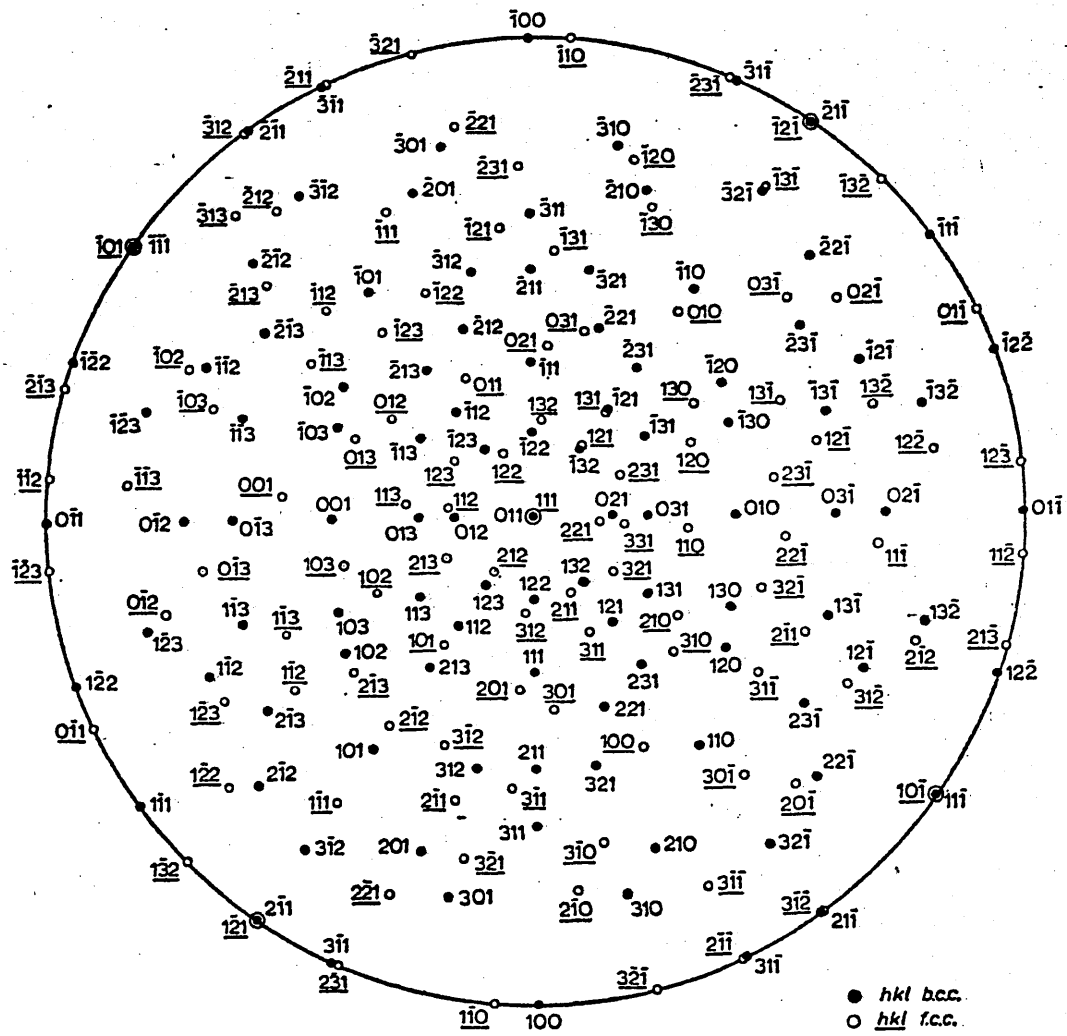


Fig 22

Shows the microstructure of alloys 4A(45Cr-17Ni), (a), (b) and (c) and 4B(32Cr-3Ni), (d), which were designed to fall within the three phase fields of ($\gamma + \delta + \sigma$) that lie to either side of the two phase ($\gamma + \sigma$) phase field at temperatures below 900°C.

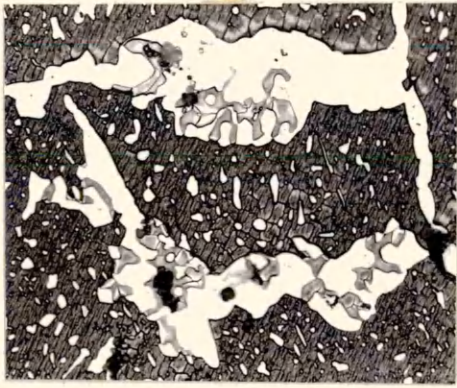
Etchant 10N. K OH Electrolytic at $\sim 4V$

(a) 900°C

(b) 800°C

(c) 700°C

(d) 650°C



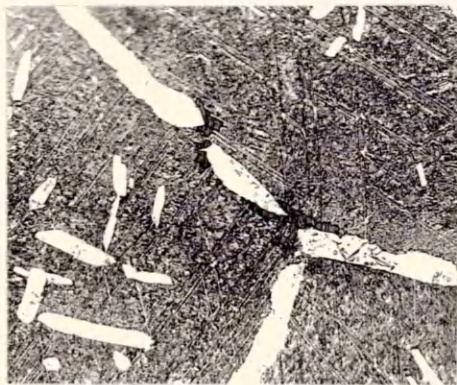
a

x450



b

x450



c

x450



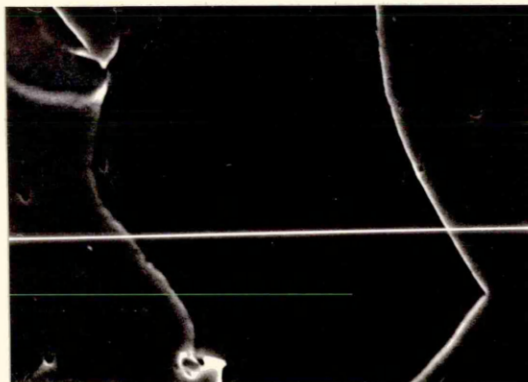
d

x450

Fig 23

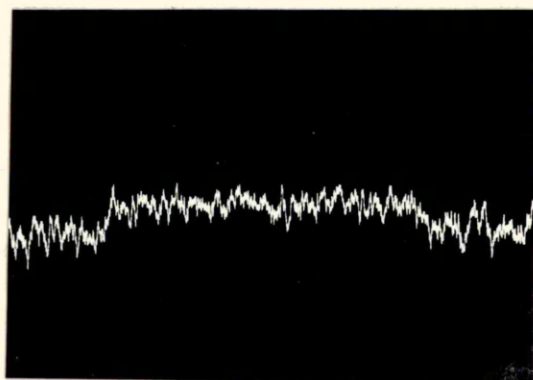
Indicates the element line scans for iron,(b), chromium,(c) and nickel,(d), across an austenite grain bounded by delta ferrite (a). The scans were produced on an S.E.M., the sample being lightly etched with 10% oxalic acid.

Electrolytic at $\sim 4V$.



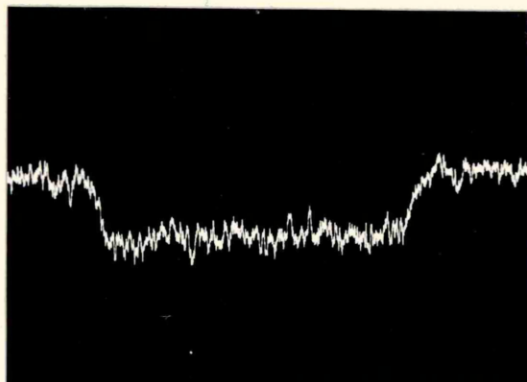
a

x1500



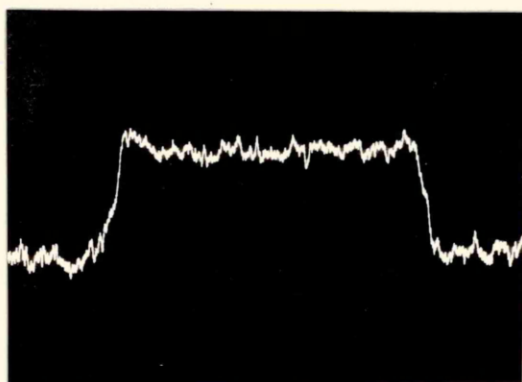
b

Fe SCAN



c

Cr SCAN



d

Ni SCAN

Fig. 24

A comparison of the change in austenite content with the change in nickel content of the precipitating austenite phase as the transformation proceeds at 800°C.

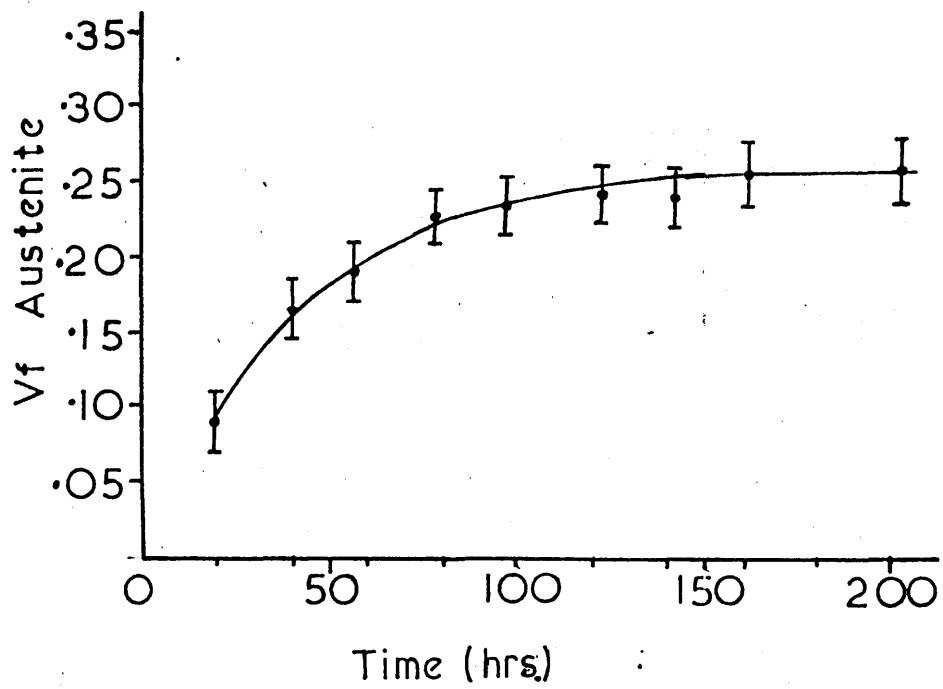
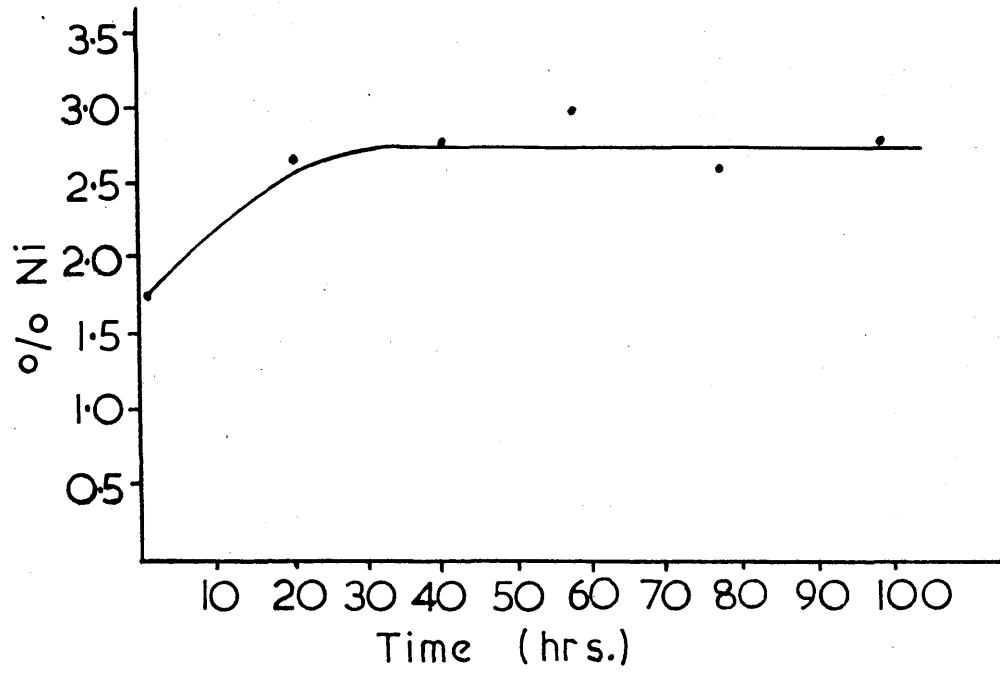


FIG 25

1150 °C Fe.Cr.Ni, Isothermal
Section

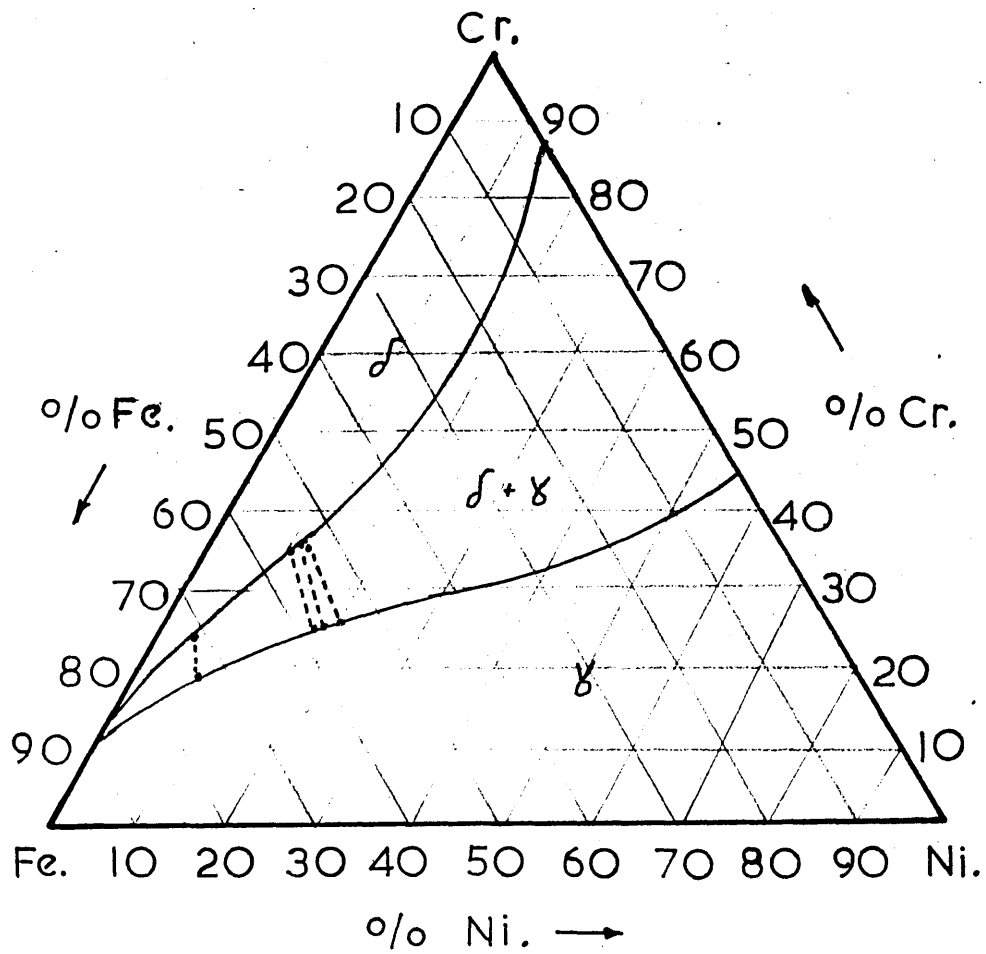


FIG 26

1050 °C Fe.-Cr.-Ni. Isotherm

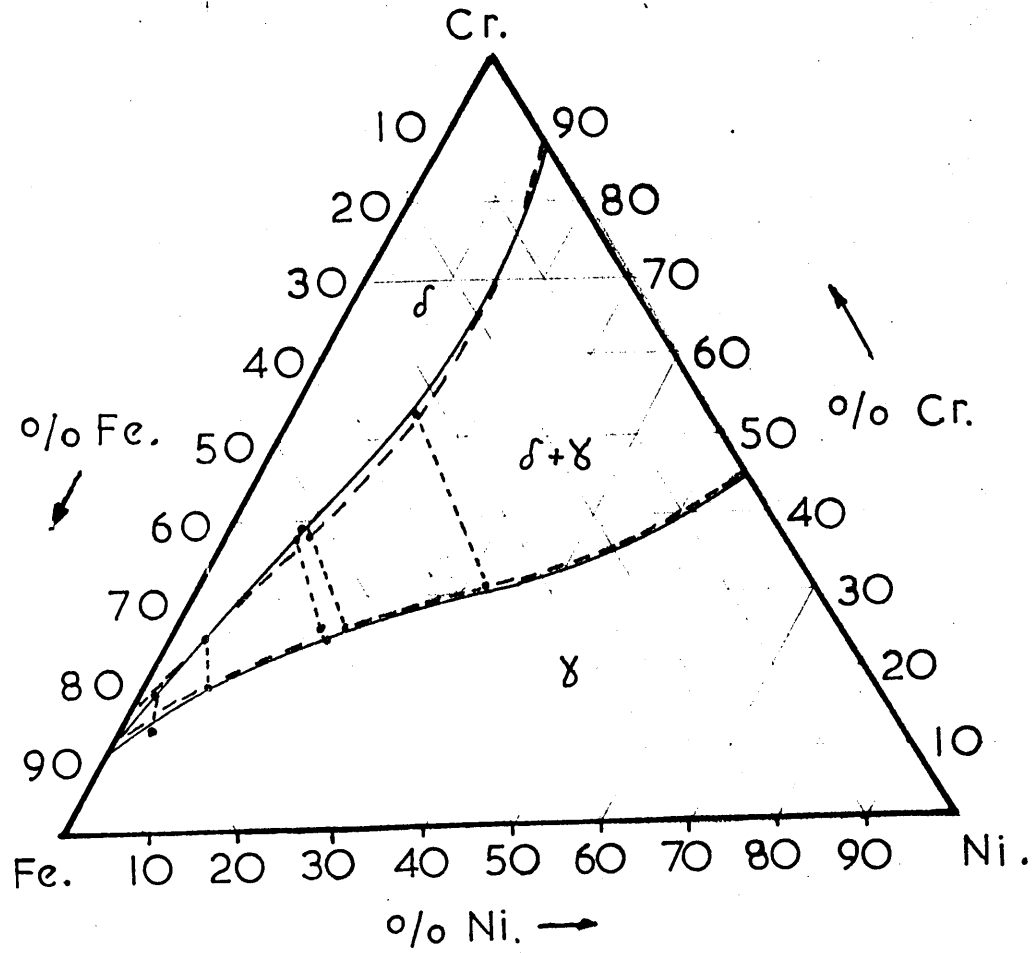


FIG 27

950 °C Fe.-Cr.-Ni. Isotherm

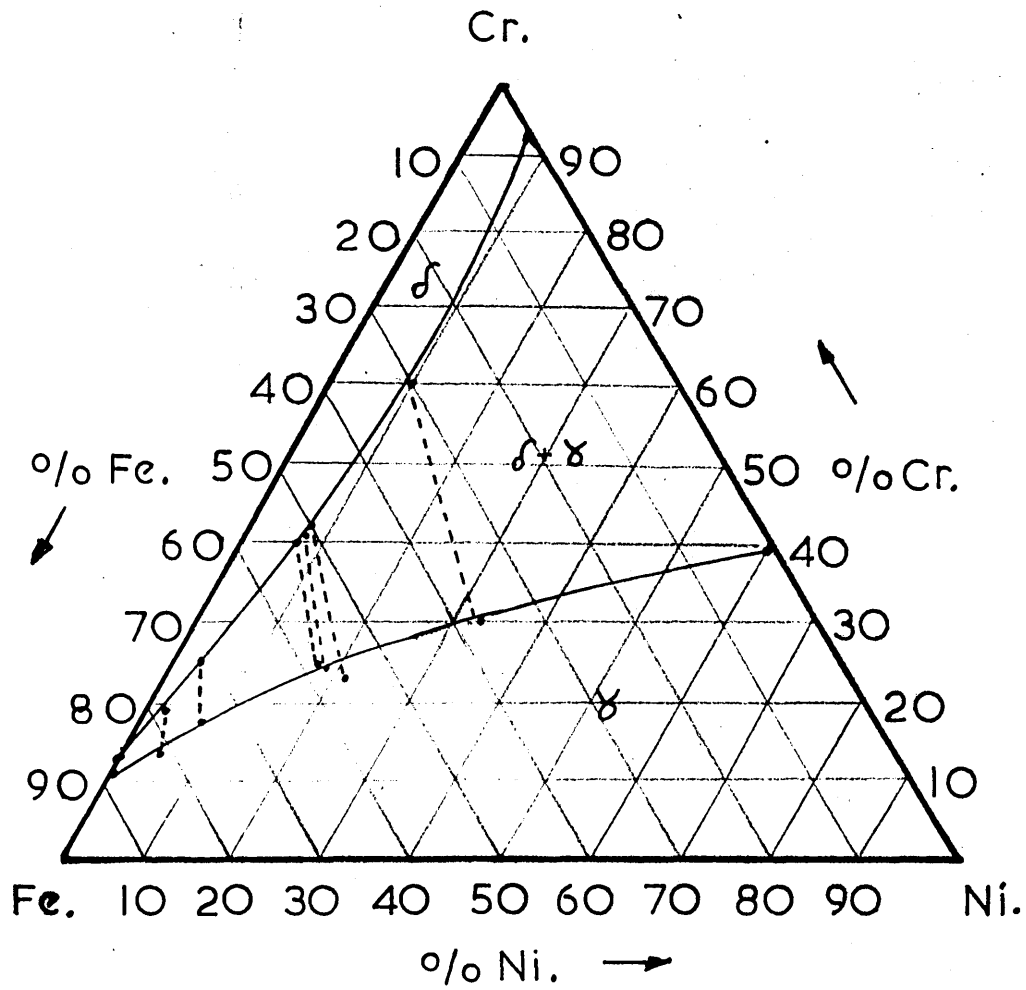
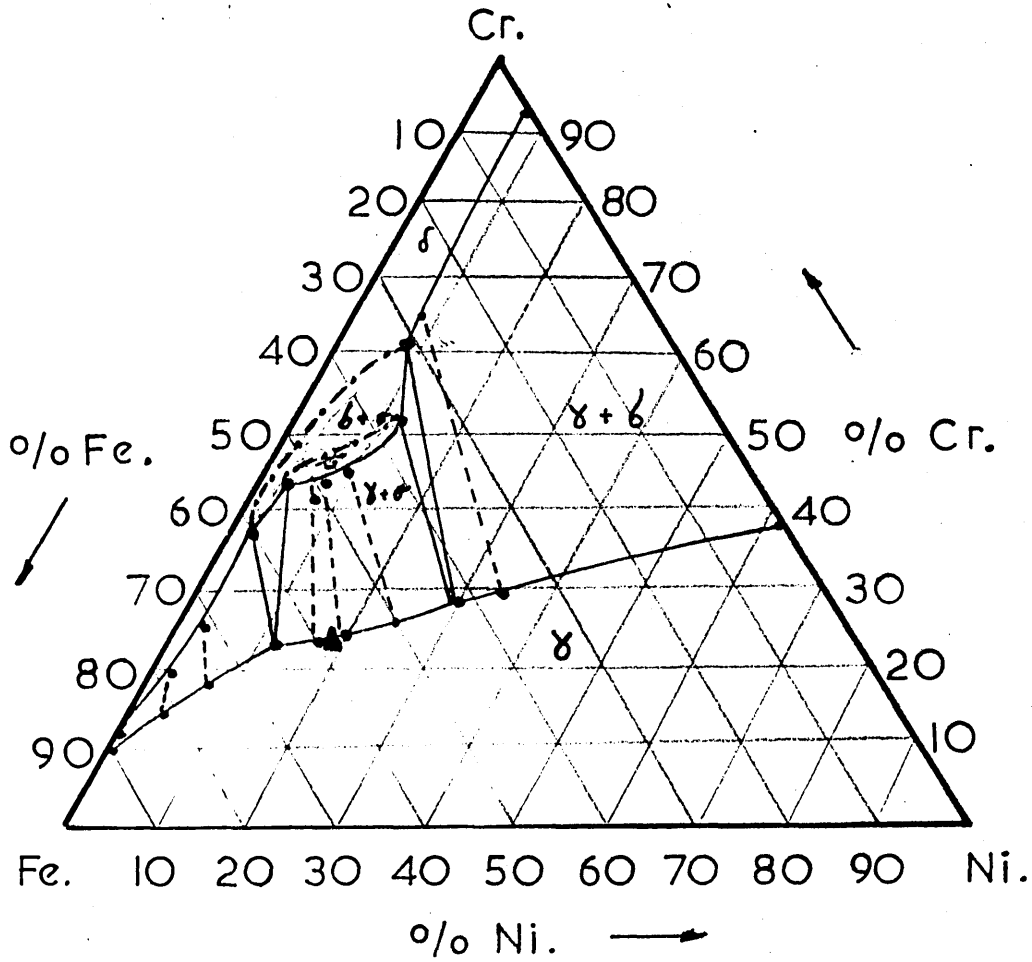


FIG 28

900°C Fe-Cr-Ni. Isothermal Section



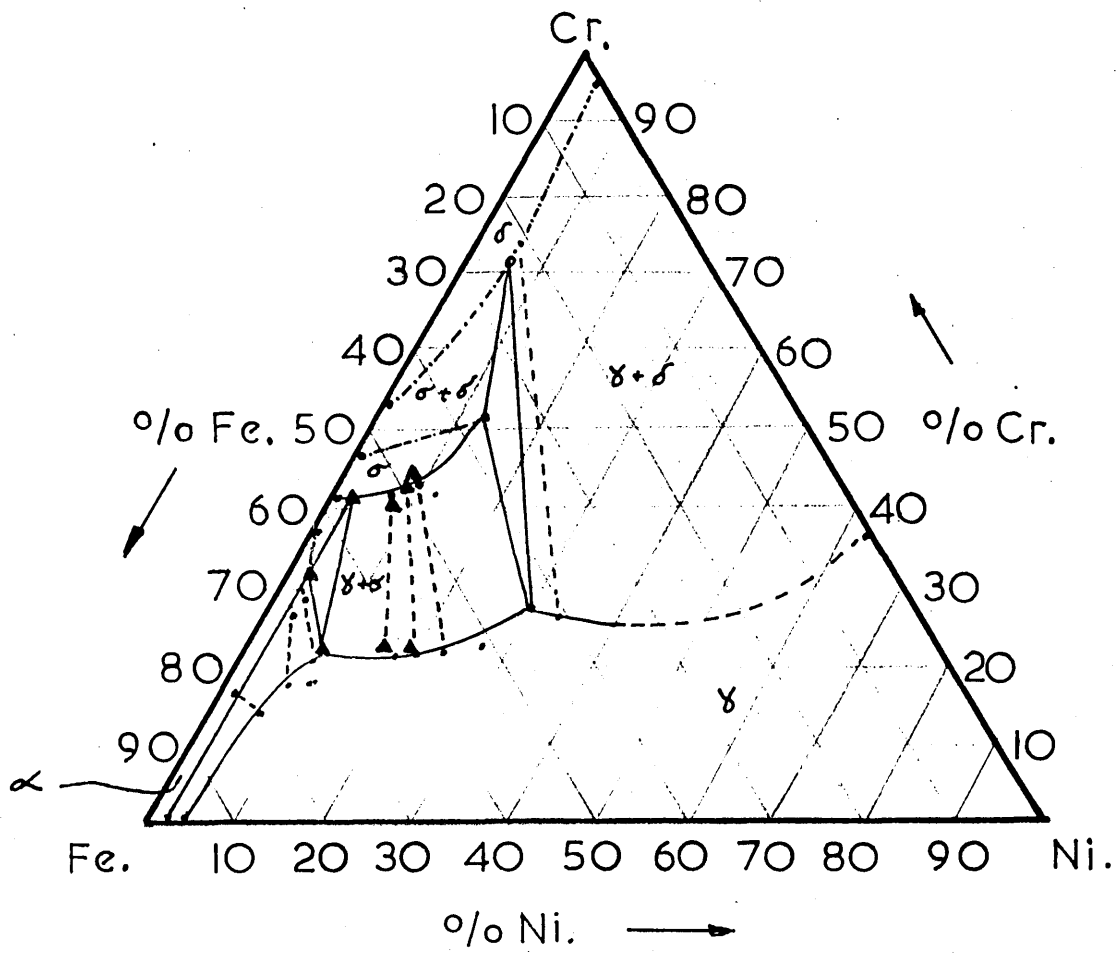
• Result At S.C.P.

▲ Result At Liverpool

- - - - Estimated phase boundaries, Ref 9.

FIG 29

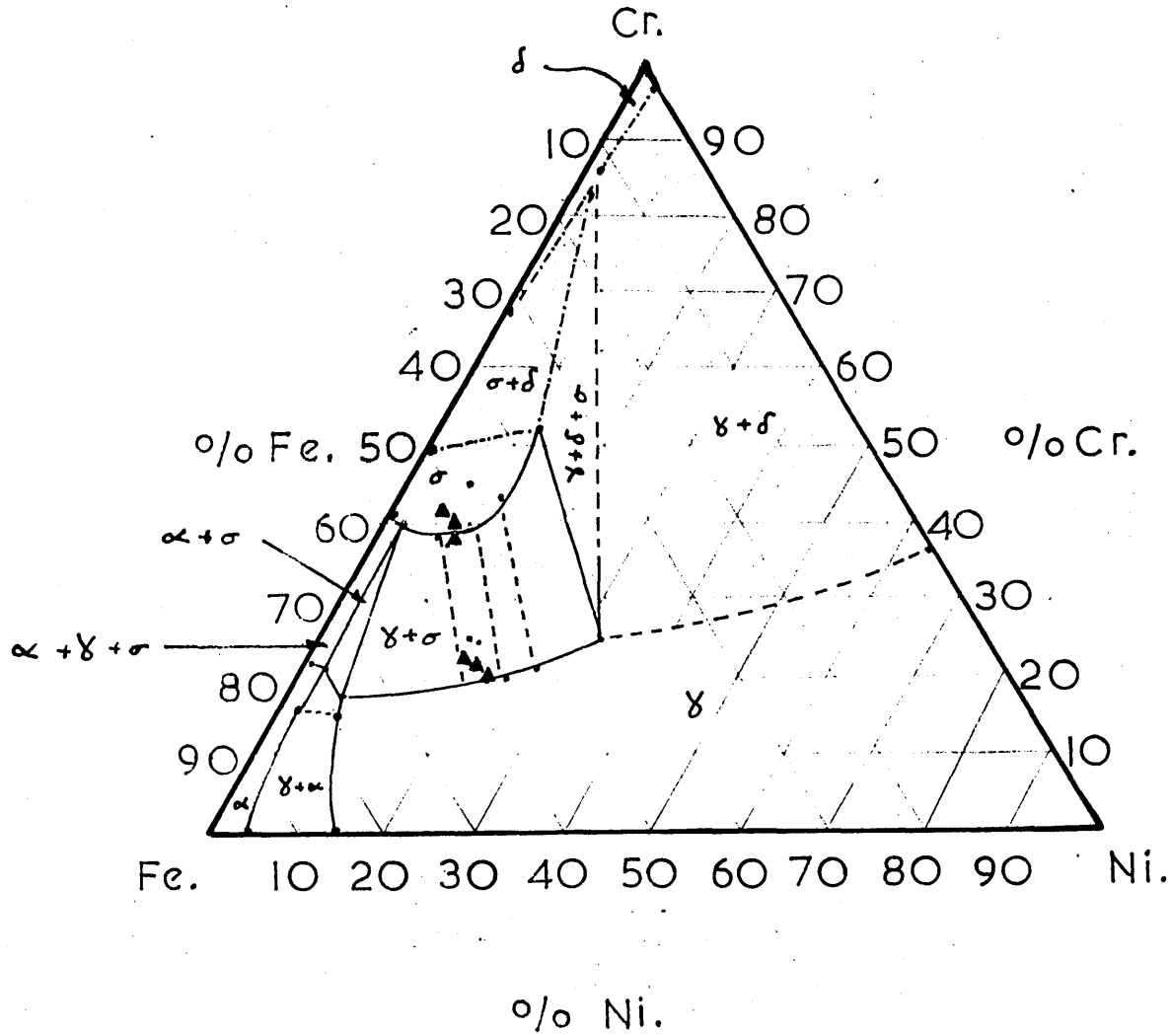
800°C Fe Cr Ni Isothermal
Section



- Result At S.C.P.
- ▲ Result At Liverpool
- Estimated phase boundaries, Ref 9.

FIG 30

650 °C Fe.-Cr.-Ni. Isothermal Section



• Result At S.C.P.
 ▲ Result At Liverpool

----- Estimated phase boundaries, Ref. 9.

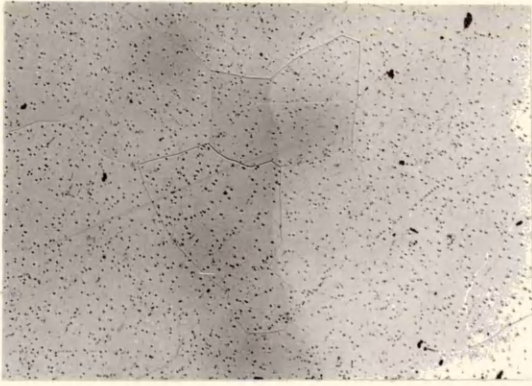
Fig 31

Shows the transformations occurring in alloy 3A(18Cr-2Ni) at 800°C as a function of isothermal treatment time which is given below.

The alloys had been cold rolled and solution treated at 1050°C prior to isothermal aging. The small black dots in micrograph (a) are etch pits which are a consequence of over etching which was necessary to reveal the ferrite grain boundaries. The cellular precipitate clearly visible in (d) is austenite (white) and $M_{23}C_6$ (dark).

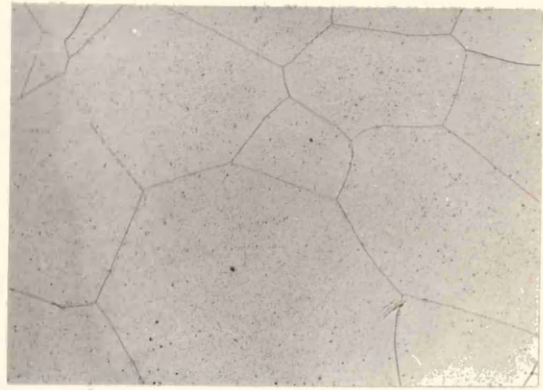
Etchant 10% Oxalic acid Electrolytic at 4V

- (a) 0 time at 800°C
- (b) 10 minutes at 800°C
- (c) 1 hour at 800°C
- (d) 20 hours at 800°C
- (e) 97 hours at 800°C
- (f) 200 hours at 800°C



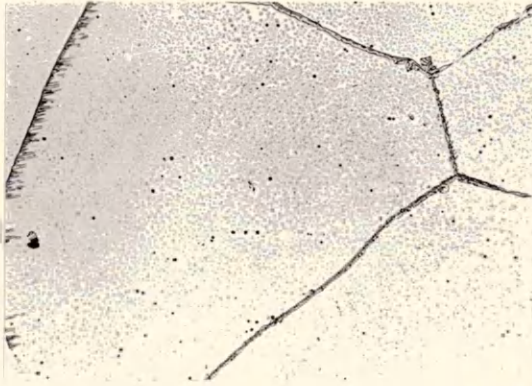
a

x50



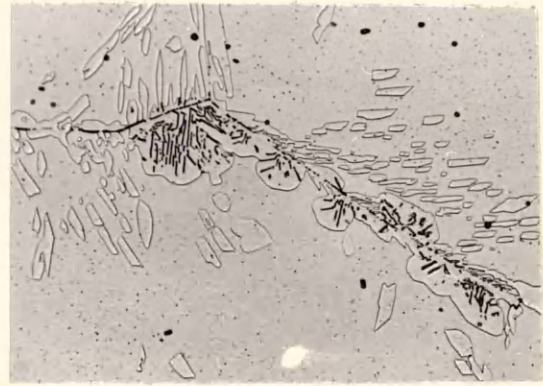
b

x100



c

x200



d

x450



e

x450



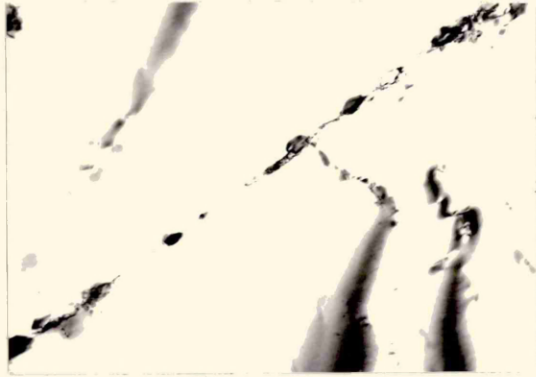
f

x100

Fig 32

Transmission Electron Micrographs of a grain boundary in alloy 3A(18Cr-2Ni) after 10 minutes at 800°C, (a) is in bright field whilst (b) is a dark field image showing the precipitates on the grain boundary. These precipitates have been identified as $M_{23}C_6$.

Polished at ambient temperature in a solution of 6% perchloric acid in acetic acid.



a

x26K



b

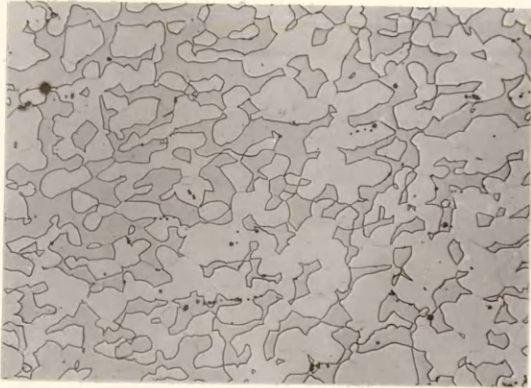
x26K

Fig 33

Shows the transformation occurring in alloy 1A(30Cr-13Ni) at 800°C as a function of isothermal treatment time given below. The alloy had been cold rolled and solution treated at 1050°C prior to isothermal aging.

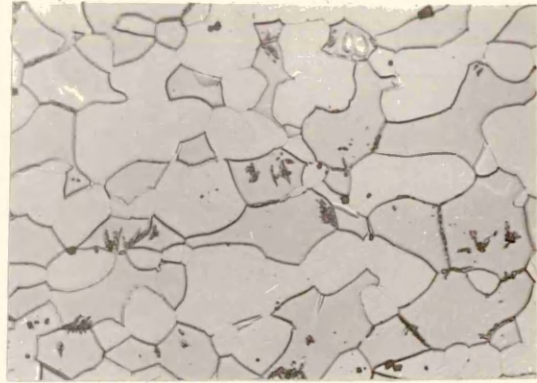
Etchant 10% oxalic acid, Electrolytic at ~ 4V

- (a) 0 time at 800°C
- (b) 10 minutes at 800°C
- (c) 30 minutes at 800°C
- (d) 1 hour at 800°C
- (e) 70 hours at 800°C
- (f) 120 hours at 800°C



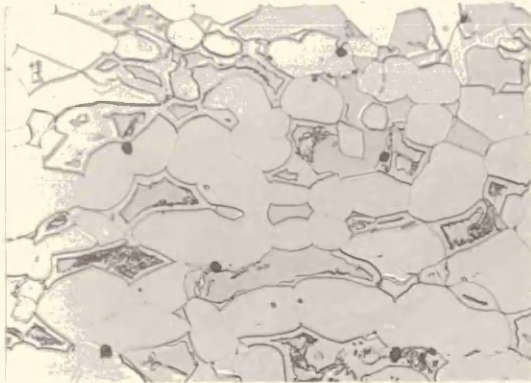
a

x200



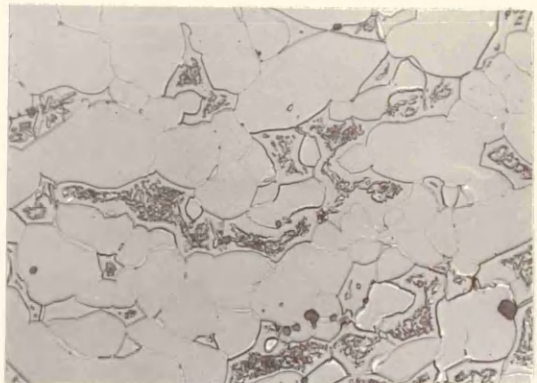
b

x450



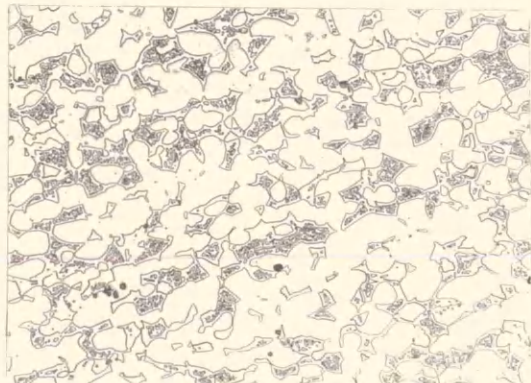
c

x450



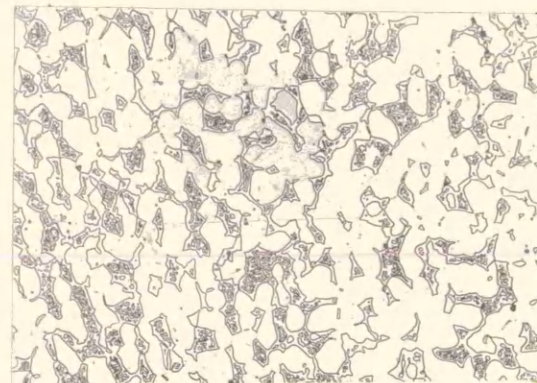
d

x450



e

x200



f

x200

Fig 34

Fig 34 (a) is a Transmission Electron Micrograph of an austenite-delta ferrite grain boundary after 10 minutes at 800°C. Dark field images shown in (b) and (c) indicate the precipitation of $M_{23}C_6$ and sigma phase respectively. The electron diffraction patterns shown in (d) and (e) were used to identify the precipitates shown in (b) and (c).

Polished at ambient temperature in a solution of 6% perchloric acid in acetic acid.



a

x20K



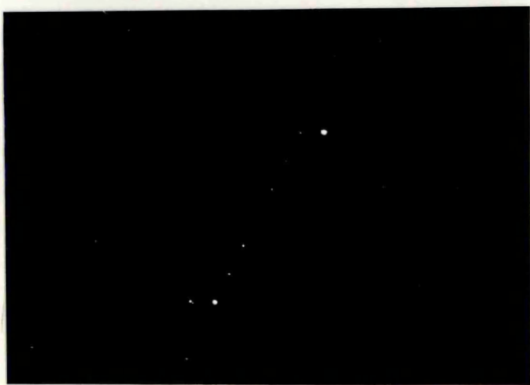
b

x20K



c

x20K



d



e

Fig 35

Transmission Electron Microscopy of alloy 1A(18Cr-2Ni) after aging for 1 hour at 800°C, showing the cellular structure of (austenite - sigma phase) evident in the optical micrograph Fig 34 (d).



a

x13K



b

x13K



c

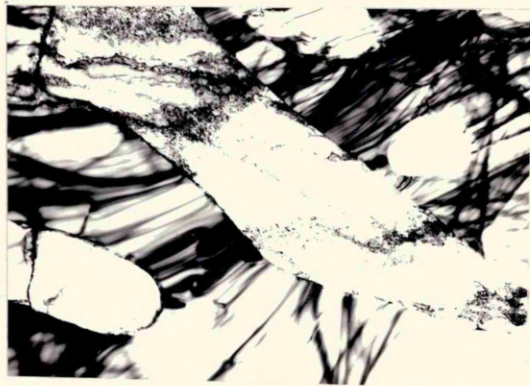
Fig 36

Transmission Electron Microscopy of alloy 1A(30Cr-13Ni) after aging for 120 hours at 800°C. Fig 36(a) shows a sigma grain in austenite whilst Fig 36(b) shows untransformed delta ferrite evident by the high dislocation density.



a

x20K



b

x10K

Fig 37

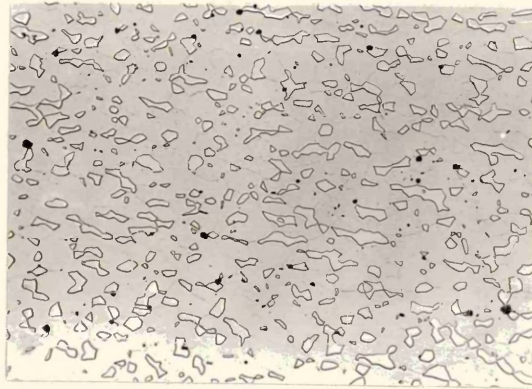
The microstructure of the manganese bearing alloys, equilibrated at 1050°C. The base alloy was (35Cr-28Ni) with the additions of manganese given below. The totally enclosed grains are delta ferrite whilst the matrix is austenite.

Etchant 10% Oxalic Acid Electrolytic at ~4V.

(a) (35Cr-28Ni) + 1.10wt%Mn

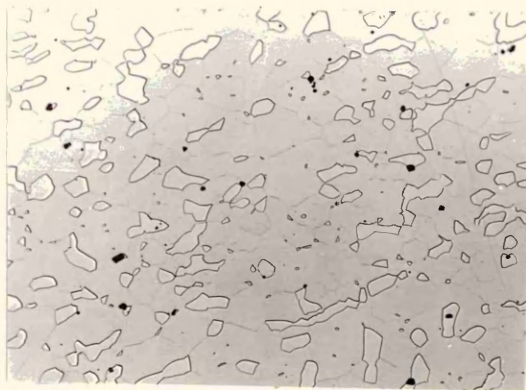
(b) (35Cr-28Ni) + 2.95wt%Mn

(c) (35Cr-28Ni) + 8.01wt%Mn



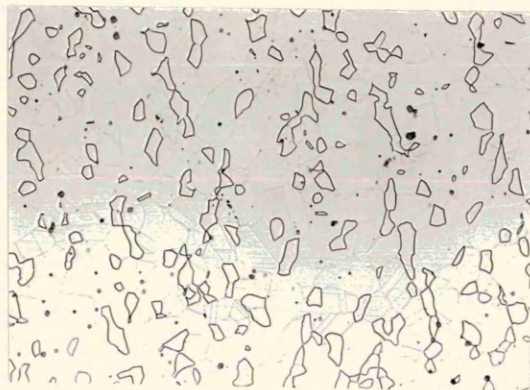
a

x200



b

x200



c

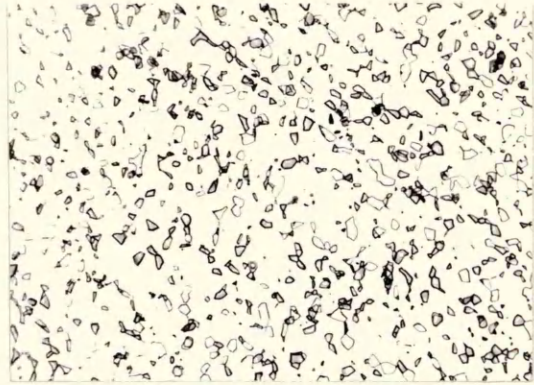
x200

Fig 38

The microstructure of the copper bearing alloy, equilibrated at 1050°C. The base alloy was (35Cr-28Ni) with the additions of copper given below. The dark grains are delta ferrite whilst the matrix is austenite.

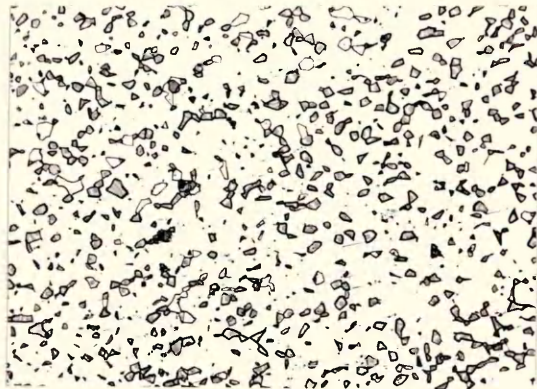
Etchant 10N. K OH Electrolytic at ~ 4V.

- (a) (35Cr-28Ni) + 1.10wt%Cu
- (b) (35Cr-28Ni) + 2.12wt%Cu
- (c) (35Cr-28Ni) + 7.50wt%Cu



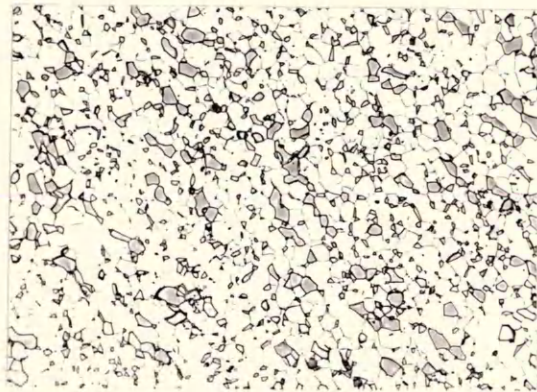
a

x150



b

x150



c

x150

Fig 39

The microstructure of the carbon bearing alloys, equilibrated at 1050°C. The base alloy composition was (35Cr-19Ni) with the additions of carbon given below. The white matrix phase is austenite, the dark phase is delta ferrite and the lighter intermediate phase is $M_{23}C_6$.

Etchant 10N. K OH Electrolytic at $\sim 4V$

(a) (35Cr-19Ni) + 0.09wt%C

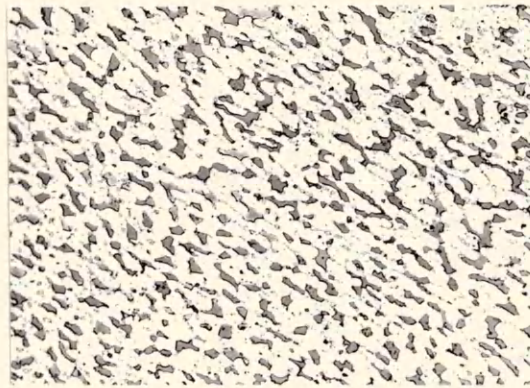
(b) (35Cr-19Ni) + 0.13wt%C

(c) (35Cr-19Ni) + 0.28wt%C



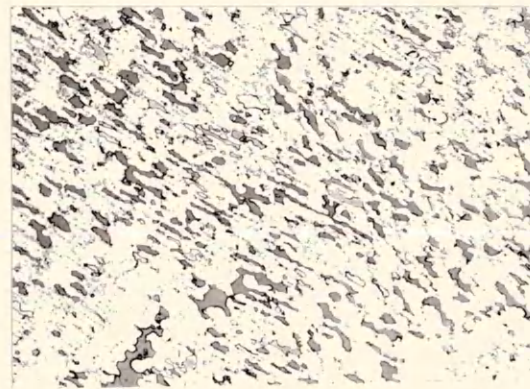
a

x100



b

x100



c

x100

Fig 40

The microstructure of the nitrogen bearing alloys, equilibrated at 1050°C. The base alloy composition was (35Cr-29Ni) with the additions of nitrogen given below. The white matrix phase is austenite, whilst the dark phase is delta ferrite.

Etchant 10N. K OH Electrolytic at ~4V

- (a) (35Cr-19Ni) + 0.04wt%N
- (b) (35Cr-19Ni) + 0.068wt%N
- (c) (35Cr-19Ni) + 0.14wt%N



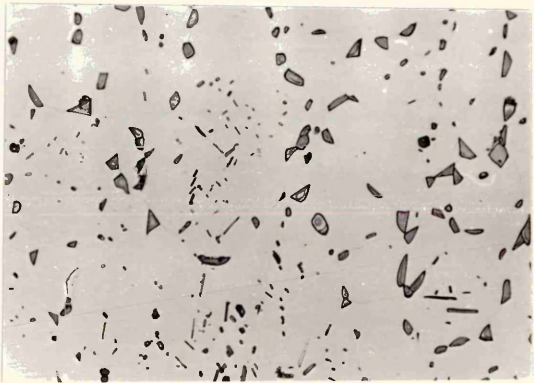
a

x450



b

x450



c

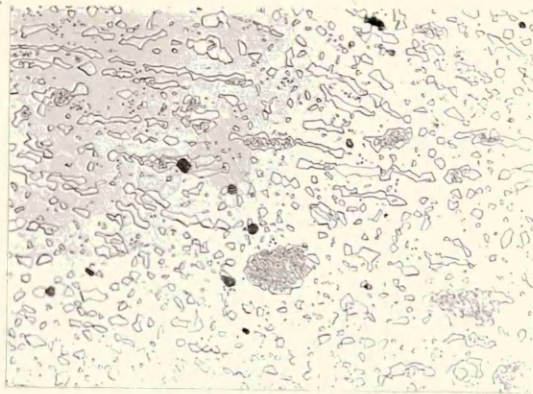
x450

Fig 41

The microstructure of the manganese bearing alloys, equilibrated at 800°C. The base alloy composition was (35Cr-28Ni) with the additions of manganese given below. At 1wt% Mn (a) the second phase which is totally enclosed is delta ferrite, whereas at the 8wt%Mn addition considerable amounts of sigma phase are evident.

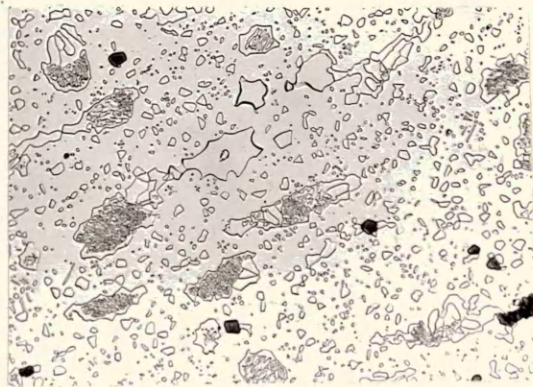
Etchant 10% Oxalic Acid Electrolytic at ~4V

- (a) (35Cr-28Ni) + 1.10wt%Mn
- (b) (35Cr-28Ni) + 2.95wt%Mn
- (c) (35Cr-28Ni) + 8.01wt%Mn



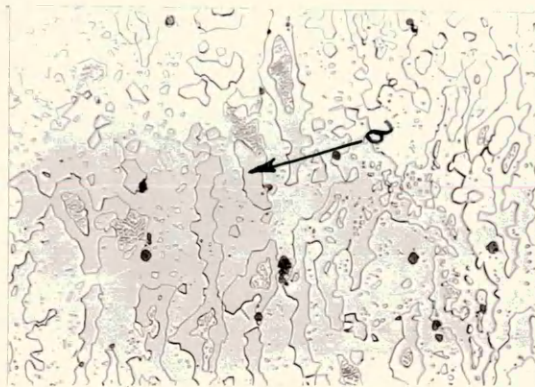
a

x450



b

x450



c

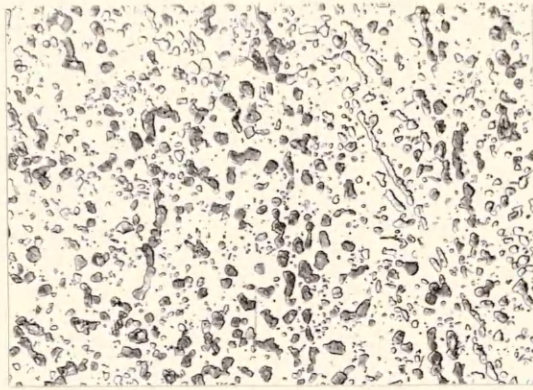
x450

Fig 42

The microstructure of the copper bearing alloys, equilibrated at 800°C. The base alloy composition was (35Cr-28Ni) with the additions of copper given below. The dark phase is delta ferrite and the lighter matrix, austenite.

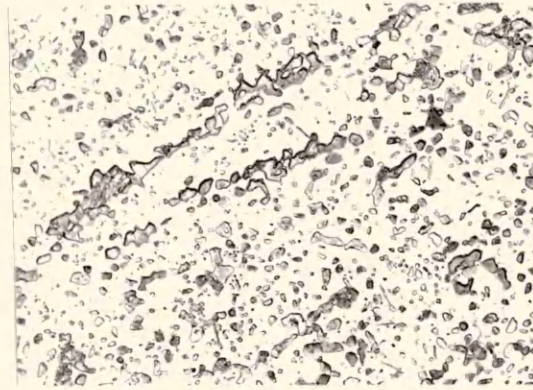
Etchant 10N. K OH Electrolytic at ~ 4V

- (a) (35Cr-28Ni) + 1.10wt%Cu
- (b) (35Cr-28Ni) + 2.12wt%Cu
- (c) (35Cr-28Ni) + 7.50wt%Cu



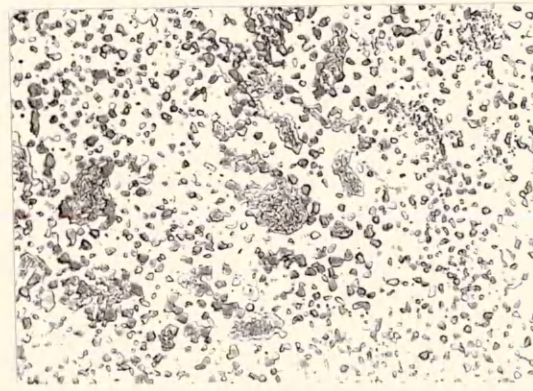
a

x450



b

x450



c

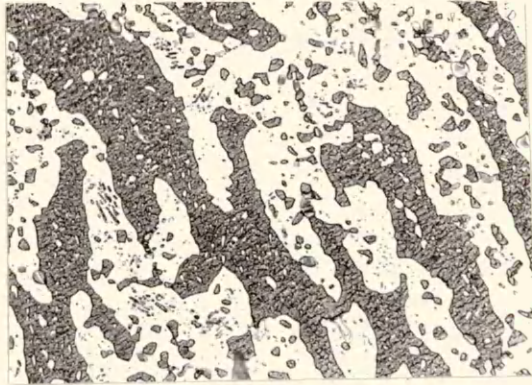
x450

Fig 43

The microstructure of the carbon bearing alloys, equilibrated at 800°C. The base alloy composition was (35Cr-19Ni) with the additions of carbon given below. The white matrix phase is austenite, the dark phase is sigma and the lighter intermediate phase is $M_{23}C_6$.

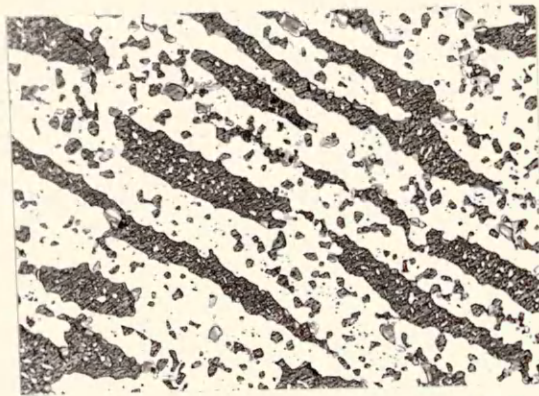
Etchant 10N. K OH Electrolytic at \sim 4V

- (a) (35Cr-19Ni) + 0.09wt%C
- (b) (35Cr-19Ni) + 0.13wt%C
- (c) (35Cr-19Ni) + 0.28wt%C



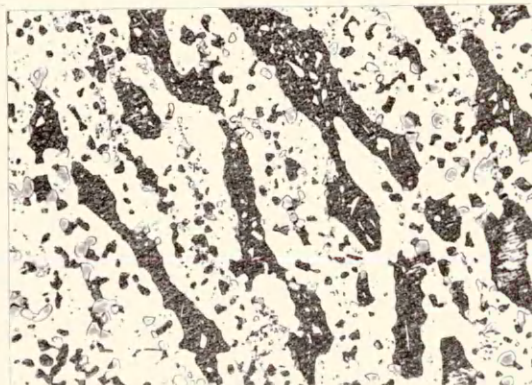
a

x450



b

x450



c

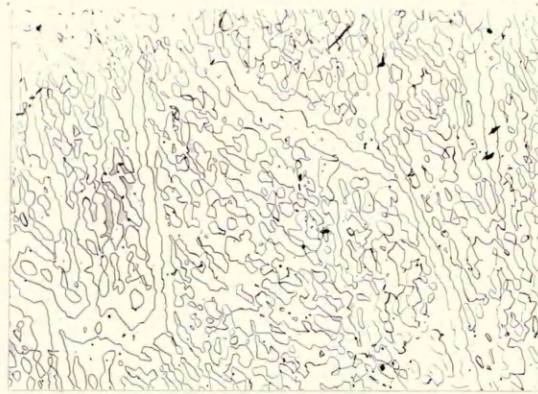
x450

Fig 44

The microstructure of the silicon bearing alloys, equilibrated at 1050°C. The base alloy composition was (30Cr-13Ni) with the silicon additions given below. The darker matrix phase is delta ferrite and the lighter phase austenite.

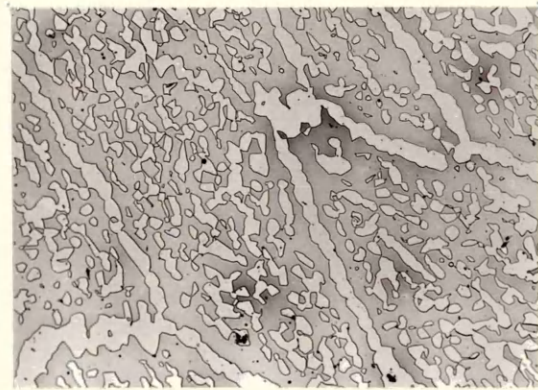
Etchant 10N. K OH Electrolytic at ~ 4V

- (a) (30Cr-13Ni) + 0.85wt%Si
- (b) (30Cr-13Ni) + 1.80wt%Si
- (c) (30Cr-13Ni) + 3.75wt%Si



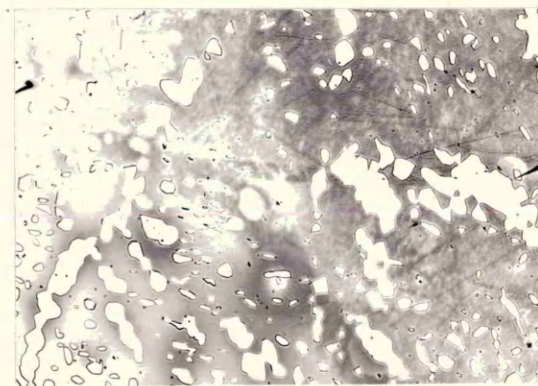
a

x100



b

x100



c

x 100

Fig 45

The microstructure of the molybdenum bearing alloys, equilibrated at 1050°C. The base alloy composition was (27Cr-16Ni) with the molybdenum additions given below. The darker phase is delta ferrite with an austenite matrix.

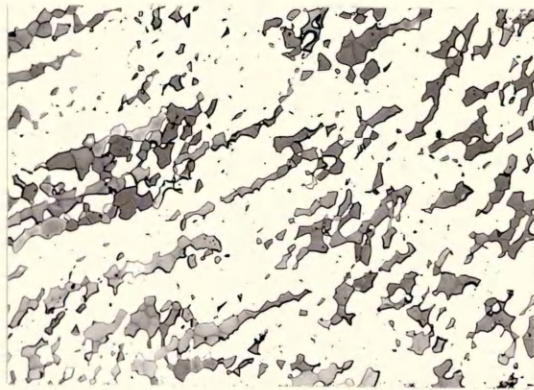
Etchant 10N. K OH Electrolytic at ~ 4V

- (a) (27Cr-16Ni) + 0.92wt%Mo
- (b) (27Cr-16Ni) + 1.98wt%Mo
- (c) (27Cr-16Ni) + 3.74wt%Mo



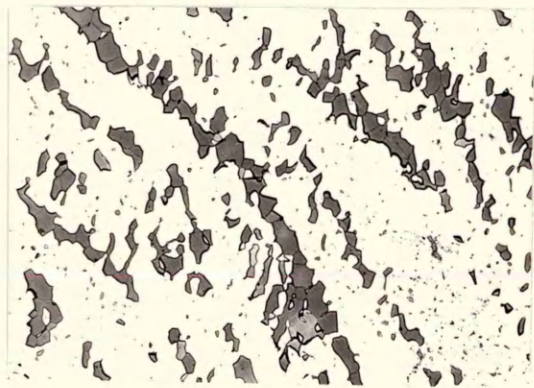
a

x100



b

x100



c

x100

Fig 46

Transmission Electron micrographs of molybdenum series alloy containing 1wt%Mo, equilibrated at 1050°C. The large black precipitate shown in (b) was identified as a M_6C type carbide.

Polished at room temperature in an electrolyte of 6% perchloric acid in acetic acid.



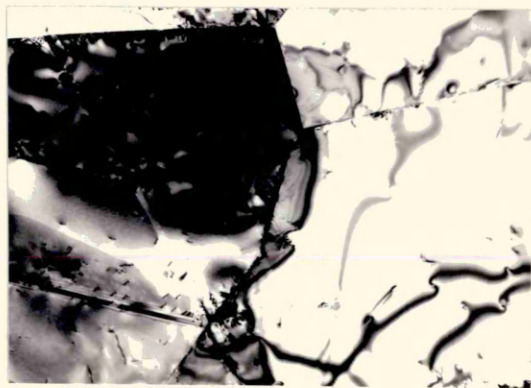
a

x50K



b

x13K



c

x13K

Fig 42

The microstructure of the niobium bearing alloys, equilibrated at 1050°C. The base alloy composition was (25Cr-18Ni) with the niobium additions given below. The lighter matrix phase is austenite and the darker phase delta ferrite. A third phase is clearly visible in (c) which has been identified as a Laves phase Fe₂Nb.

Etchant 10N. K OH. Electrolytic at ~4V

- (a) (25Cr-18Ni) + 0.48wt%Nb
- (b) (25Cr-18Ni) + 1.06wt%Nb
- (c) (25Cr-18Ni) + 2.16wt%Nb



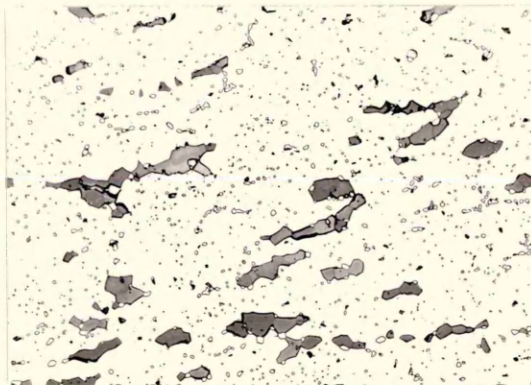
a

x 200



b

x 200



c

x 200

Fig 48

Transmission Electron Micrographs showing the bright field (a) and dark field (b) images of a random precipitate within the 2Wt%Nb alloy equilibrated at 1050°C. This phase was identified using electron diffraction techniques as Laves phase.

Polished at room temperature using an electrolyte of 6% perchloric acid in acetic acid.



a

x20K



b

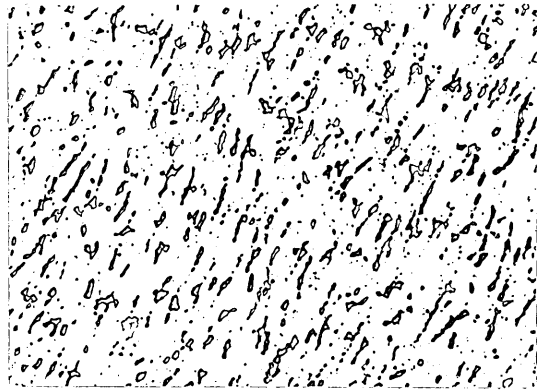
x20K

Fig 49

The microstructure of the titanium bearing alloys, equilibrated at 1050°C. The base alloy composition was (26Cr-18Ni) with the titanium additions given below. The darker phase is delta ferrite with the lighter matrix phase austenite.

Etchant 10N. K OH. Electrolytic at ~ 4V

- (a) (26Cr-18Ni) + 0.34Wt%Ti
- (b) (26Cr-18Ni) + 0.54Wt%Ti
- (c) (26Cr-18Ni) + 1.05Wt%Ti



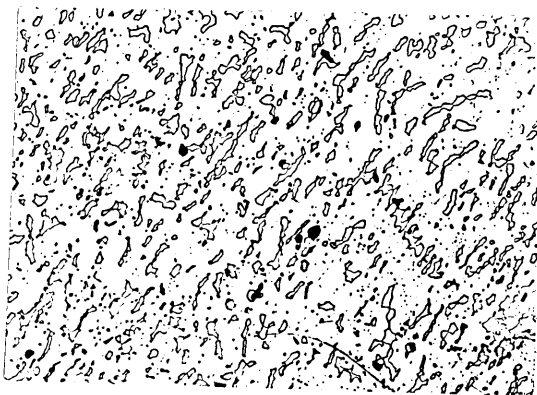
a

x50



b

x50



c

x50

Fig 50

Transmission Electron Microscopy of the alloy containing 0.34Wt%Ti, equilibrated at 1050°C. Fig 51(a) shows a grain boundary triple point and the absence of precipitates at the grain boundaries. Fig 51 (b) and (c) are a pair of bright and dark field micrographs show a precipitate within the matrix which was identified as an M C type carbide by electron diffraction techniques.

Polished at room temperature in an electrolyte of 6% perchloric acid in acetic acid.



a

x20K



b

x20K



c

x20K

Fig 51

The microstructure of the silicon bearing alloys, equilibrated at 800°C. The base alloy composition was (30Cr-13Ni) with the silicon additions given below. At 800°C the microstructures were much finer but generally the lighter phase was austenite, and the darker phase sigma.

Etchant 10% Oxalic acid. Electrolytic at ~4V

(a) (30Cr-13Ni) + 0.85wt%Si

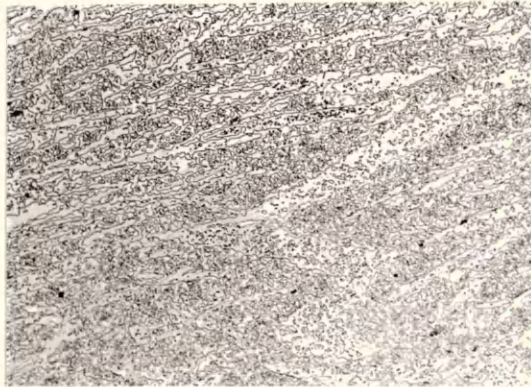
(b) (30Cr-13Ni) + 1.80wt%Si

(c) (30Cr-13Ni) + 3.75wt%Si



a

x 200



b

x 200



c

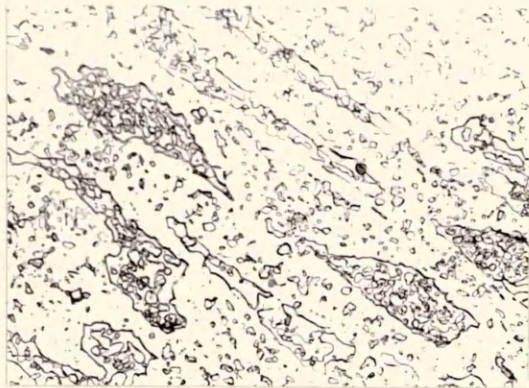
x 200

Fig 52

The microstructure of the molybdenum bearing alloys, equilibrated at 800°C. The base alloy composition was (27Cr-16Ni) with the molybdenum additions given below. The matrix phase is austenite, whilst the totally enclosed phase is sigma.

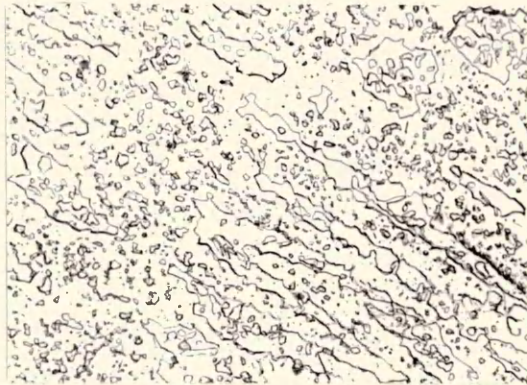
Etchant 10% Oxalic acid Electrolytic at ~4V

- (a) (27Cr-16Ni) + 0.92Wt%Mo
- (b) (27Cr-16Ni) + 1.98Wt%Mo
- (c) (27Cr-16Ni) + 3.74Wt%Mo



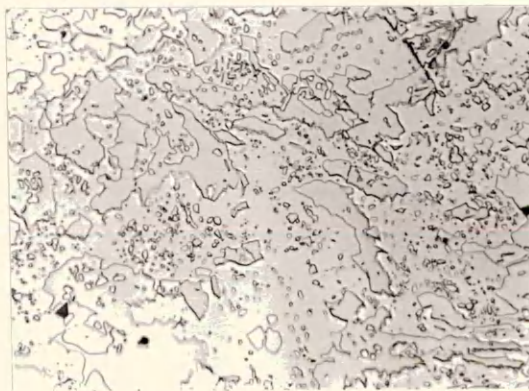
a

x450



b

x450



c

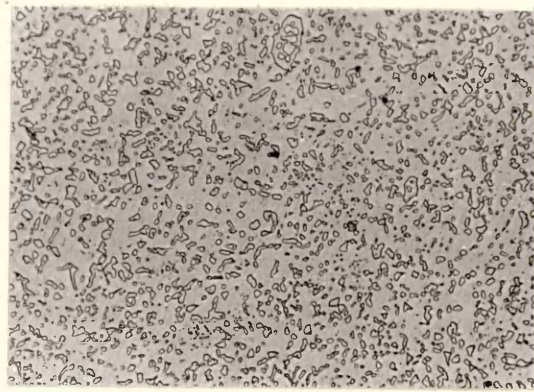
x450

Fig 53

The microstructure of the niobium bearing alloys, equilibrated at 800°C. The base alloy composition was (25Cr-18Ni) with the niobium additions given below. The matrix phase is austenite, whilst the totally enclosed phase is sigma.

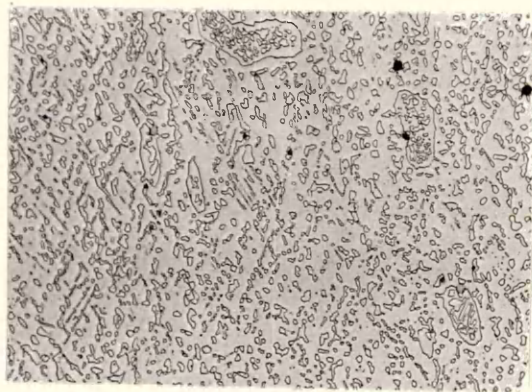
Etchant 10% Oxalic acid. Electrolytic at ~4V

- (a) (25Cr-18Ni) + 0.48wt%Nb
- (b) (25Cr-18Ni) + 1.06wt%Nb
- (c) (25Cr-18Ni) + 2.16wt%Nb



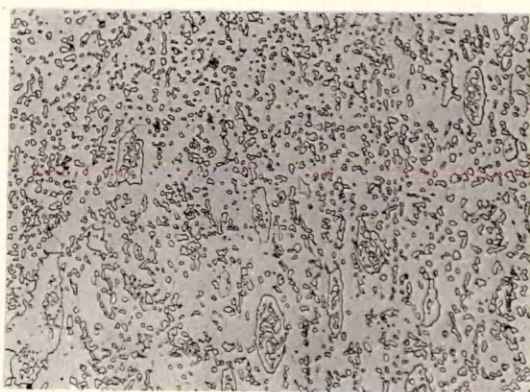
a

x200



b

x 200



c

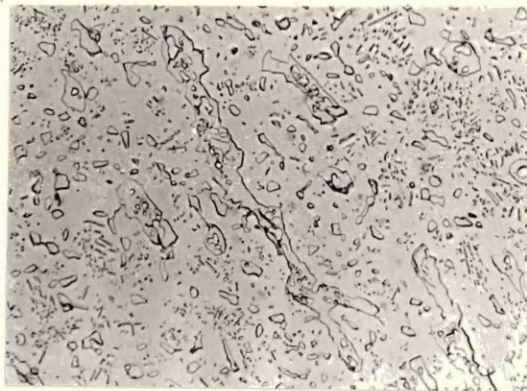
x 200

Fig 54

The microstructure of the titanium bearing alloys, equilibrated at 800°C. The base alloy composition was (26Cr-18Ni) with the titanium additions given below. The matrix phase is austenite, whilst the totally enclosed phase is sigma.

Etchant 10% Oxalic acid, Electrolytic at ~ 4V

- (a) (26Cr-18Ni) + 0.34wt%Ti
- (b) (26Cr-18Ni) + 0.54wt%Ti
- (c) (26Cr-18Ni) + 1.05wt%Ti



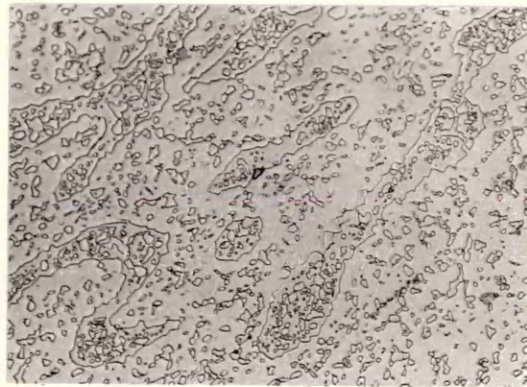
a

x450



b

x450



c

x450

Fig. 55

The effect of austenite forming additions on the delta ferrite content at 1050°C.

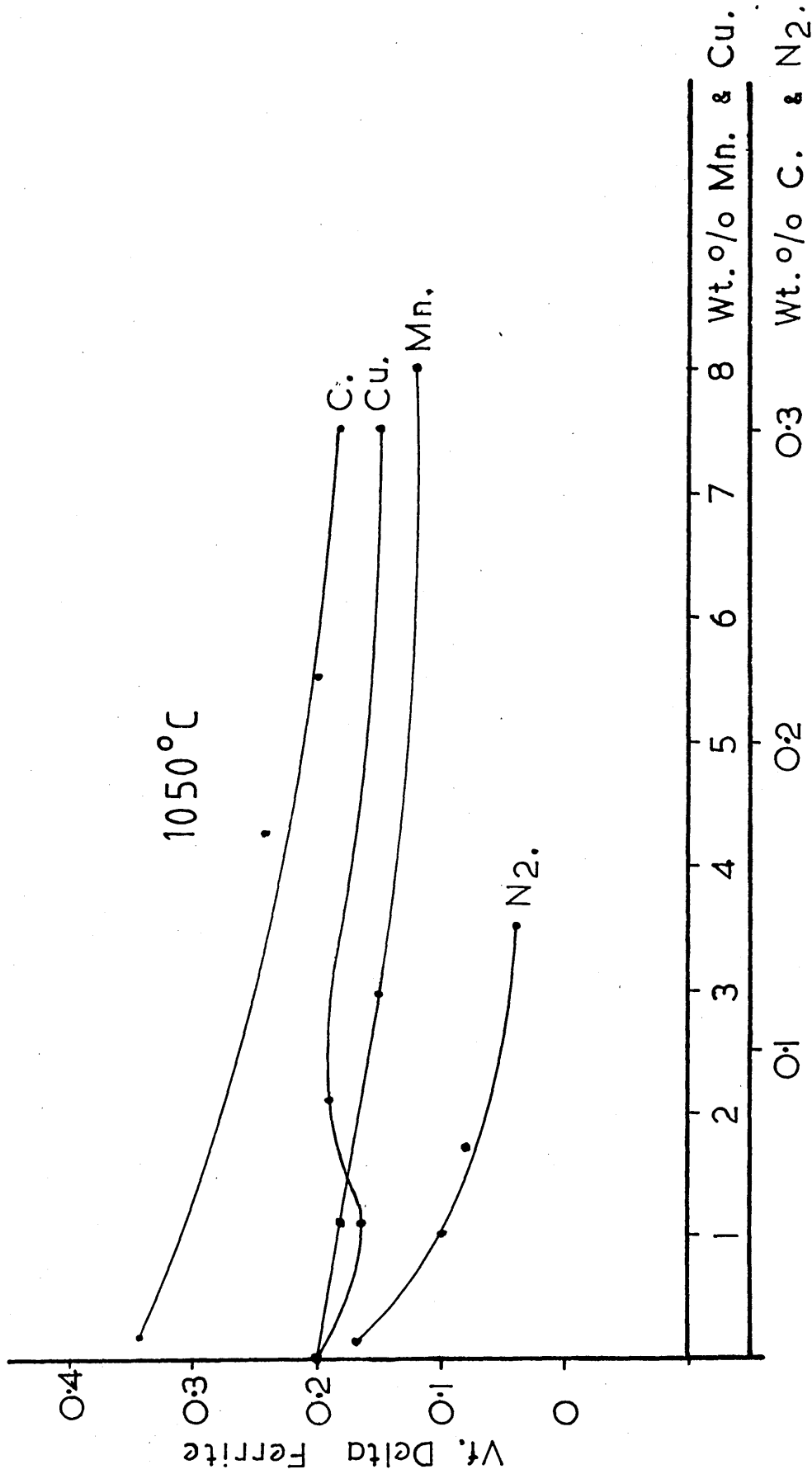


Fig. 56

The effect of austenite forming additions on the delta ferrite or sigma phase content at 800°C.

Fig. 57

The effect of delta ferrite/sigma phase forming additions on the delta ferrite content at 1050°C.

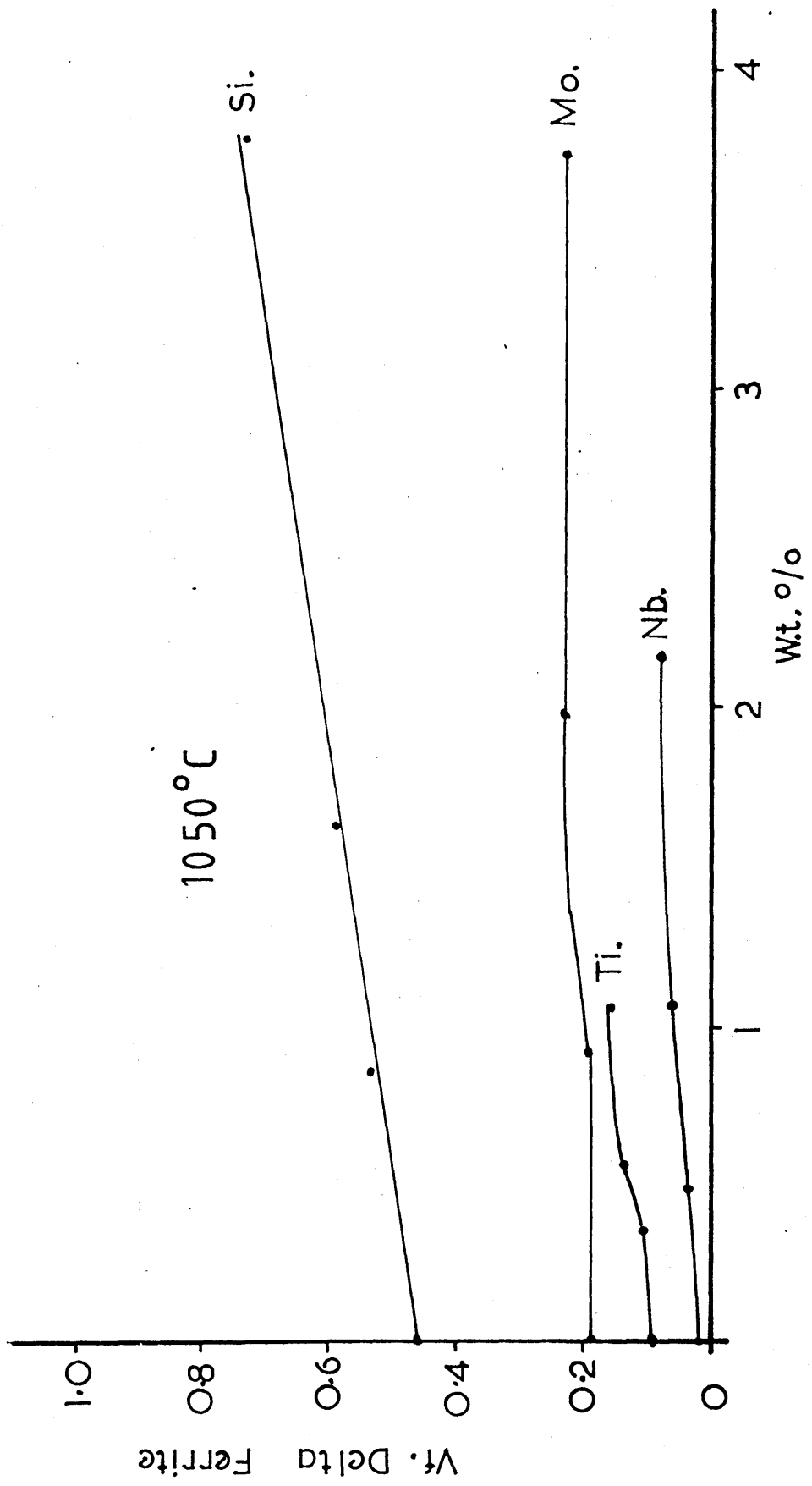


Fig. 58

The effect of delta ferrite/sigma phase forming additions on the sigma phase content at 800°C.

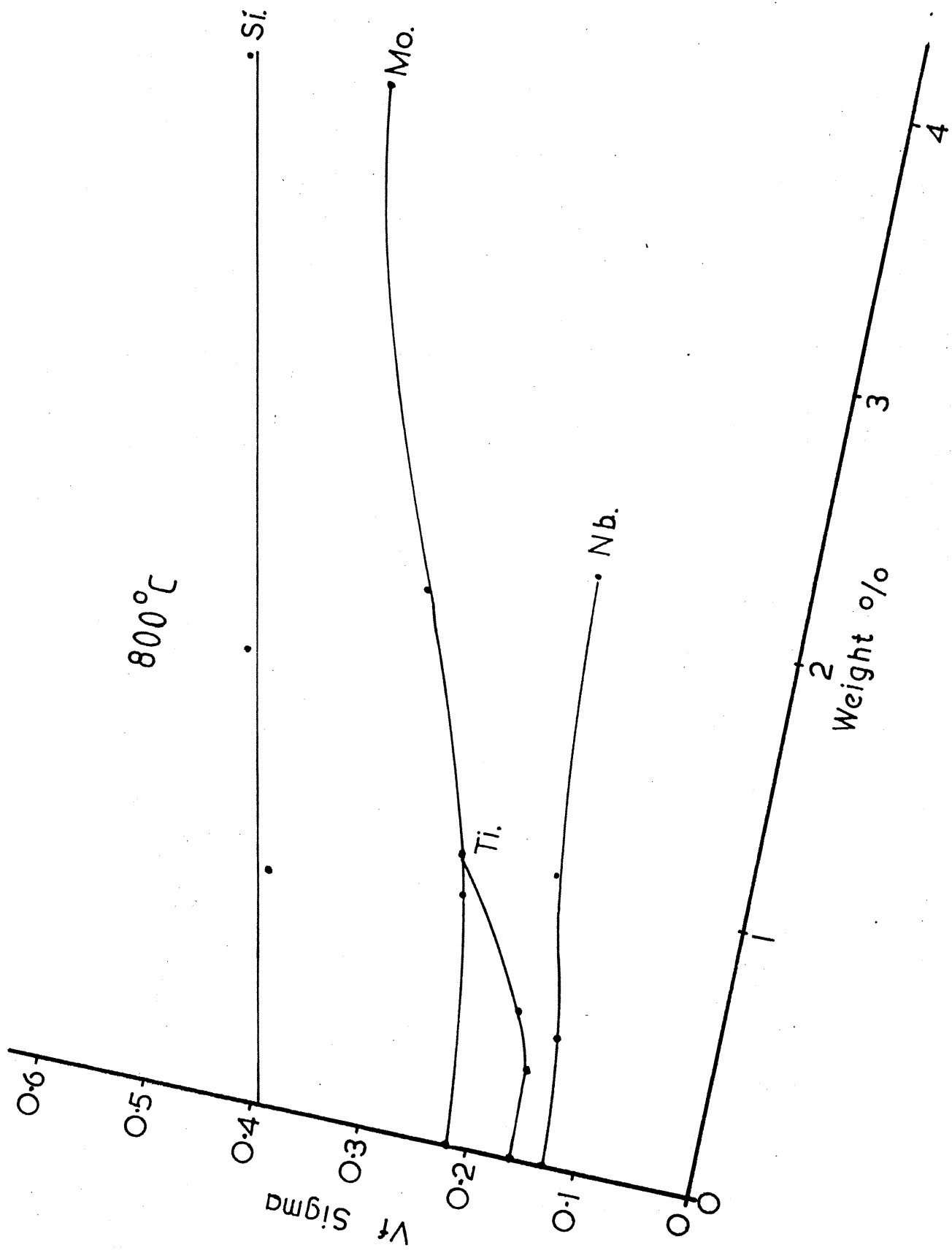


Fig. 59

Schematic description of the method for determining the effect of nickel and chromium on the delta ferrite or sigma phase content of a particular composition.

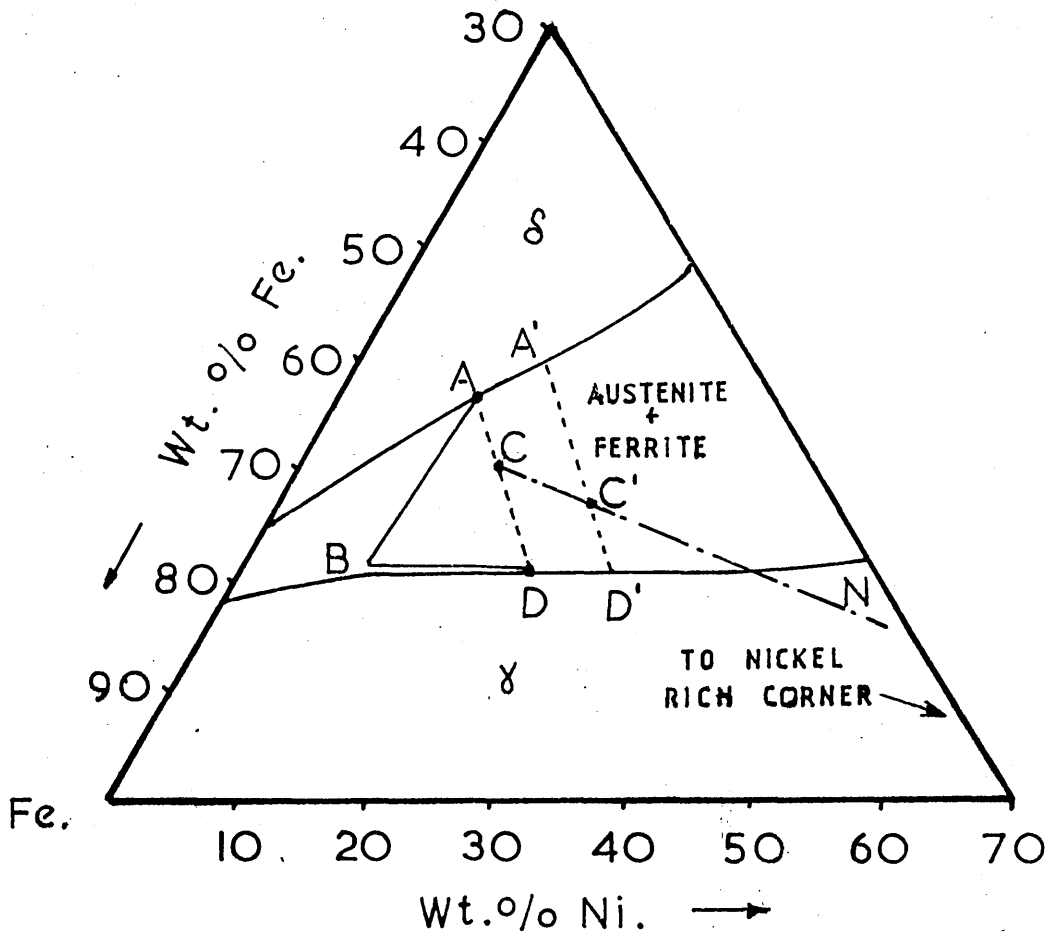


Fig. 60

Shows the change in delta ferrite as the nickel content increases, the volume fraction changes being determined by the use of the isothermal sections of the Fe-Cr-Ni system which was determined in this work.

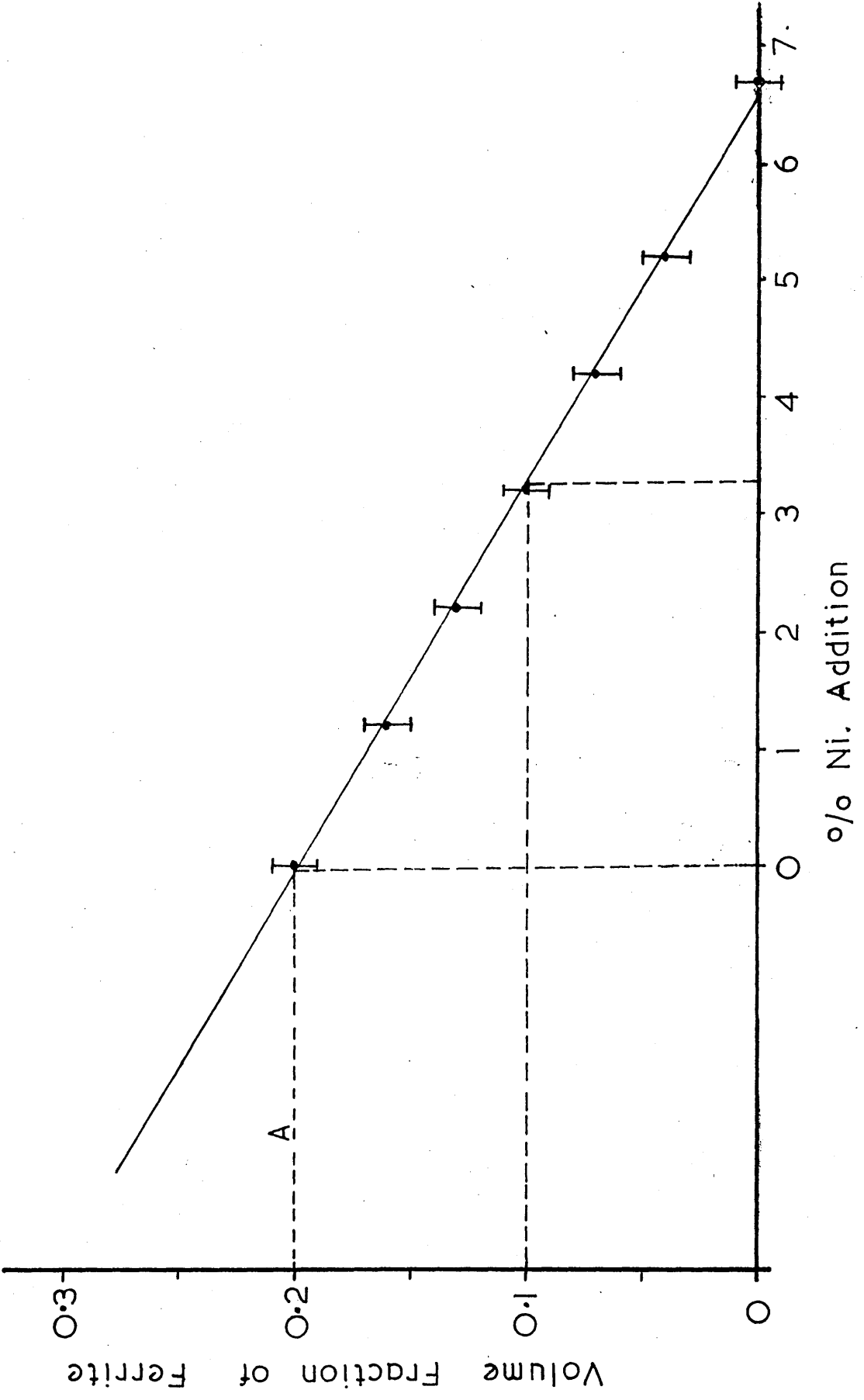


Fig. 61

The nickel equivalent of manganese at 1050°C and 800°C
as a function of manganese content.

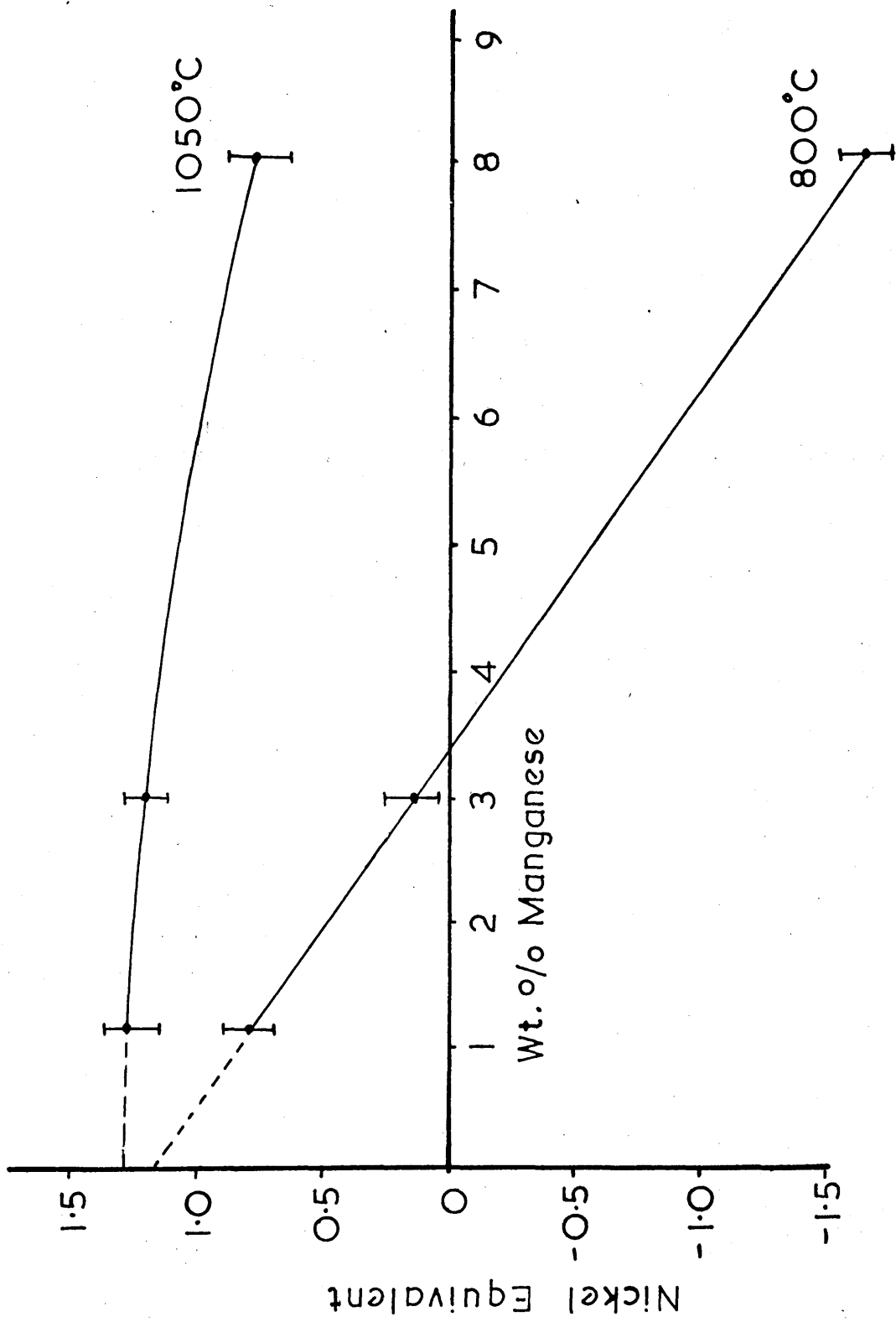


Fig. 62

The nickel equivalent of copper at 1050°C and 800°C as a function of copper content.

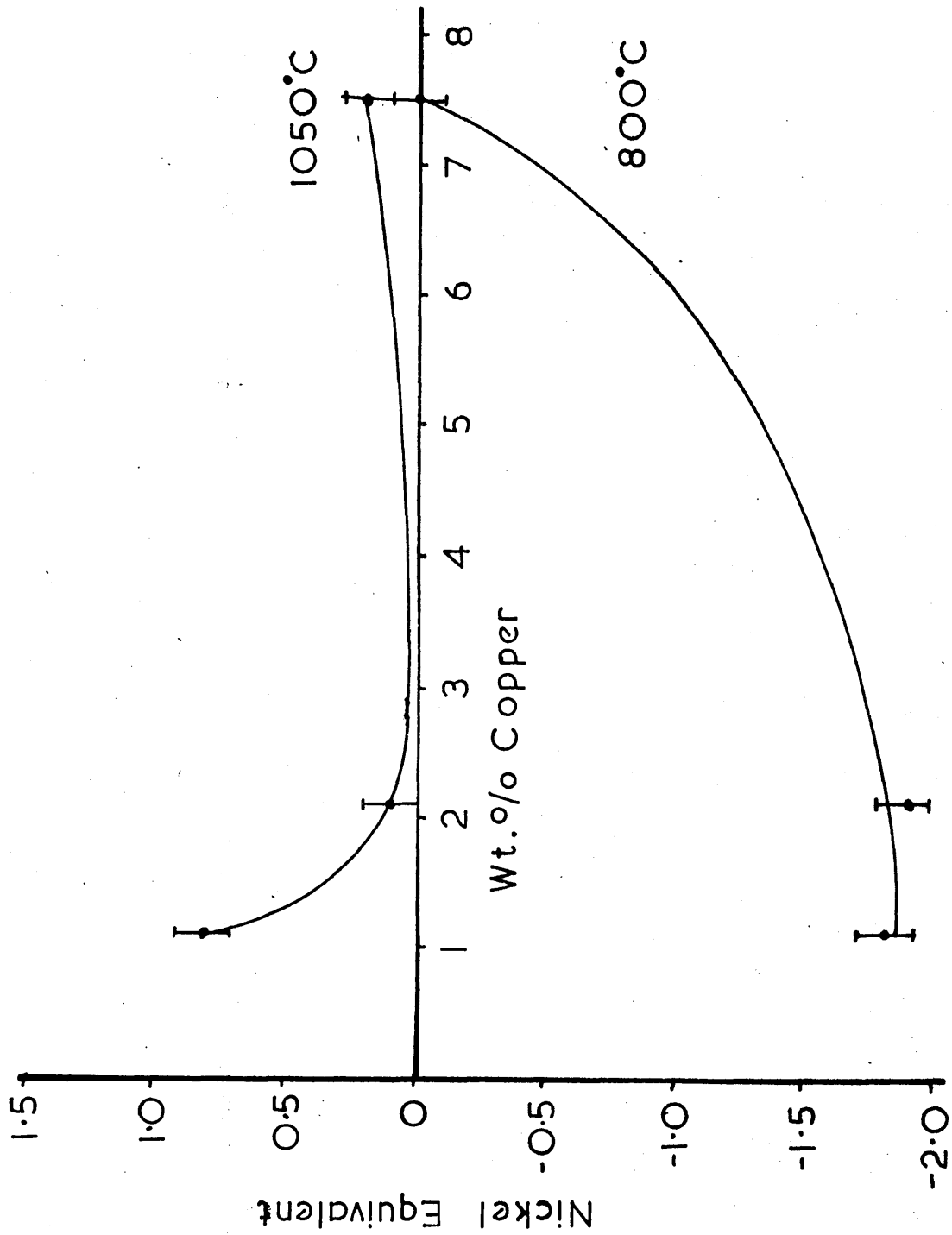


Fig. 63

The nickel equivalent of nitrogen at 1050°C and 800°C as a function of nitrogen content.

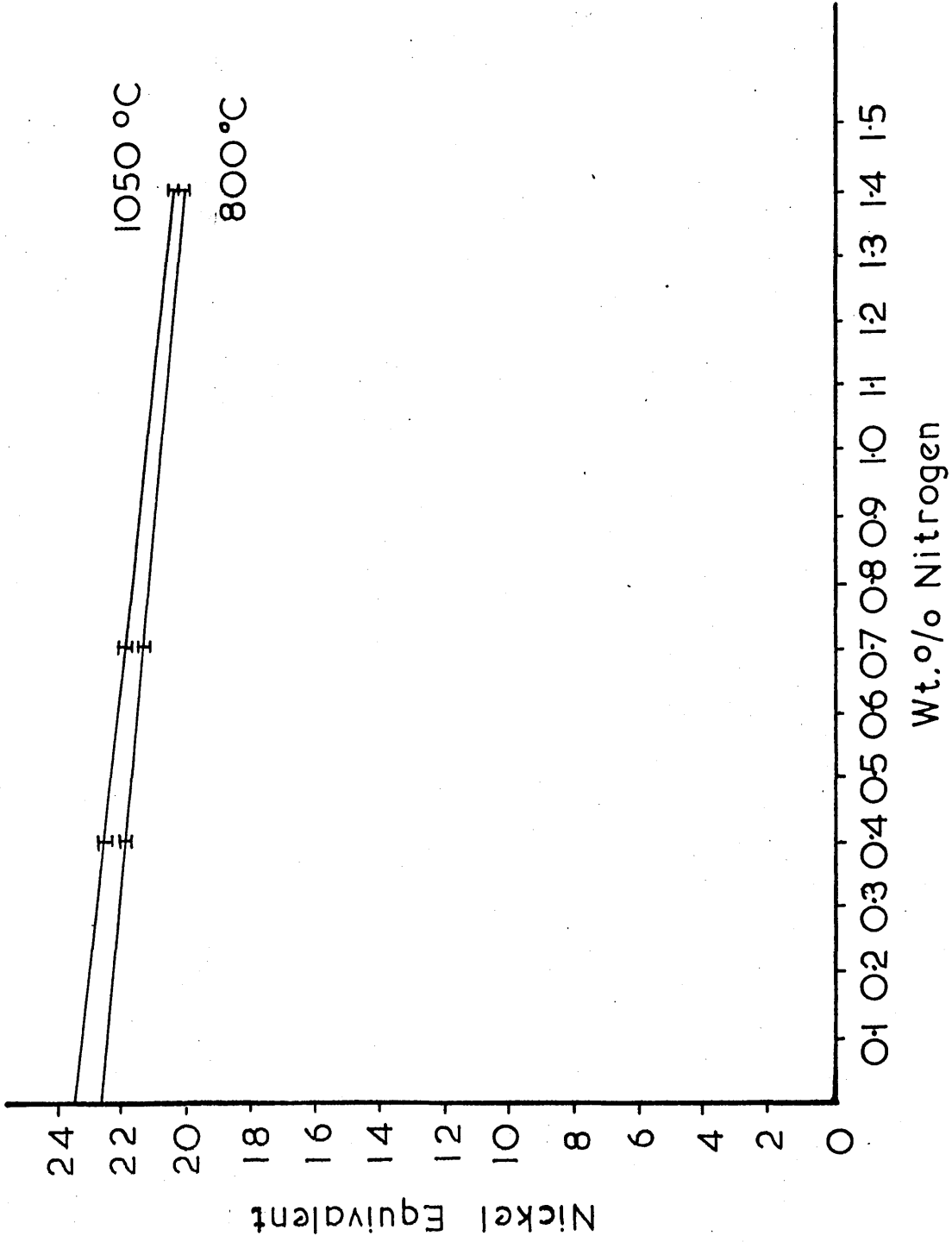


Fig. 64

The chromium equivalent of silicon at 1050°C and 800°C
as a function of silicon content.

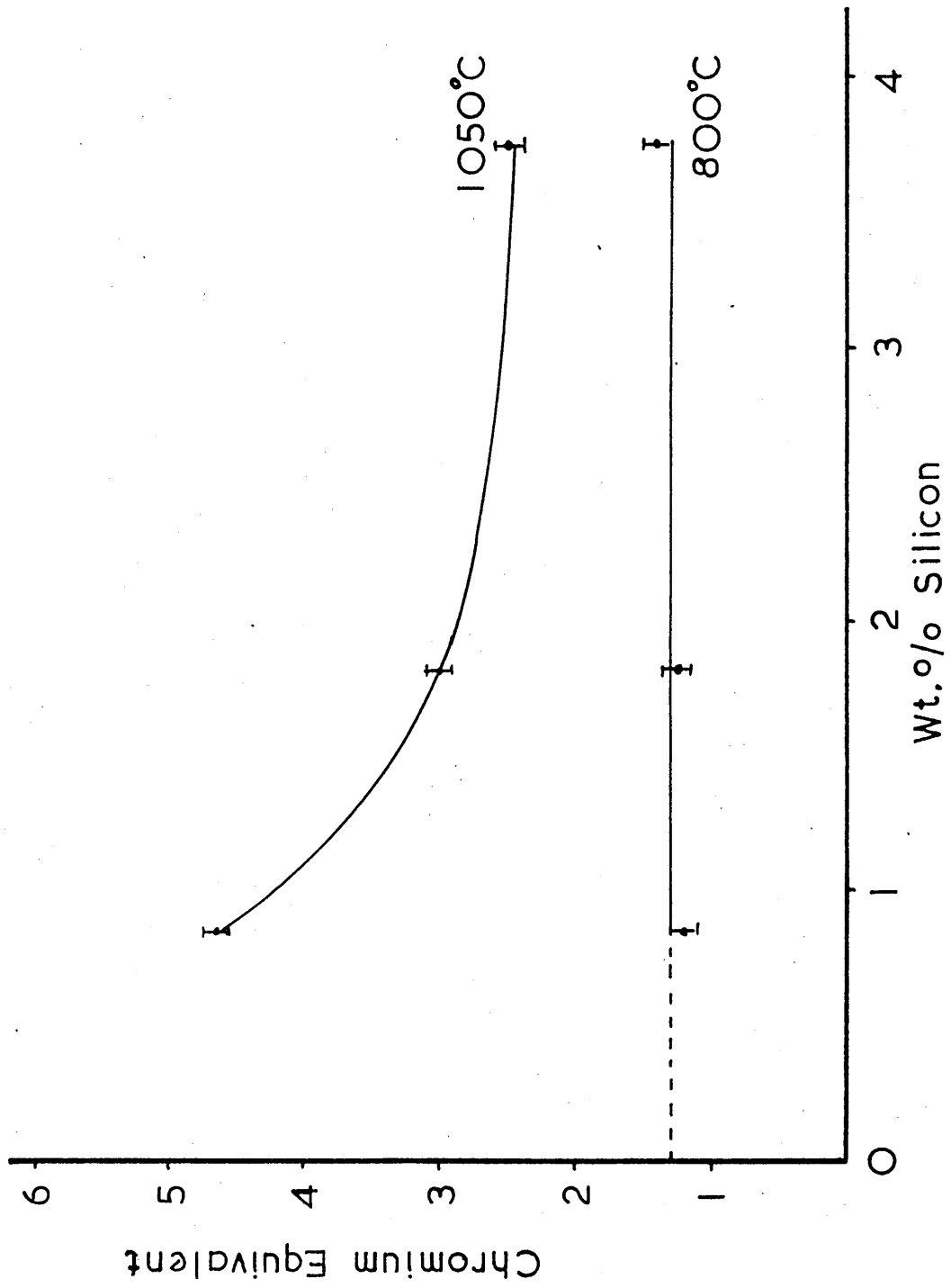


Fig. 65

The chromium equivalent of molybdenum at 1050°C and 800°C
as a function of molybdenum content.

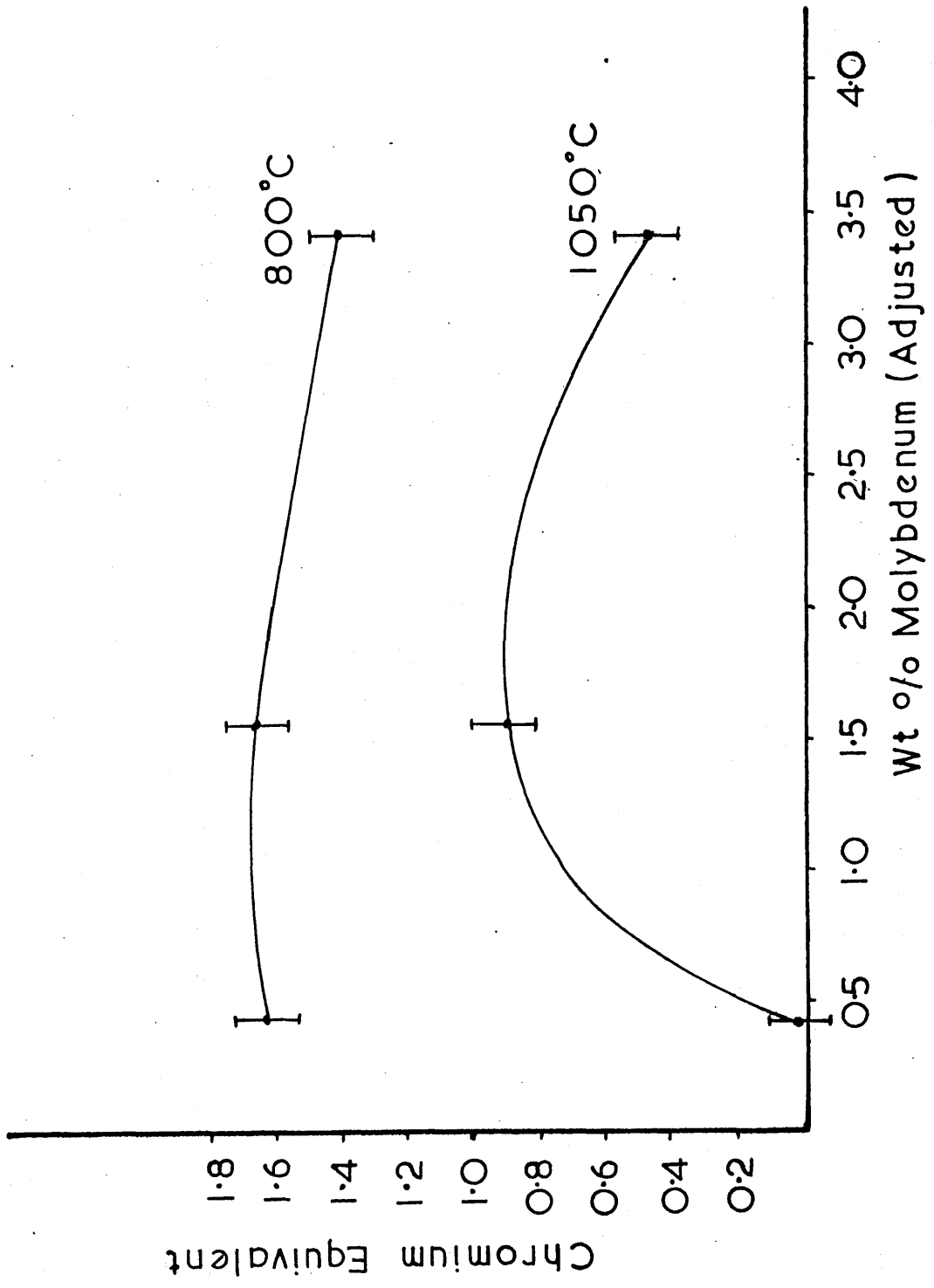


Fig. 66

The chromium equivalent of niobium at 1050°C and 800°C as a function of niobium content.

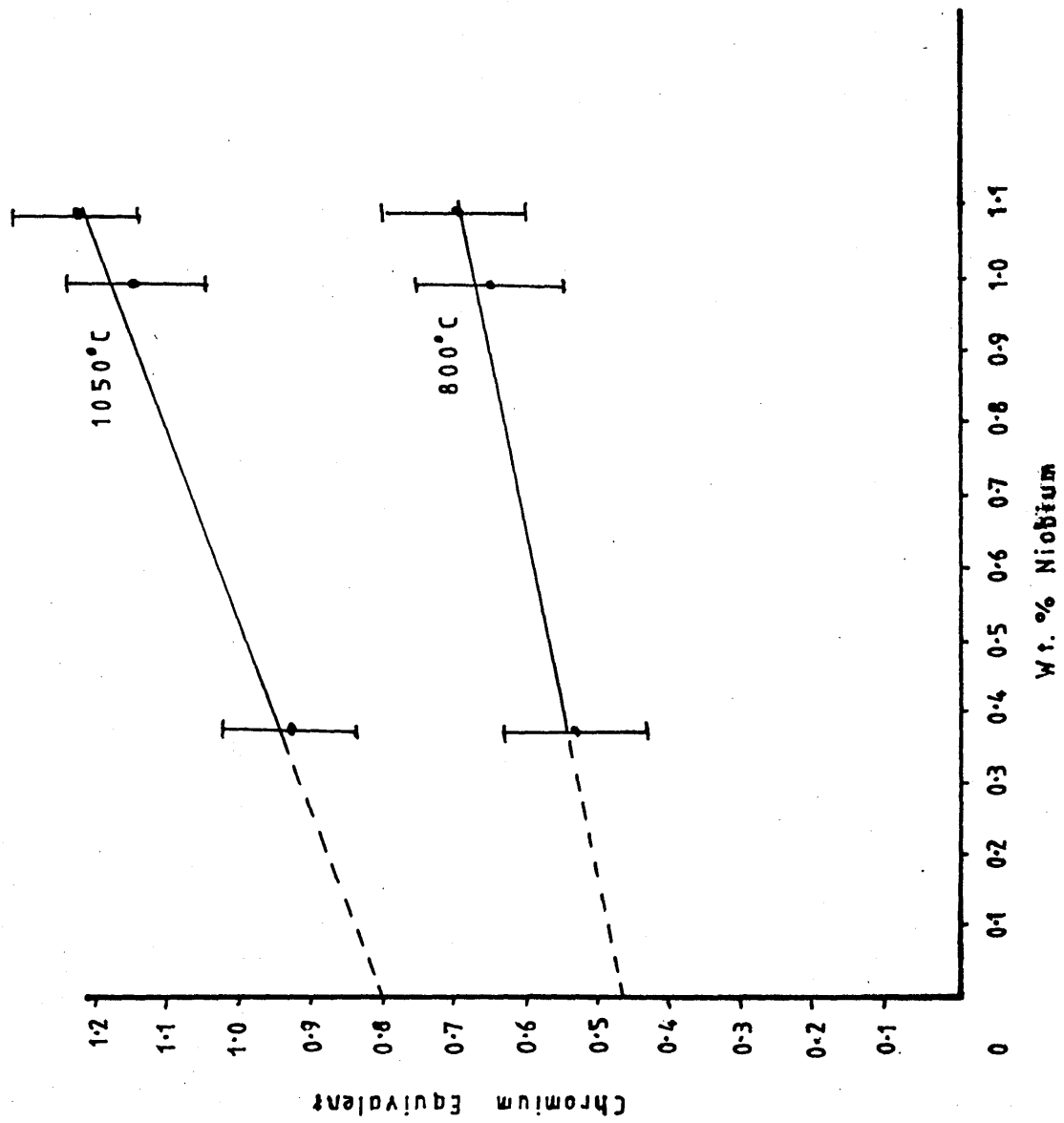


Fig. 67

The chromium equivalent of titanium at 1050°C and 800°C
as a function of titanium content.

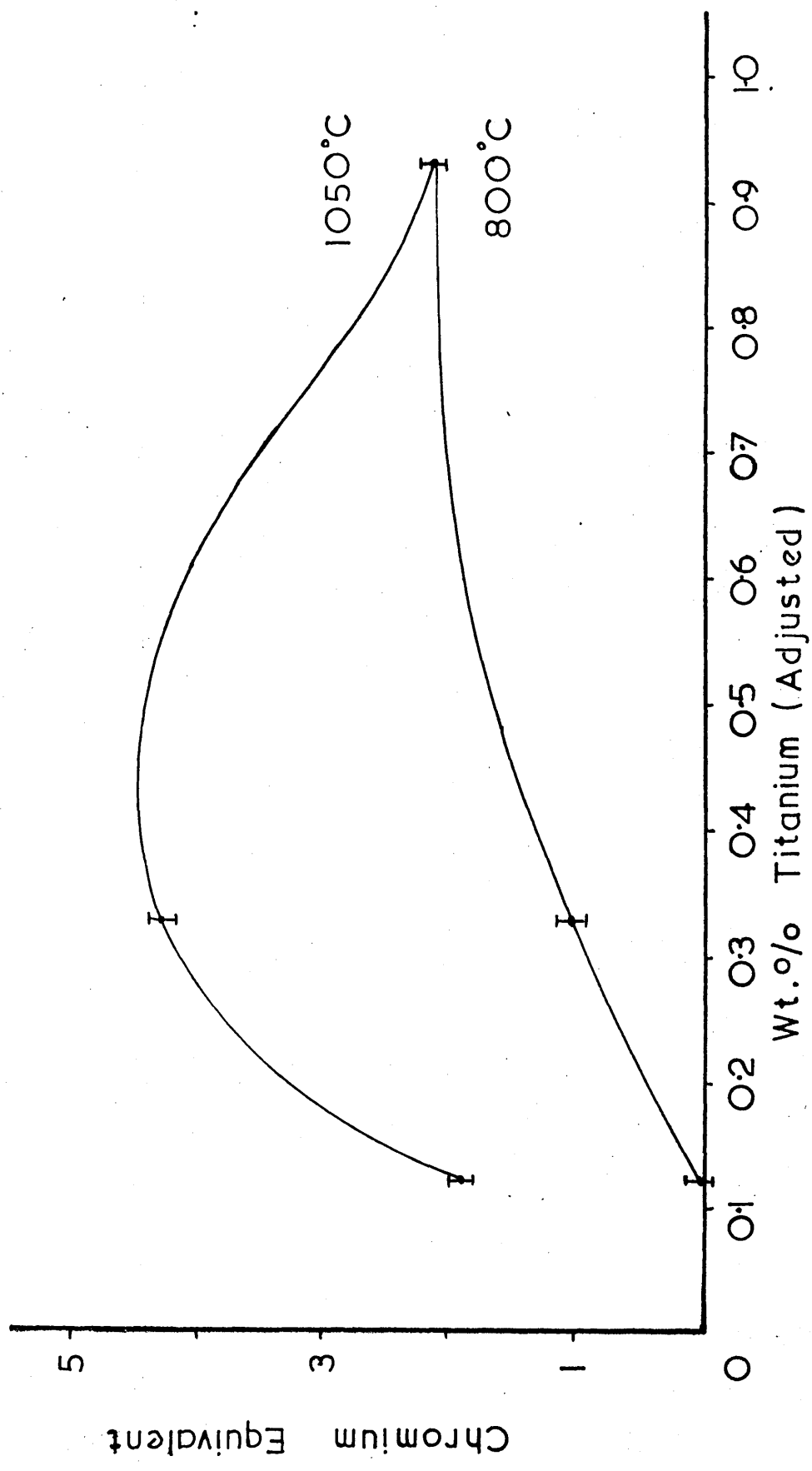


Fig. 68

Shows the increase in void size with dose for a 1wt%Si bearing alloy, irradiated at 500°C, where (a) was irradiated up to 7 dpa, (b) 12 dpa and (c) 20 dpa.

Fig. 69

Shows the void swelling characteristics of the silicon bearing alloy irradiated in the H.V.E.M. at 500°C and at ~ 0.5 d.p.a. min.⁻¹.

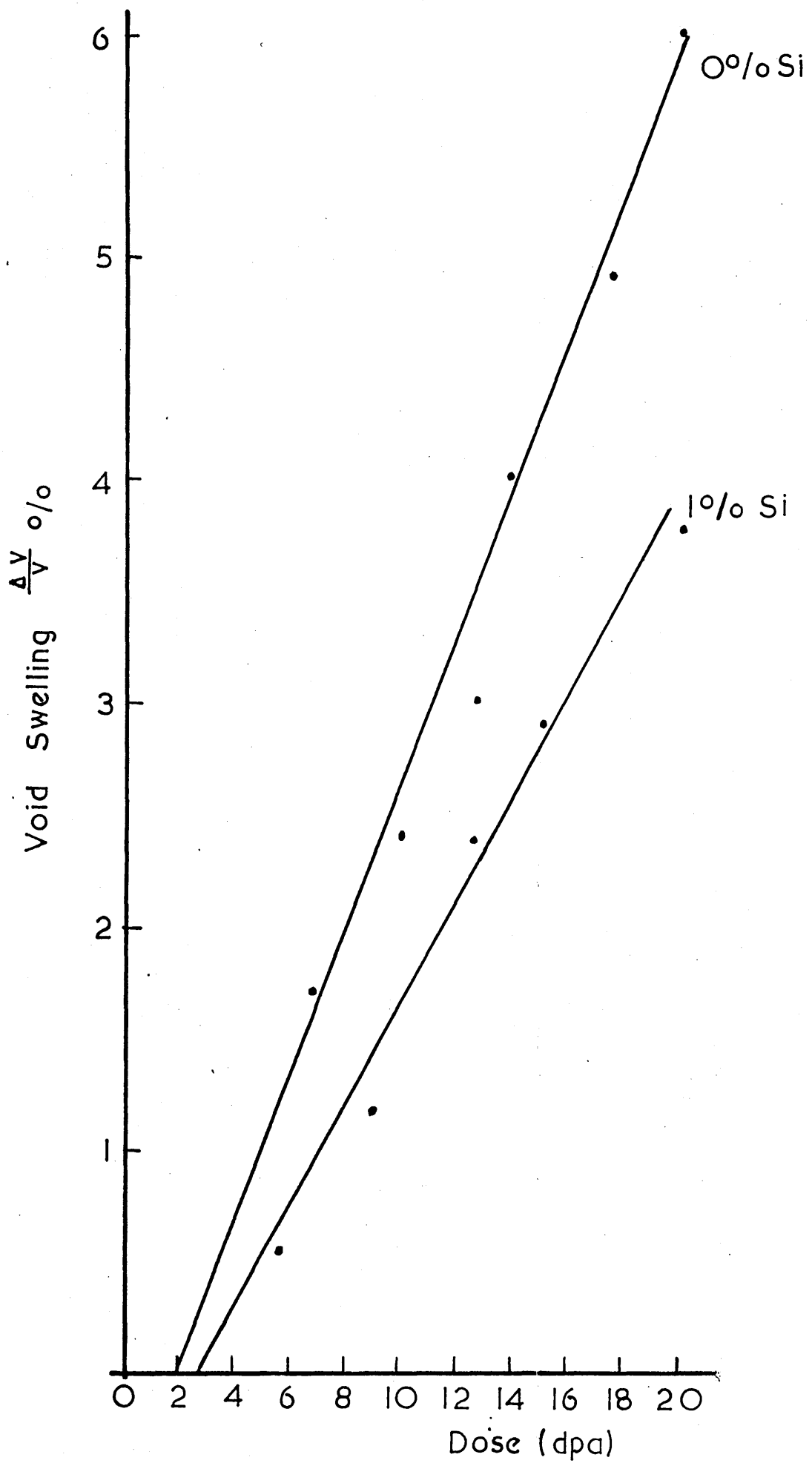


Fig. 70

Shows the void swelling characteristics of the manganese bearing alloys irradiated in the H.V.E.M. at 500°C and at ~ 0.5 d.p.a. min.⁻¹.

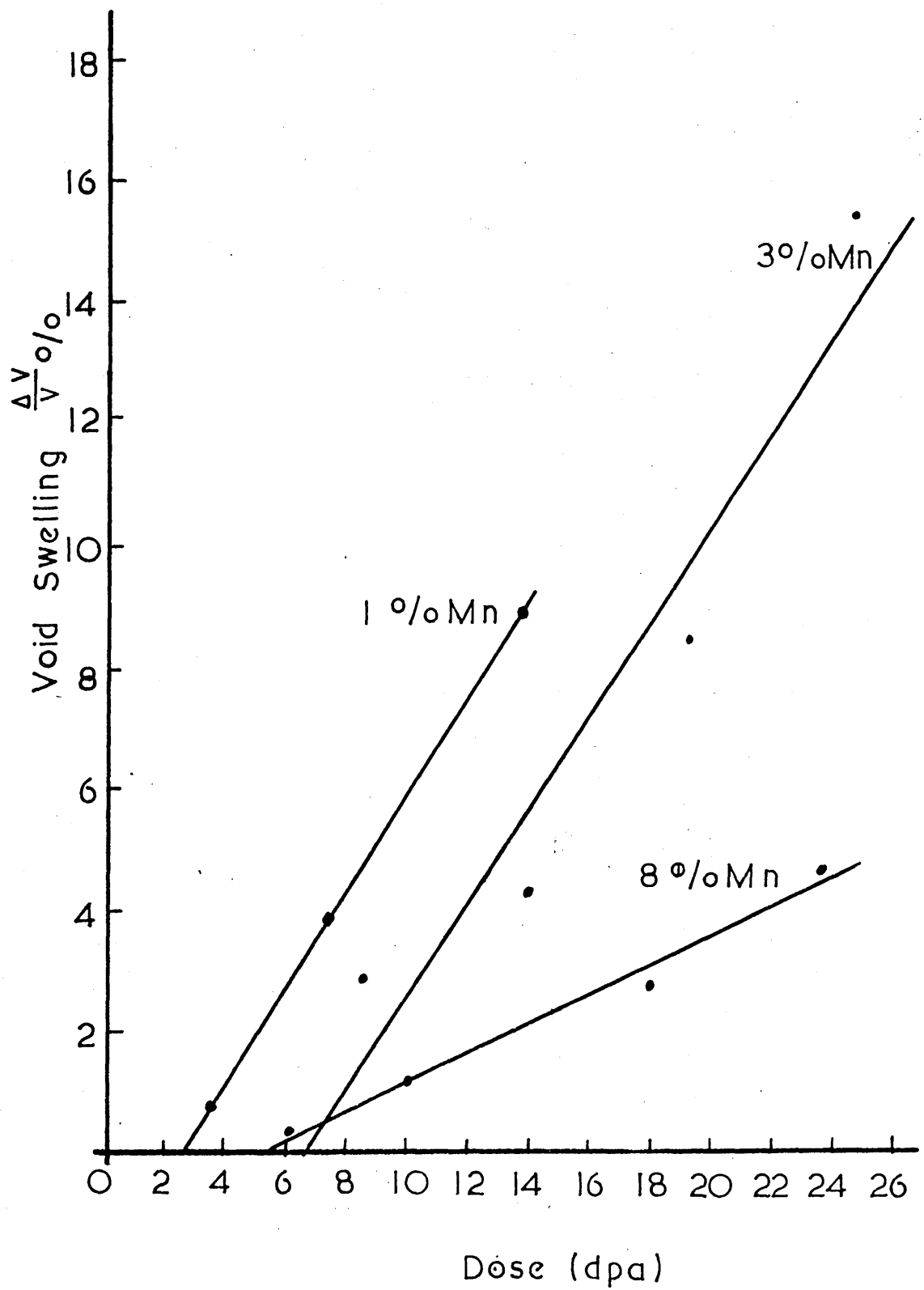


Fig. 71(a)

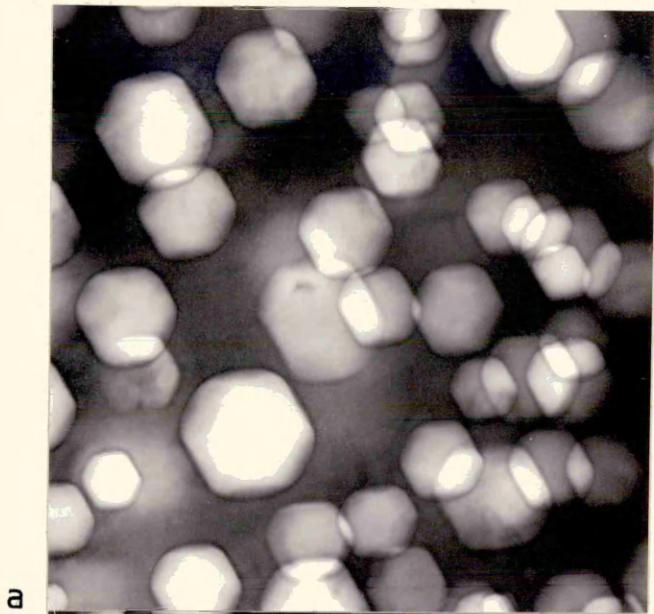
Shows the dislocation loop structure that was developed during irradiation at 500°C in the H.V.E.M. in the 7.5wt%Cu containing alloy up to a dose of ~ 30 dpa.

Fig. 71(b)

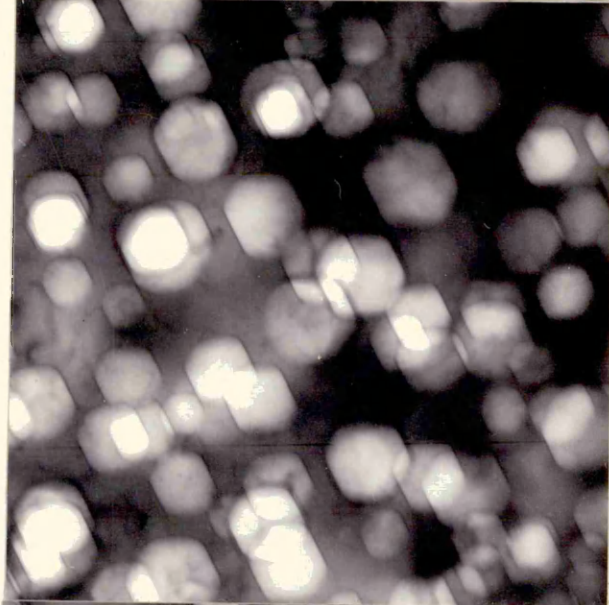
Shows the morphology of the voids in the 8wt%Mn alloy irradiated in the H.V.E.M. at 500°C up to a dose of ~ 30 dpa.

Fig. 72

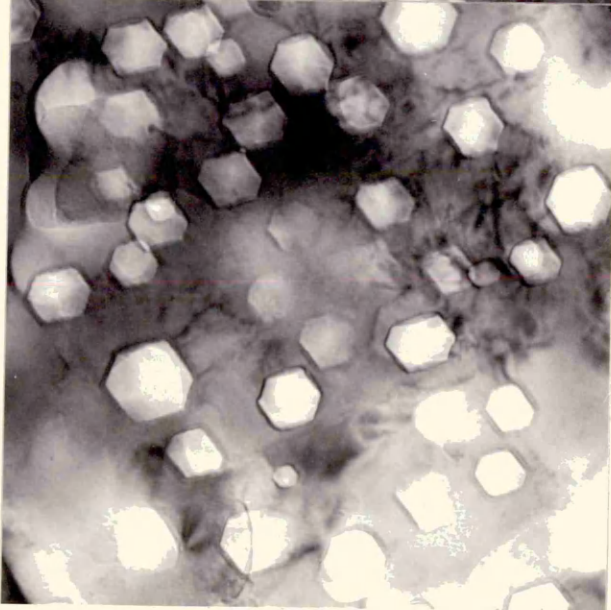
Shows the void swelling characteristics of the molybdenum containing alloys irradiated in the V.E.C. at 600°C. (a) contains 3.75wt%Mo, (b) 1.98wt%Mo and (c) 0wt%Mo.



a



b



c

x150K

Fig. 73

A summary of the effect of irradiation in the V.E.C. using
46 MeVNi⁶⁺ ions at 600°C at a dose of 40 d.p.a. for alloys
containing Mn,Cu,Si and Mo. -

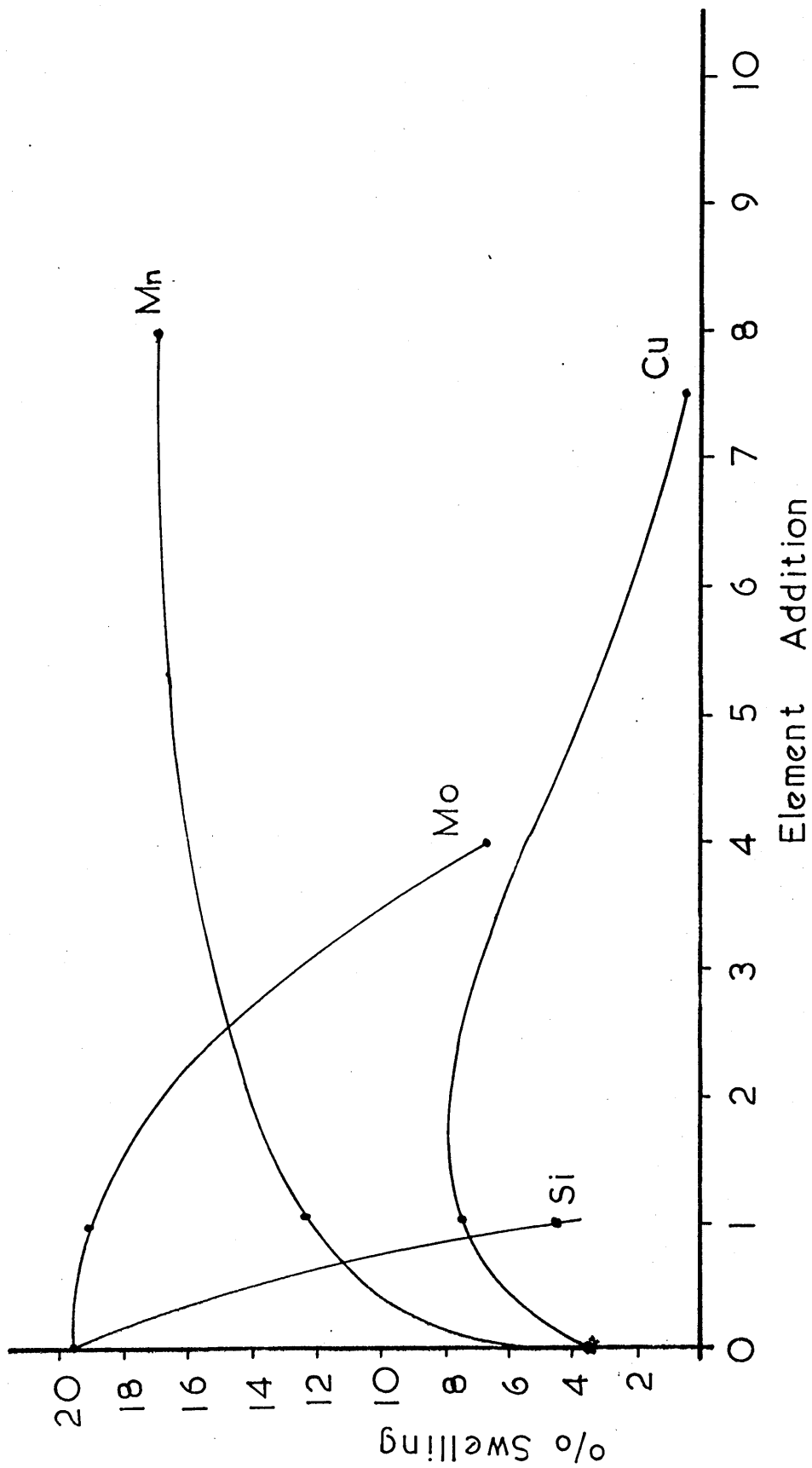


Fig. 74

Shows the effect of heavy ion irradiation on the constitution of the duplex microstructure. The austenite at the bottom of the micrograph contains voids whilst the delta ferrite has transformed to a cellular structure of (sigma phase + new austenite). It is evident that the new austenite has begun to swell by the formation of voids.



x150

2